DIPLOMARBEIT

Dynamics of correlations of fermions in lattices

Application of the time-dependent two-particle reduced density matrix method

Ausgeführt am Institut für

Theoretische Physik
der Technischen Universität Wien

ausgeführt unter der Anleitung von
O.Univ.-Prof. Dipl.-Phys. Dr.rer.nat. Joachim Burgdörfer
Dipl.-Ing. Dr. techn. Iva Březinová

von

Stefan Donsa
Troststraße 100/2/13
1100 Wien

Ort, Datum

Unterzeichner

Contents

Abbreviations

Alcoba: Purification scheme introduced by Alcoba.

EC: Energy conserving purification scheme.

NY: Valdemoro reconstruction including the approximation of the three-particle cumulant by Nakatsuji and Yasuda of the three-particle reduced density matrix.

NY+CC: Contraction consistent Valdemoro reconstruction including the approximation of the three-particle cumulant by Nakatsuji and Yasuda of the three-particle reduced density matrix.

TD-2RDM: Time-dependent two-particle reduced density matrix method.

Val: Valdemoro reconstruction of the three-particle reduced density matrix.

Val+CC: Contraction consistent Valdemoro reconstruction of the three-particle reduced density matrix.

1. Introduction

Correlations in many-body quantum states are currently a highly active field of research due to the fact that correlations lead to interesting properties while at the same time being enormously difficult to describe theoretically. While for weakly correlated systems the picture of non-interacting particles provides a good starting point for calculations this is not true for strongly correlated systems which show a qualitatively different behavior [1]. The inclusion of correlations into theoretical methods such as density functional theory [2] or time-dependent density functional theory [3] is an interesting current question with no unique answer. Especially for strongly correlated systems theoretical methods are limited [1]. One of the most famous model systems to investigate strong correlations is the Hubbard model [1, 4]. Despite its simplicity it shows very rich physics and is exactly solveable only for the one-dimensional case [5, 6].
A recent experimental realization of the Hubbard model was achieved with ultracold atoms in optical lattices [7, 8] were characteristic features of the Hubbard model such as the Mott metal-insulator transition were observed for bosons [9] and fermions [10]. A lot of research is being conducted currently [11, 12] to use ultracold atoms as experimental quantum simulators [13]. With these systems experimentalists hope to enter regimes of the Hubbard model that are not understood so far. This is necessary since the main theoretical methods to describe the Hubbard model, e.g. Quantum Monte-Carlo methods [8], dynamical mean field theory [14] or dynamical matrix renormalization group theory for one-dimensional systems [15], are not capable to describe all phenomena of the Hubbard model, e.g. high temperature superconductivity, frustrated antiferromagnetic phases or ultracold dipolar gases [8, 16].
Investigating the Hubbard model, we start with the question how to define correlations and and how to quantify them such that we can compare different systems with each other and determine which one is more correlated. Throughout literature there are numerous definitions of correlations [17–21] and so far there is no measure universally agreed on [22]. Having defined such correlation measures we apply the time-dependent two-particle reduced density matrix (TD-2RDM) method [23] to the one-dimensional fermionic Hubbard model and investigate its performance compared to the exact calculation and previous attempts to describe the non-equilibrium physics of the Hubbard model using reduced density matrices [24–26]. Within the TD-2RDM method we neglect three-particle correlations and test to which level this assumption is justified for the Hubbard model.

The structure of the thesis is as follows: We review the Hubbard model and its connection to ultracold atoms in optical lattices. Thereafter, we give a short introduction to correlations before reviewing the concept of reduced-density matrices (RDMs) and how the different orders of RDMs are coupled. We truncate the equations of motion for the RDMs at the two-particle level and discuss the problems that arise through the reconstruction of the three-particle reduced density matrix. Thereafter, we define different measures for correlations that will be applied in this thesis. We give the equations of motion for the Hubbard model within the TD-2RDM method. We investigate the influence of correlations on the eigenstates of the Hubbard model and show limitations of our method arising from them. Finally we show how correlations build up from a highly non-equilibrium and un-correlated state and compare the result of TD-2RDM method with the exact calculation and previous attempts [24–26]. We show the limitations of the method and propose possible ways to overcome them.

2. Experimental simulators of strongly correlated electrons: Ultracold atoms in optical lattices

Ultracold atoms confined in optical lattices are frequently invoked to mimic the complex physics of strongly correlated many-electron systems. Optical lattices are highly tunable and together with the tune-ability of the interaction strength between the atoms via Feshbach-resonances these systems are prominent candidates for the exploration of correlations in a simplified setting [7, 12, 13].
A prominent model which can be realized with these experiments is the Hubbard-model. The Hubbard model was developed to describe particles in a periodic potential in the tight-binding approximation. It was introduced by J. Hubbard in 1963 to model electronic correlations in narrow energy bands [4]. It is the simplest model for electrons moving in a solid that includes the Pauli exclusion principle and an electron-electron interaction term. Optical lattices loaded with ultra-cold Fermi gases are an ideal realization of the Hubbard model but not of a real solid [8] since in optical lattices there are no lattice defects and it is not possible to excite phonons. Moreover, all effects due to long-range interactions and incomplete screening are neglected. Hence, one can use optical lattices to emulate some fundamental properties of a solid but they fail to account for more complex effects where the interaction between electrons and phonons is important such as, e.g., the BCS theory for superconductors.
The phase transition from a superfluid phase to a Mott insulating phase was observed in 2002 in a three-dimensional (3D) optical lattice for repulsively interacting bosons [9] and in 2008 for fermions [10]. By increasing the depth of the lattice potential V_0 the phase transition of the atomic cloud from a superfluid to a Mott-insulating phase was observed.
In this chapter, we will give a brief review of the Hubbard model, the basic features of optical lattices, and how one can model the Hubbard model with ultracold atoms in optical lattices. We follow the more detailed discussions given in, e.g., [5, 7, 8, 12, 13, 16, 27].

2.1. Optical lattices

Optical lattices arise due to the interaction of atoms with standing waves of laser light. The resulting trapping property is based on a second order effect. The laser light induces an electrical dipole moment in the atoms which then interacts with the standing wave created by the laser light. We briefly review the underlying physics following [27]. In the dipole approximation in length gauge the atom-field interaction is given by

$$H_{\text{dipole}} = -\mathbf{d} \cdot \mathbf{E}(\mathbf{r}, t), \tag{2.1}$$

where $\mathbf{d}$ is the dipole moment operator, and $\mathbf{E}(\mathbf{r}, t)$ is the electric field. In order to simplify calculations we write the electric field with frequency ω as $\mathbf{E}(\mathbf{r}, t) = \mathbf{E}_\omega e^{-i\omega t} + \mathbf{E}_{-\omega} e^{i\omega t}$. To calculate the shift of the electronic groundstate energy, ΔE_g, due to H_{dipole} we use standard quantum perturbation theory. The first order contribution $\langle g | H_{\text{dipole}} | g \rangle$ vanishes and the second order term is

$$\begin{aligned}
\Delta E_g &= \sum_e \langle g | \mathbf{d} \cdot \mathbf{E}_\omega | e \rangle \frac{1}{E_e - E_g + \hbar\omega} \langle e | \mathbf{d} \cdot \mathbf{E}_{-\omega} | g \rangle \\
&+ \sum_e \langle e | \mathbf{d} \cdot \mathbf{E}_{-\omega} | g \rangle \frac{1}{E_e - E_g - \hbar\omega} \langle g | \mathbf{d} \cdot \mathbf{E}_\omega | e \rangle \\
&= -\frac{1}{2} \alpha(\omega) \left\langle \mathbf{E}(\mathbf{r}, t)^2 \right\rangle_t ,
\end{aligned} \tag{2.2}$$

where $|g\rangle$ ($|e\rangle$) is the ground (excited) state of the atom associated with the energies $E_g(E_e)$, the sum runs over all possible excited states, $\hbar\omega$ is the energy of the photons in the laser field, $\alpha(\omega)$ is the polarizability of the atom, and $< ... >_t$ denotes a time average. When the laser is (slightly) detuned from resonance, it is sufficient to take only the coupling between two states of the atom with resonance frequency $\omega_0 = (E_e - E_g)/\hbar$ into account and to assume that the term with smallest energy denominator is dominant. Doing so the polarizability $\alpha(\omega)$ reduces to

$$\alpha(\omega) \approx \frac{|\langle e|\mathbf{d}|g\rangle|^2}{\hbar(\omega_0 - \omega)}. \tag{2.3}$$

This calculation assumes that the excited state has an infintely long life time which is not the case. In reality, it decays spontaneously with the emission of a photon. Taking into account the finite lifetime $1/\Gamma_e$ we arrive at

$$\alpha(\omega) \approx \frac{|\langle e|\mathbf{d}|g\rangle|^2}{\hbar(\omega_0 - \omega) - i\hbar\Gamma_e/2} = . \tag{2.4}$$

The total energy shift of the groundstate energy is then

$$\Delta E_g \approx V_g - i\hbar \frac{\Gamma_{\text{loss}}}{2}, \tag{2.5}$$

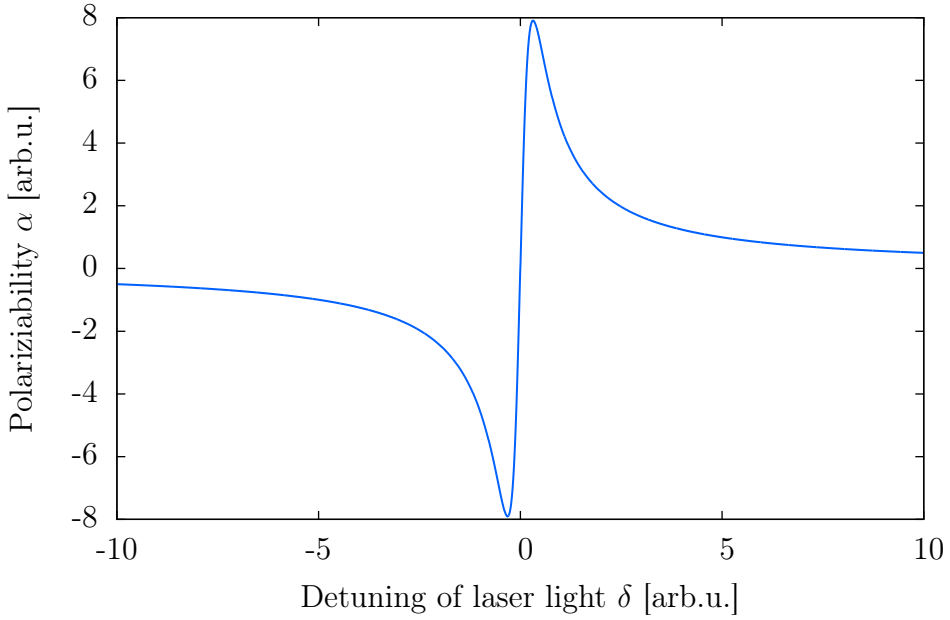

Figure 2.1.: Real part of the polariziability α for different laser detunings $\delta = \omega - \omega_0$.

with

$$V_g = -\frac{1}{2} Re\left(\alpha(\omega)\right) \left\langle \mathbf{E}(\mathbf{r},t)^2 \right\rangle_t = -\frac{1}{2}\alpha'(\omega) \left\langle \mathbf{E}(\mathbf{r},t)^2 \right\rangle_t = \frac{\hbar \Omega_R^2 \delta}{\delta^2 + \Gamma_e^2/4}, \tag{2.6}$$

where $\delta = \omega - \omega_0$ is the detuning of the laser light from the inneratomic resonance, and $\Omega_R = \left|\langle e \left|\mathbf{d}\cdot\mathbf{E}\right| g\rangle\right| / \hbar$ is the Rabi frequency. The term

$$\Gamma_{\text{loss}} = \frac{\Gamma_e \Omega_R^2}{\delta^2 + \Gamma_e^2/4}, \tag{2.7}$$

is a loss term taking into account particles that spontaneously emit to the ground state and cease to be bound by the trap. Calculating the dipole potential perturbatively is valid as long as $\Omega_R \ll \left(\delta^2 + \Gamma_e^2/4\right)^{1/2}$ which holds under almost all conditions for experiments with ultracold atoms [27, 28]. The magnitude of the optical potential can be tuned by changing Ω_R, which is proportional to the laser intensity, and by changing the detuning δ. The detuning moreover governs the ratio between V_g and $\hbar\Gamma_{\text{loss}}$ which is $V_g/\hbar\Gamma_{\text{loss}} = \delta/\Gamma_e$. For the experimental realization it is important to note that the optical potential V_g scales with I/δ while the loss of atoms Γ_{loss} scales with I/δ^2 where $I \propto \langle \mathbf{E}(\mathbf{r},t)^2 \rangle_t$ is the intensity of the laserlight. Therefore, optical traps use large detunings combined with high intensities to create suffienctly deep potentials with a small loss rates [28]. The effective energy shift generates an effective potential and, therefore, induces a dipole force on the cloud

of atoms,

$$\mathbf{F}_{dip} = -\vec{\nabla} V_g(\mathbf{r}) = \frac{1}{2}\alpha'(\omega)\vec{\nabla}\left\langle \mathbf{E}(\mathbf{r},t)^2 \right\rangle_t . \tag{2.8}$$

The sign of the polarizability α' determines whether the dipole moment points in the same or in the opposite direction as the electric field, see Fig. 2.1. If ω is smaller than ω_0 ($\delta < 0$), red - detuned laser light, the dipole points in the same direction as the eletric field and the potential is attractive. If $\delta > 0$, blue - detuned laser light, the dipole points in the opposite direction as the electric field and the potential is repulsive. In the attractive case, the potential minima are correspond to maxima in the intensity of the laser light, while in the repulsive case the potential minima correspond to the minima of the laser light.
In one dimension (1D) an optical lattice can be created by two counterpropagating laser beams with a Gaussian profile which leads to a potential of the form

$$V_{\text{trap}}(\xi, x) \approx V_0 e^{-2\xi^2/w^2(x)} \sin^2(kx), \tag{2.9}$$

where x is the propagation direction, ξ is the distance from the focal point of the laser, $w(x)$ is the beam waist, V_0 is the maximum depth of the optical potential, $k = 2\pi/\lambda$ is the wavenumber, and λ is the wavelength of the laser light [13]. The primitive period of the potential $a = \lambda/2$ can be changed by using laser light with different wavelengths or by slightly changing the angle between the laser beams [29]. In the center of the trap the trapping potential of the optical lattice can be approximated by a simple sinusoidal potential, for more details see for example [13]. We thus have a periodic potential with two parameters namely the potential depth and the size of the unit cell where both parameters can be changed at will. To make the analogy to a solid more explicit, we now have a periodic potential with variable lattice depth and lattice constant. One can create one-dimensional (1D), two-dimensional (2D), or three-dimensional (3D) lattices by choosing the appropriate number of counter-propagating laser beams.

2.2. Hubbard model

We give a brief derivation of the Hubbard Hamiltonian following [5]. We start out with the basic many-body Hamiltonian for electrons in an atomic lattice including an electron-electron interaction term V_{int} in the Born-Oppenheimer approximation

$$H = \sum_{i=1}^{N} \left(-\frac{\hbar^2}{2m}\partial^2_{\mathbf{x}_i} + V_p\left(\mathbf{x}_i\right) \right) + \frac{1}{2} \sum_{1 \le i,j \le N} V_{\text{int}}\left(\mathbf{x}_i, \mathbf{x}_j\right), \tag{2.10}$$

where N is the number of electrons with mass m, $V_p\left(\mathbf{x}\right) = V_p\left(\mathbf{x} - \mathbf{R}_j\right)$ is the periodic potential around the atomic lattice sites $\mathbf{R}_j$, and $V_{\text{int}}\left(\mathbf{x}_i, \mathbf{x}_j\right)$ is the interaction

potential between the electrons. We can seperate this Hamiltonian in N effective one-body Hamiltonians

$$h_1(\mathbf{x}) = -\frac{\hbar^2}{2m}\partial^2_{\mathbf{x}_i} + V_p(\mathbf{x}), \tag{2.11}$$

and a sum over the interaction terms V_{int}. By making an ansatz for the wave function using Bloch's theorem

$$\phi_{\alpha,\mathbf{k}}(\mathbf{x}) = e^{i\mathbf{k}\cdot\mathbf{x}} u_{\alpha,\mathbf{k}}(\mathbf{x}), \tag{2.12}$$

we find the one-particle eigenfunctions of h_1

$$h_1\phi_{\alpha,\mathbf{k}}(\mathbf{x}) = \epsilon_{\alpha,\mathbf{k}}\phi_{\alpha,\mathbf{k}}(\mathbf{x}), \tag{2.13}$$

with $\mathbf{k}$ being the quasi-momentum of the lattice, α being the band index, and $\epsilon_{\alpha,\mathbf{k}}$ the eigenenergy of an electron in the band α with quasi-momentum $\mathbf{k}$. α runs from 0 to ∞ where the band with index 0 contains the functions with lowest energy eigenvalues $\epsilon_{0,\mathbf{k}}$. $u_{\alpha,\mathbf{k}}$ has the periodicity of the lattice and the quasi-momentum lies inside the first Brillouin zone. Being eigenfunctions of the one-particle Hamiltonian h_1, the $\phi_{\alpha,\mathbf{k}}(\mathbf{x})$ build up a complete basis set of one-particle states for h_1. A complementary set of basis functions are the Wannier functions $W_{\alpha,m}$ which are localized around the lattice sites $\mathbf{R}_m$. They can be constructed from the Bloch eigenfunctions $\phi_{\alpha,\mathbf{k}}$ by

$$W_\alpha(\mathbf{x}-\mathbf{R}_m) = \frac{1}{V_{BZ}}\int \mathrm{d}^3k\, \phi_{\alpha,\mathbf{k}}(\mathbf{x})\, e^{-i\mathbf{R}_m\cdot\mathbf{k}}. \tag{2.14}$$

The integration runs over the first Brillouin zone and we divide by the volume of the first Brillouin zone V_{BZ} to ensure normalization of $W_{\alpha,m}$. The Wannier functions are orthonormal to each other for different energy bands and different sites $\langle W_{\alpha,m}|W_{\beta,n}\rangle = \delta_{\alpha,\beta}\delta_{m,n}$. We will calculate the Wannier functions for a one dimensional optical lattice in Sec. 2.3 and use them to illustrate our results in Sec. 5. Using the standard creation (annihilation operators) $\hat{a}^\dagger_{\alpha i,\sigma}$ ($\hat{a}_{\alpha i,\sigma}$) which create (annihilate) an electron with spin σ at site i in the energy band α we can rewrite the initial Hamiltonian, Eq. 2.10, in second quantization as

$$H = \sum_{\substack{\alpha\\ i,j\\ \sigma}} J^\alpha_{ij}\, \hat{a}^\dagger_{\alpha i,\sigma}\hat{a}_{\alpha j,\sigma} + \frac{1}{2}\sum_{\substack{\alpha,\beta,\gamma,\delta\\ i,j,k,l\\ \sigma_1,\sigma_2}} U^{\alpha,\beta,\gamma,\delta}_{i,j,k,l}\, \hat{a}^\dagger_{\alpha i,\sigma_1}\hat{a}^\dagger_{\beta j,\sigma_2}\hat{a}_{\gamma k,\sigma_2}\hat{a}_{\delta l,\sigma_1}, \tag{2.15}$$

where the hopping matrix elements J^α_{ij} are given by

$$J^\alpha_{ij} = \int \mathrm{d}^3x\, W^*_\alpha(\mathbf{x}-\mathbf{R}_i)\, h_1 W_\alpha(\mathbf{x}-\mathbf{R}_j), \tag{2.16}$$

and the interaction parameters can be calculated using the overlap integrals

$$U_{i,j,k,l}^{\alpha,\beta,\gamma,\delta} = \int \mathrm{d}^3x_1\mathrm{d}^3x_2 W_\alpha^*\left(\mathbf{x}_1-\mathbf{R}_i\right) W_\beta^*\left(\mathbf{x}_2-\mathbf{R}_j\right) V_{\mathrm{int}}\left(\mathbf{x}_1,\mathbf{x}_2\right) W_\gamma\left(\mathbf{x}_2-\mathbf{R}_k\right) W_\delta\left(\mathbf{x}_1-\mathbf{R}_l\right). \tag{2.17}$$

So far, we did not make any approximations and the Hamiltonian in Eq. 2.15 is identical to Eq. 2.10. From Eq. 2.15, we see that hopping is only allowed within an energy band and a spin flip is prohibited. Hopping is only allowed if the target site is not occupied as a consequence of the Pauli exclusion principle. The interaction takes place between electrons in different bands and with different spins.
The Hubbard model can be otained from Eq. 2.15 assuming that the interaction is very short-ranged, or to be more precise, if the on site interaction $U_{i,i,i,i}^{\alpha,\beta,\gamma,\delta}$ is much larger than all other contributions. The second assumption leading to the Hubbard model is that the Fermi surface lies within one single energy band. All other bands are neglected. This allows to write down a Hamiltonian with the effective parameters J_{ij} and $U = U_{i,i,i,i}^{\alpha,\alpha,\alpha,\alpha}$

$$H = \sum_{\substack{ij\\ \sigma}} J_{ij}\hat{a}_{i,\sigma}^\dagger \hat{a}_{j,\sigma} + \frac{U}{2}\sum_{\substack{i\\ \sigma_1,\sigma_2}} \hat{a}_{i,\sigma_1}^\dagger \hat{a}_{i,\sigma_2}^\dagger \hat{a}_{i,\sigma_2}\hat{a}_{i,\sigma_1}. \tag{2.18}$$

Using the tight-binding approximation which implies that the Wannier functions $W_\alpha\left(\mathbf{x}-\mathbf{R}_i\right)$ are strongly localized around the lattice site $\mathbf{R}_i$ we can further simplify this Hamiltonian by keeping only hopping elements between adjacent sites. Since we want to treat fermions (i.e., atomic species with spin $F = 1/2$) we just consider spin $\uparrow$ and $\downarrow$. We then arrive at the final Fermi - Hubbard Hamiltonian

$$H_{\mathrm{Hub}} = -J\sum_{\substack{\langle i,j\rangle\\ \sigma\epsilon(\downarrow,\uparrow)}} \hat{a}_{i,\sigma}^\dagger \hat{a}_{j,\sigma} + U\sum_i \hat{n}_{i,\uparrow}\hat{n}_{i,\downarrow}, \tag{2.19}$$

where $\hat{n}_{i,\uparrow} = \hat{a}_{i,\uparrow}^\dagger \hat{a}_{i,\uparrow}$ and $\hat{n}_{i,\downarrow} = \hat{a}_{i,\downarrow}^\dagger \hat{a}_{i,\downarrow}$ are the particle number operators which count the number of electrons with spin $\uparrow$ ($\downarrow$) at site i. $\langle i,j\rangle$ denotes the sum over nearest neighbors, i.e. $i = j \pm 1$. The sign in front of the hopping term is chosen such that the parameter J is a positive number, since the value of $J_{i,j}$ for adjacent sites is negative in our case. The second term describes on-site interaction and neglects all interactions between electrons which are not located at the same site.
As usual for fermionic systems one can formulate the Hubbard model either via holes or via particles. The completely symmetric case corresponds to half-filling where N sites are filled with $N/2$ electrons with spin $\uparrow$ and $N/2$ electrons with spin $\downarrow$. It is instructive to look at the two extreme cases for the Hubbard model at half filling.

J=0 In this case the Hamiltonian is already diagonal and the groundstate for N sites is $\binom{N}{N/2}$ degenerate with every site being occupied with only one electron. The ground state energy of this system is 0. This limit corresponds to $\frac{U}{J} \gg 1$ and is called the atomic limit.

U=0 For $U = 0$ the model can be solved analytically and the many-body eigenfunctions are antisymmetrized product states of the successively occupied one-particle eigenfunctions of the one-particle Hamiltonian. The ground state is non-degenerate.

2.3. The Hubbard model for optical lattices

To derive the actual parameters for the 1D one-band Hubbard model we closely follow [8]. The wavelength of the laser light is $\lambda = 2\pi/k_{\text{latt}}$ which forms a lattice with lattice constant $a_{\text{latt}} = \lambda/2$. The periodic potential has the form $V(x) = V_0 \sin^2(k_{\text{latt}}x)$. The time-independent one-particle Schrödinger equation is given by

$$H\,\psi(x) = \left(-\frac{\hbar^2}{2m}\partial_x^2 + V_0 \sin^2(k_{\text{latt}}x)\right)\psi(x) = E\psi(x). \tag{2.20}$$

From now on, we work in units of the recoil energy $E_R = \frac{\hbar^2 k_{\text{latt}}^2}{2m} = \frac{\hbar^2\pi^2}{2ma_{\text{latt}}^2}$ which is the change in kinetic energy if the atom absorbs or emits a photon of the laser beam. In these units the Schrödinger equation reads as

$$H_R\,\psi(x) = \left(-\frac{1}{k_{\text{latt}}^2}\partial_x^2 + \frac{V_0}{E_R}\sin^2(k_{\text{latt}}x)\right)\psi(x) = \frac{E}{E_R}\psi(x). \tag{2.21}$$

Typical values in experiments with, e.g., ^{40}K atoms are $\lambda = 738$ nm and optical lattice depths of up to $V_0 = 20\ E_R$ [30]. The ratio of kinetic and interaction energy U/J ranges typically between zero and up to 200 in experiments [12, 30]. To derive the hopping and interaction parameters of the Hubbard model as a function of the tuneable potential parameters V_0 and a_{latt} we calculate the Wannier functions of this system. For this we solve Eq. 2.21 via exact diagonalization for $k \,\epsilon\, \left[-\frac{\pi}{a_{\text{latt}}}, \frac{\pi}{a_{\text{latt}}}\right]$. The boundary conditions correspond to Bloch boundary conditions

$$\psi_k(x + a_{\text{latt}}) = e^{ika_{\text{latt}}}\psi_k(x). \tag{2.22}$$

The eigenvalues of the problem form energy bands as expected for particles in a periodic potential. We construct Wannier functions for the lowest band. The Wannier functions are not uniquely defined because of the freedom to multiply every Bloch eigenfunction ψ_k with an arbitrary k-dependent phase. This phase may have a dramatic effect on the degree of localization of the final Wannier function.

For 1D it was shown by W. Kohn [31] that for a symmetric potential V around $x = 0$, i.e. $V(x) = V(-x)$ the maximally localized Wannier functions can be constructed uniquely by choosing ψ_k of Eq. 2.22 to be real at $x = 0$ and to ensure that the real part of the eigenfunctions is symmetric around $x = 0$. We normalize the eigenfunctions to

$$\frac{1}{a_{latt}} \int_{-a_{latt}/2}^{a_{latt}/2} \mathrm{d}x \ |\psi_k(x)|^2 = 1. \tag{2.23}$$

From this we can straightforwardly construct the Wannier functions using Eq. 2.14

$$W(x - x_1) = \frac{a_{latt}}{2\pi} \int_{-\pi/a_{latt}}^{\pi/a_{latt}} \mathrm{d}k \ \psi_k(x) e^{-ikx_1}, \tag{2.24}$$

where $x_1 = 0, \pm a_{latt}, \pm 2a_{latt}, ...$, and the prefactor corresponds to the inverse of the volume of the Brillouin-zone. The maximally localized Wannier functions are real, decay exponentially and are orthonormal such that [31]

$$\int_{-\infty}^{+\infty} \mathrm{d}x \ W^* \left(x - x_1\right) W \left(x - x_2\right) = \delta_{x_1, x_2}. \tag{2.25}$$

To calculate the nearest-neighbour hopping parameter J we use Eq. 2.16

$$\frac{J}{E_R} = \int_{-\infty}^{+\infty} \mathrm{d}x \ W^* \left(x - a_{latt}\right) H_R W \left(x\right). \tag{2.26}$$

We also calculate the hopping parameters for next nearest and next-next nearest neighbour hopping J_2, J_3 via

$$\frac{J_2}{E_R} = \int_{-\infty}^{+\infty} \mathrm{d}x \ W^* \left(x - 2a_{latt}\right) H_R W \left(x\right), \tag{2.27}$$

$$\frac{J_3}{E_R} = \int_{-\infty}^{+\infty} \mathrm{d}x \ W^* \left(x - 3a_{latt}\right) H_R W \left(x\right). \tag{2.28}$$

Before calculating the interaction parameter U we compare the different energy scales in the Hubbard model. One key assumption of the Hubbard model is that it is sufficient to consider just the lowest band of the bandstructure [5]. For this assumption to hold, the interaction parameter U has to be smaller than the band gap which is proportional to $\frac{V_0}{2}$ to leading order [32]. Otherwise the particles could be excited into the second energy band, see Fig. 2.2. This means that for small V_0, U has to be small in order for the single-band Hubbard model to hold. The hopping parameter J is proportional to the bandwidth and decreases with increasing V_0 exponentially, see below in Eq. 2.43 and Fig. 2.6a.
To calculate the effective interaction parameter U we assume that the gas of ultracold atoms is confined in two harmonic traps with different frequencies in the

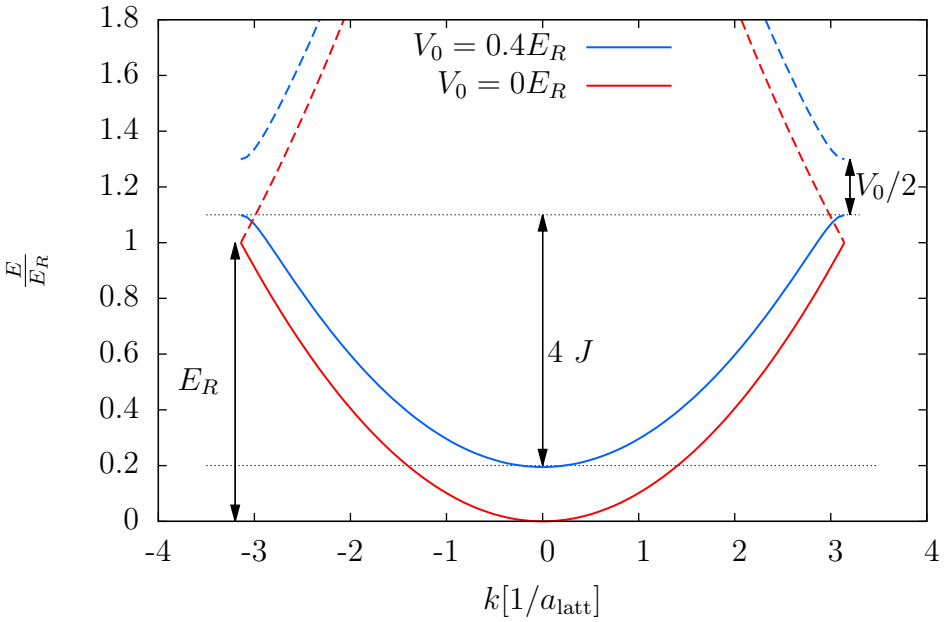

Figure 2.2.: The energy scales of the optical lattice. J is proportional to the bandwidth, V_0 is proportional to the bandgap, and E_R is the bandwidth of the system with $V_0 \to 0$.

transverse $\omega_\perp = \omega_y = \omega_z$ direction and the direction of the laser beams x, ω_x. In the transverse direction typically the confinement is much stronger (factor ≈ 1000), $\omega_\perp \approx 2\pi \times 100$ kHz, than in x $\omega_x \approx 2\pi \times 10 - 100$ Hz, such that the condensate always stays in the ground state of the transverse harmonic confinement and the dynamics is fully reduced to 1D [7]. We write the full 3D wave function as

$$\Psi(x, y, z) = W(x)\Psi_{\text{Gauss}}(y)\Psi_{\text{Gauss}}(z) \tag{2.29}$$

where $\Psi_{\text{Gauss}}(...)$ is the Gaussian ground state of the transverse harmonic oscillator. We consider pairwise point-like interaction since for cold atoms the interaction is dominated by the s-wave scattering length a_s. Thus, we replace the interatomic interaction V_{int} by the effective pseudopotential $V_{\text{eff}}(\mathbf{x}_1, \mathbf{x}_2) = g\delta(\mathbf{x}_1 - \mathbf{x}_2)$ with $g = \frac{4\pi\hbar^2 a_s}{2\mu}$ where $\mu = \frac{m_1 m_2}{m_1 + m_2}$ is the reduced mass of the two interacting atoms. Considering a cloud formed out of identical atoms, $\mu = \frac{m}{2}$ and thus $g = \frac{4\pi\hbar^2 a_s}{m}$, for

more detail see for example [7]. Inserting Eq. 2.29 into Eq. 2.17 we obtain

$$\begin{aligned} U &= \int \mathrm{d}^3x_1\, \mathrm{d}^3x_2\, \Psi^*(\mathbf{x}_1)\Psi^*(\mathbf{x}_2)V_{\text{eff}}\left(\mathbf{x}_1,\mathbf{x}_2\right)\Psi(\mathbf{x}_2)\Psi(\mathbf{x}_1) \\ &= \int \mathrm{d}^3x_1\, \mathrm{d}^3x_2\, \Psi^*(\mathbf{x}_1)\Psi^*(\mathbf{x}_2)\delta\left(\mathbf{x}_1-\mathbf{x}_2\right)\Psi(\mathbf{x}_2)\Psi(\mathbf{x}_1) \qquad (2.30) \\ &= g\int \mathrm{d}x_1\ |W(x_1)|^4 \int \mathrm{d}y_1\, |\Psi_{\text{Gauss}}(y_1)|^4 \int \mathrm{d}z_1\, |\Psi_{\text{Gauss}}(z_1)|^4 \\ &= 2\hbar\omega_\perp a_s \int \mathrm{d}x\ |W(x)|^4 \\ \frac{U}{E_R} &= \frac{4m\omega_\perp a_s a_{latt}^2}{\hbar\pi^2}\int \mathrm{d}x\ |W(x)|^4 . \qquad (2.31) \end{aligned}$$

2.3.1. The dependence of U and J on experimentally tunable parameters a_{latt} and V_0

The functional dependence of U and J on a_{latt} and V_0 can be traced back to the scaling property of the Schrödinger equation (Eq. 2.21). Performing a coordinate transformation to $k_{\text{latt}}x \to \xi$, the Schrödinger equation reads as

$$\tilde{H}_R\,\psi\left(\xi\right) = \left(-\partial_\xi^2 + \frac{V_0}{E_R}\sin^2\left(\xi\right)\right)\psi\left(\xi\right) = \frac{E}{E_R}\psi\left(\xi\right). \qquad (2.32)$$

Doing so, we can omit all the normalization factors of 2.24 depending on a_{latt}. These equations then read as

$$\int_{-\frac{1}{2}}^{\frac{1}{2}} \mathrm{d}\xi\ |\psi_k(\xi)|^2 = 1, \qquad (2.33)$$

and

$$W(\xi-\xi_1) = \frac{1}{2\pi}\int_{-\pi}^{\pi} \mathrm{d}k\ \psi_k(\xi)e^{-ik\xi_1}. \qquad (2.34)$$

By inserting these Wannier functions into Eq. 2.26 we can decompose $\frac{J}{E_R}$ into a term depending on a_{latt} explicitly and one that is independent of it

$$\begin{aligned} \frac{J}{E_R} &= -\int \mathrm{d}\xi\ \mathrm{W}^*\left(\mathrm{y}-1\right)\partial_\xi^2\ \mathrm{W}\left(\xi\right) + \frac{\mathrm{c}_1}{\mathrm{a}_{\text{latt}}^2}\int \mathrm{d}\xi\ \mathrm{W}^*\left(\xi-1\right)\sin^2(\xi)\ \mathrm{W}\left(\xi\right) \qquad (2.35) \\ &= c + \frac{c_1'}{a_{\text{latt}}^2}, \qquad (2.36) \end{aligned}$$

where all constants c, c_1, c_1' are dependent on $\frac{V_0}{E_R}$ but not on a_{latt} explicitly. The Wannier functions are implicitly dependent an a_{latt} because they depend on $\frac{V_0}{E_R} \propto$

a_{latt}^{-2}. Hence also $\frac{J}{E_R}$ is implicitly dependent on a_{latt}. Neglecting the second term c_1' we find that $\frac{J}{E_R}$ to leading order depends on $\frac{V_0}{E_R}$ without an explicit dependence on a_{latt}

$$\frac{J}{E_R} = f_1\left(\frac{V_0}{E_R}\right). \tag{2.37}$$

For the effective pseudopotential V_{eff} we obtain

$$\begin{aligned} V_{\text{eff}}\left(\mathbf{x}_1, \mathbf{x}_2\right) \propto \delta\left(\mathbf{x}_1 - \mathbf{x}_2\right) &= \delta\left(\frac{a_{\text{latt}}}{\pi}\left(\xi_1 - \xi_2\right)\right)\delta\left(y_1 - y_2\right)\delta\left(z_1 - z_2\right) \\ &\propto \frac{\delta\ \left(\xi_1 - \xi_2\right)\delta\left(y_1 - y_2\right)\delta\left(z_1 - z_2\right)}{|a_{latt}|}. \end{aligned} \tag{2.38}$$

Using Eq. 2.30 we find that

$$\frac{U}{E_R} = a_{\text{latt}} f_2\left(\frac{V_0}{E_R}\right). \tag{2.39}$$

The dependence of U and J on $\frac{V_0}{E_R}$ via f_1 and f_2 cannot by given explicitly so that we consider the limiting case of $\frac{V_0}{E_R} \gg 1$. In this limit we approximate the periodic potential by a harmonic potential near $x = 0$

$$V = V_0 \sin^2\left(k_{latt} x\right) \approx V_0 k_{\text{latt}}^2 x^2 = \frac{1}{2} m\omega^2 x^2, \tag{2.40}$$

where $\omega^2 = \frac{4V_0 E_R}{\hbar^2}$. With this we approximate the "Wannier functions" to be the ground state of the harmonic oscillator which is a Gaussian function

$$W(x) = \frac{1}{\sqrt{\sqrt{\pi} x_0}} e^{-\frac{x^2}{2x_0^2}} \quad \text{with} \quad x_0 = \left(\frac{E_R}{V_0}\right)^{1/4} \frac{a_{\text{latt}}}{\pi}. \tag{2.41}$$

This allows us to calculate the asymptotic value of the Hubbard interaction via Eq. 2.31

$$\frac{U}{E_R} = \sqrt{\frac{32}{\pi^3}} \hbar\omega_\perp a_s a_{\text{latt}} \left(\frac{V_0}{E_R}\right)^{1/4}, \tag{2.42}$$

which agrees with the prediction of Eq. 2.39. The value for the hopping parameter in this approximation does not give accurate results because the tails of the exact Wannier functions are not well accounted for by Gaussian functions. However, we can still obtain the asymptotic form of J by looking at the asymptotic behaviour of the Mathieu function which is the exact solution of Eq. 2.21. As described in [8] one obtains

$$\frac{J}{E_R} \approx \frac{4}{\sqrt{\pi}} \left(\frac{V_0}{E_R}\right)^{3/4} e^{-\frac{\pi^2}{4}\sqrt{\frac{V_0}{E_R}}}. \tag{2.43}$$

$\frac{J}{E_R}$ is only implicitly dependent on a_{latt} since $E_R \propto a_{\text{latt}}^{-2}$. As a side remark we note that another option to obtain an approximation for J is to use the bandwidth $E_{n,\pi} - E_{n,0}$ of the n-th band

$$4J \approx E_{1,\frac{\pi}{a_{\text{latt}}}} - E_{1,0}, \tag{2.44}$$

where $E_{1,\frac{\pi}{a_{\text{latt}}}}$ denotes the energy of the first band at the momentum $\frac{\pi}{a_{\text{latt}}}$. This can be understood by looking at the dispersion relation for the Hubbard model [8]

$$E_k = -2\ J\cos(k a_{\text{latt}}). \tag{2.45}$$

In summary, the parameters J and U can be tuned independently via the optical lattice parameters V_0 and a_{latt} since

$$\frac{U}{E_R} = a_{\text{latt}} f_1\left(\frac{V_0}{E_R}\right) \qquad \frac{J}{E_R} = f_2\left(\frac{V_0}{E_R}\right), \tag{2.46}$$

with some functions f_1 and f_2. Independent of the optical lattice, U can also be tuned via a magnetic field B using the dependence of the s-wave scattering length a_s on the magnetic field [7]. For more details see, e.g, [8, 16]

2.3.2. Numerical results

For later use of the Wannier functions and to test the previous analytical results we calculate numerically the energy bands, denoted by different values of the band index α, in the reduced Brillouin-zone for different potential strengths, see Fig. 2.3. For $V_0 = 0$ we obtain a quadratic disperson relation. With increasing V_0 the dispersion relation gets increasingly modified and band gaps start to emerge. The gap between the first and the second band can be calculated using perturbation theory which gives $V_0/2$, see e.g. [32]. The gap emerges because the potential breaks the degeneracy of the states at the Brillouin-zone boundary and leads to one eigenvector whose maxima are located at the minima of the potential and one where the maxima coincide with the maxima of the potential. The band gap rapidly decreases for higher bands. In addition, with increasing V_0 the first energy band gets flatter and the shape changes from a parabolic to a cosine shape as predicted by Eq. 2.45, see Fig. 2.4a. In the following we compare Wannier functions obtained via Eq. 2.24 for different potential strengths. Already for weak potentials such as $V_0 = 4\ E_R$ we observe that the most significant overlap between two wave functions is between nearest neighbors, see Fig. 2.4b. We observe that while being delocalized for $V_0 = 0$ the tails get strongly suppressed with increasing potential strength and already for $V_0 = 5\ E_R$ the Wannier function is almost completely localized at one lattice site, see Fig. 2.5a. The Wannier functions are exponentially localized as predicted in [31] for maximally localized Wannier functions, see Fig. 2.5b. Deviations from the

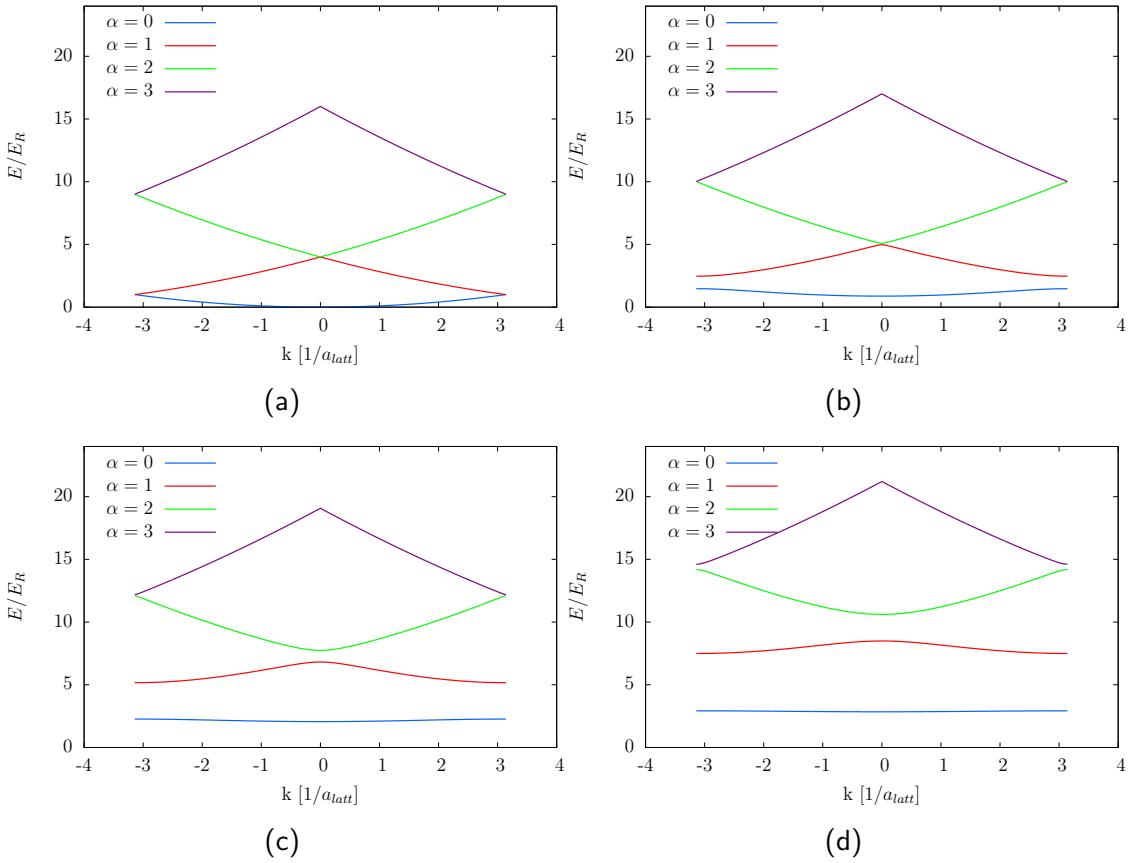

Figure 2.3.: Band structure of an 1D optical lattice described by Eq. 2.21 for different potential amplitudes V_0. (a) $V_0 = 0$, (b) $V_0 = 2\ E_R$, (c) $V_0 = 6E_R$, and (d) $V_0 = 10E_R$. α marks the band index in (a) - (d).

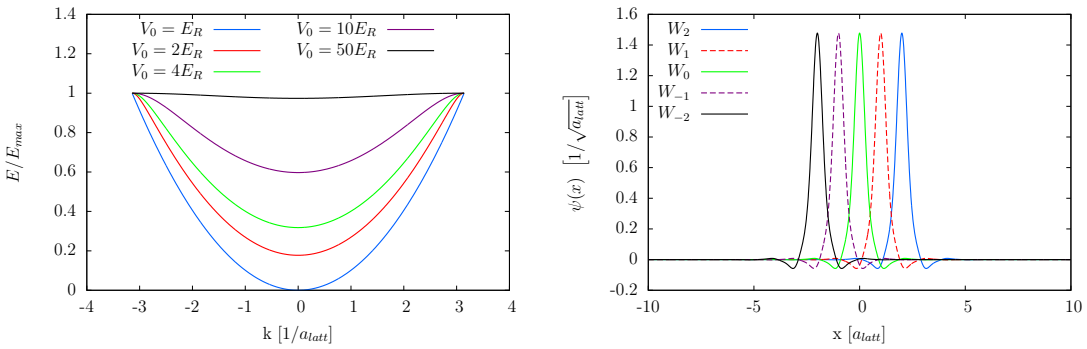

(a) (b)

Figure 2.4.: (a) Shape of the first energy band normalized to $E_{\max} = E\left(\frac{\pi}{a_{\text{latt}}}\right)$ with increasing V_0. (b) Wannier functions for $V_0 = 0.4\ E_R$. The overlap with the nearest neighbor is much larger than with the next-nearest neighbor.

strictly exponential decay are a numerical effect. Having obtained the Wannier functions we compute J and U using Eq. 2.26 and Eq. 2.31 and compare our results with the asymptotic forms of J and U, see Fig. 2.6a and Fig. 2.6b. In the inset we see that the difference between the estimate using the bandwidth, Eq. 2.44, and the numerically exact calculation fits very well. For small V_0 the asymptotic form, Eq. 2.43, does not provide a good estimate for the hopping parameter. For $V_0 > 10\ E_R$ both approximations agree very well with the numerical result. The asymptotic from of U does not fit as good but still gives a good prediction for the trend.

Finally, we test whether direct hopping to other lattice points than the nearest one can indeed be neglected. In Fig. 2.6c we clearly see that this simplification is correct even for rather small V_0 since J_2 and J_3 are orders of magnitude smaller than J. We thus will take into account only nearest neighbor hopping as usual.

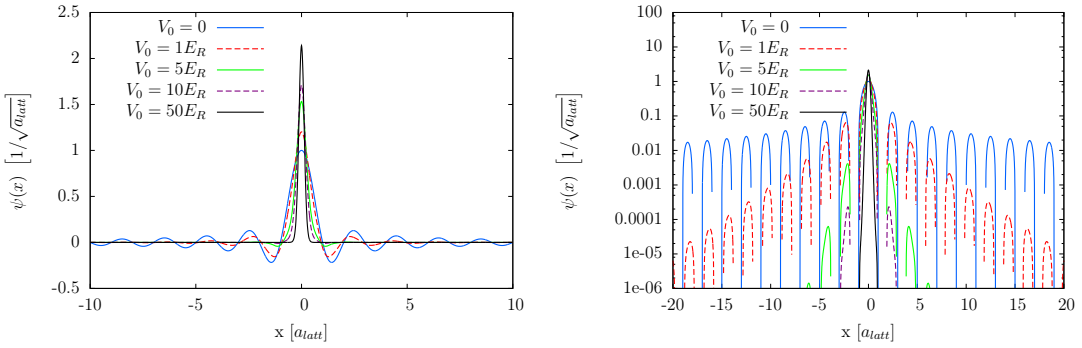

(a) (b)

Figure 2.5.: Wannier functions for different potential strengths, (a) linear plot, (b) logarithmic plot.

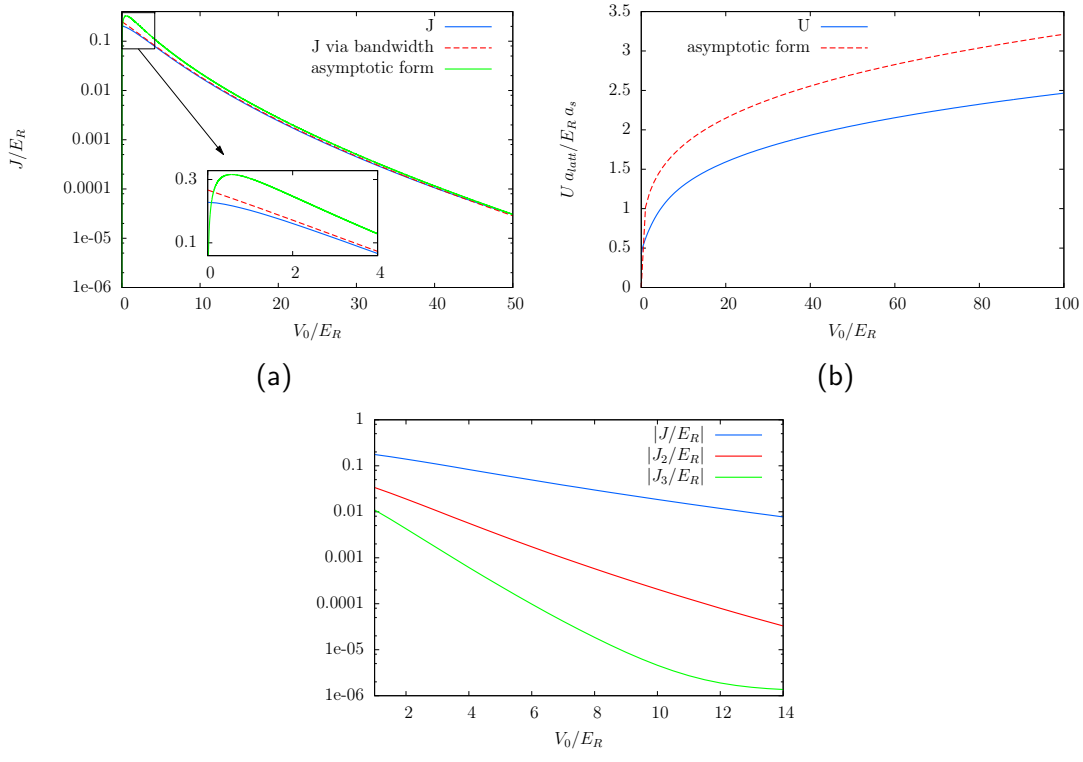

(a) (b)

(c)

Figure 2.6.: Comparison of the numerically obtained hopping parameter J (a) with the theoretical predictions via the bandwidth, Eq. 2.44, and the asymptotic form, Eq. 2.43, and (b) the interaction parameter U with the theoretical prediction, Eq. 2.42. (c) Comparison of the numerically obtained hopping parameters for the nearest, Eq. 2.26, the next-nearest, Eq. 2.27, and the next-next nearest neighbor, Eq. 2.28.

3. Correlations and reduced-density matrices

Correlations are an ubiquitous feature of quantum many-body systems which need to be accounted for within every theoretical method if one wants to obtain observables with a certain accuracy. They are at the core of the computational complexity of quantum mechanics. Going back to classical statistical mechanics, correlations are a well-defined measure that allow to determine the dependence of two variables, say x and y, on one another based on a joint probability distribution $P_{X,Y}(x,y)$,

$$\mathrm{Cor}(x,y) = \frac{\langle (x - \langle x \rangle)\,(y - \langle y \rangle) \rangle}{\sigma_x \sigma_y}, \tag{3.1}$$

where $< ... >= \int \mathrm{d}x \int \mathrm{dy}(...)\mathrm{P_{X,Y}(x,y)}$ and

$$\sigma_y = \sqrt{< x^2 > - < x >^2}, \tag{3.2}$$

$$\sigma_y = \sqrt{< y^2 > - < y >^2} \tag{3.3}$$

are the standard deviations of x and y [33]. The correlation measure (Eq. 3.1) vanishes if the probability distribution factorizes $P_{X,Y}(x,y) = P_X(x)P_Y(y)$ and the particles are then called uncorrelated. This is an example for a two-particle correlation function, i.e. a correlation function of second order but the concept of correlations is not limited to second order but can be extended to higher orders.
In quantum mechanics a universal definition of correlations is absent and many different concepts are frequently used [22]. In general an uncorrelated many-body quantum state can be described via a Hartree-Fock configuration, i.e. an anti-symmetric product state of one-body wave functions which is strictly possible only for non-interacting systems [17–19]. Solving the Hartree-Fock equations includes the effects of the exchange interaction due to the non-local exchange-term that appears in the equations [34]. For interacting systems a single Hartree-Fock determinant is no longer a solution to the N-body system. To describe such a correlated system one can, e.g., use a superposition of Hartree-Fock wave functions, i.e. the so called configuration interaction approach, or treat the problem perturbatively starting from the behavior of the non-interacting system [2, 35]. All corrections that improve the Hartree-Fock approximation are usually ascribed to correlations [17–19].

One of the first definitions of the p-order correlation for a many-body quantum system was given by Glauber [36, 37] for a bosonic systems, i.e. photons in the electromagnetic field. He defined a wave to be m-th order coherent, if it can be factorized into a product of a single function [37]. The coherence measure introduced by Glauber is defined for bosonic systems but could in principle be used for fermionic systems if adapted accordingly. As we will show later, our measure for correlations is closely related to the measure of coherence developed by Glauber. We distinguish different orders of correlations in the same way as for coherence [37], e.g., two-particle correlations, three-particle correlations and so on. To understand the influence of correlations on a physical system we study how correlations change with interaction strength and how they build up from an uncorrelated Hartree-Fock state. To do so, a setup which allows variation of the interaction strength in a broad interval and whose physics can be described by a simple model is desirable. A recently available experimental realization was achieved with ultra-cold atoms in optical lattices which can be described theoretically with the Hubbard model to very high accuracy [7], see Sec. 2. One of the outstanding properties of ultra-cold atoms in optical lattices is that one can investigate both the non-interacting as well as the interacting system and use the former as a reference for the latter. We will use this model throughout this thesis to investigate correlations.

3.1. Reduced-density matrices

In the course of this thesis we use different measures of correlations which all depend on reduced-density matrices. We use the concept of the p-particle reduced density matrix (p-RDM) [17, 38]. To obtain the p-RDM we trace out $(N-p)$ coordinates of the system,

$$D\left(z_1,...,z_p;z_1',...,z_p'\right) = \\ \frac{N!}{(N-p)!}\int \Psi^*\left(z_1,...,z_p,z_{p+1},...,z_N\right)\Psi\left(z_1',...,z_p',z_{p+1},...,z_N\right)\mathrm{d}z_{p+1}...\mathrm{d}z_N, \quad (3.4)$$

with $z_i=(x_i,\sigma_i)$, x_i being the spatial coordinates and $\sigma\epsilon\left(\uparrow,\downarrow\right)$ the spin. N is the total number of particles. Following [23] we normalize the p-RDM to

$$\int D\left(z_1,...,z_p;z_1,...,z_p\right)\mathrm{d}z_1...\mathrm{d}z_p = \frac{N!}{(N-p)!}. \quad (3.5)$$

For simplicity, we introduce a shorthand notation for the p-RDM following [39]

$$D\left(z_1,...,z_p;z_1',...,z_p'\right) = D_{1...p}. \quad (3.6)$$

Expanding the p-RDMs in a spin orbital basis $\phi_i(z)=\phi_i(x)\otimes|\sigma\rangle$

$$D_{1...p} = \sum_{i_1,..,i_p,j_1,..,j_p} D^{i_1...i_p}_{j_1...j_p}\phi_{i_1}\left(z_1\right)...\phi_{i_p}\left(z_p\right)\phi^*_{j_1}(z_1')...\phi^*_{j_p}(z_p'), \quad (3.7)$$

helps interpreting the individual contributions and enhances the numerical efficiency [23]. The orbital indices i, j run from one to the maximum number of spin-orbitals M. For simplicity, we drop the explicit label for the expansion coefficients of the p-RDM, e.g. $D^{i_1 i_2}_{j_1 j_2} = [D_{12}]^{i_1 i_2}_{j_1 j_2}$, since the different orders can be identified unambiguously by the number of indices. The p-RDM expansion coefficients can be written in second quantization [40] using the creation (annihilation) operators $\hat{a}_i(\hat{a}_i^\dagger)$ as

$$D^{i_1 \dots i_p}_{j_1 \dots j_p} = \langle \Psi | \, \hat{a}^\dagger_{i_1} \dots \hat{a}^\dagger_{i_p} \hat{a}_{j_p} \dots \hat{a}_{j_1} \, | \Psi \rangle \, . \tag{3.8}$$

This allows us to interpret the p-RDM coefficients as transition matrix elements for a process where p particles in the orbitals $\phi_{j_1}, ..., \phi_{j_p}$ are destroyed and p particles in the orbitals $\phi_{i_1}, ..., \phi_{i_p}$ are created [40]. For a fermionic system normalized correlation functions as defined by Glauber [36, 37] are not meaningful because they are not equal to one for a Hartree-Fock state due to the anti-symmetrization. To quantify correlation we need to determine whether particles are independent of each other or not [17]. The physical objects assessing this are cumulants [42]. The p-particle cumulant $\Delta_{1..p}$ is the part of the p-RDM that can not be expressed through lower order cumulants and RDMs. For non-interacting systems, i.e. systems which can be described with a single Slater determinant, all cumulants except for the first order vanish [43]. Hence they are a more suitable measure for correlations than the p-RDMs themselves . The relations between the p-RDMs and the p-particle cumulants for $p \leq 4$ are

$$D_1 = \Delta_1 \tag{3.9a}$$
$$D_{12} = 2D_1 \wedge D_1 + \Delta_{12} \tag{3.9b}$$
$$D_{123} = 6D_1 \wedge D_1 \wedge D_1 + 9\Delta_{12} \wedge D_1 + \Delta_{123} \tag{3.9c}$$
$$D_{1234} = 24D_1 \wedge D_1 \wedge D_1 \wedge D_1 + 72\Delta_{12} \wedge D_1 \wedge D_1 + 18\Delta_{12} \wedge \Delta_{12} + 16\Delta_{123} \wedge D_1 + \Delta_{1234}, \tag{3.9d}$$

where the wedge product is the antisymmetrized tensor product

$$D_{1\dots a} \wedge D_{1\dots b} = \frac{1}{[(a+b)!]^2} \sum_{\pi,\sigma} \mathrm{sgn}(\pi)\mathrm{sgn}(\sigma) D^{i_{\pi(1)} \dots i_{\pi(a)}}_{j_{\sigma(1)} \dots j_{\sigma(a)}} D^{i_{\pi(a+1)} \dots i_{\pi(a+b)}}_{j_{\sigma(a+1)} \dots j_{\sigma(a+b)}}, \tag{3.10}$$

and the sums run over all permutations π and σ [44]. Let us note that the p-RDM can be reconstructed from the q-RDMs and q-particle cumulants with $q < p$ except for one term, i.e. the p-particle cumulant, see Eq. 3.9a - 3.9d. The expansion for D_{12} consists of the antisymmetrized product of D_1 and one part which can not be described via D_1 that stems from correlations. For a Hartree-Fock state $\Delta_{12} = 0$ and we have $D_{12} = 2D_1 \wedge D_1$ exactly. For D_{123}, Eq. 3.9c, the first term is the Hartree-Fock contribution one would obtain for non-interacting particles. The

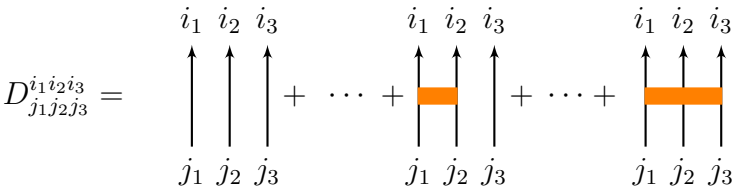

Figure 3.1.: Graphical representation of the terms contributing to D_{123}. Straight lines correspond to the full 1-RDM and the orange boxes symbolize the full interaction vertex. The dots represent terms that can be obtained from the previous term via permutations but are topologically different. The full interaction vertex is a sum of all possible interactions that can take place.

second term describes the correlation of two particles with each other, while the evolution of the third particle is independent of the two remaining particles and the last term is Δ_{123} which describes three-particle correlations. Using a graphical representation for D_{123}, see Fig. 3.1, we demonstrate how to calculate the prefactors in Eq. 3.9c using combinatorics. The diagram shown in Fig. 3.1, and all similar diagrams in this work, are intended to give a qualitative interpretation of the building blocks. Due to the antisymmetric tensor product, Eq. 3.10, each term is divided by the number of topologically distinct graphs. This is corrected for by the prefactors since each graph has to enter with the same weight. The graphical representation is used in analogy to the graphical representation of Green's functions, see e.g. [45, 46]. For the first term, the Hartee-Fock term, there exist 3! possibilities to exchange the lower and 3! possibilities to exchange the upper indices. Yet exchanging complete arrows with each other, e.g. $i_1 \leftrightarrow i_2$ and $j_1 \leftrightarrow j_2$, does not give topologically different diagrams. There are 3! possibilities to do so. This makes $\frac{3!\cdot 3!}{3!} = 6$ possible configurations. For the second diagram, i.e. the correlation of two particles with each other, we again have 3! possibilities to order the lower and the upper indices, respectively. However we have $2!\cdot 2$ possibilities to exchange the indices of the two-particle cumulant. Thus we obtain $\frac{3!\cdot 3!}{2!\cdot 2!} = 9$ possible configurations. The cumulant Δ_{12} contains the full interaction vertex, i.e. the sum over of all possible collisions between two particles. All other interactions, i.e. collisions involving three particles, are taken into account in the last term, the three-particle cumulant Δ_{123}.

We give a short interpretation of the individual RDMs and cumulants. The diagonal of the 1-RDM, $D(z;z)$, is the spin-dependent density of the system and the diagonal of the 2-RDM $D(z_1, z_2; z_1, z_2)$ corresponds to the spin dependent pair-density, i.e. the probability to find a pair of particles, one with coordinate z_1 and one with coordinate z_2. Tracing out the spin degree of freedom we obtain the usual density and pair density [2, 3]. The diagonal elements of the 1-RDM $D^i_i = n_i$ can be interpreted as a mean occupation number of orbital ϕ_i, and the diagonal elements of the

2-RDM D_{ij}^{ij} represents the mean occupation of the orbital pair (ϕ_i, ϕ_j) [24, 47]. The diagonal of Δ_{ij}^{ij} can be interpreted as the correlation between fluctuations of the occupation of the corresponding orbitals ϕ_i and ϕ_j which is called covariance [47]. This can be extended to higher order cumulants, e.g. Δ_{ijk}^{ijk} measures the correlation between fluctuations of the occupation numbers of (ϕ_i, ϕ_j, ϕ_k) and so on [47]. The orbitals $\phi_1, ..., \phi_M$ are called working orbitals.
Because the p-RDMs are hermitian it is always possible to choose a basis in which they are diagonal. The so obtained eigenvalues of the 1-RDM (2-RDM) are called natural occupation numbers $\lambda^{(1)}$ (geminal occupation numbers $\lambda^{(2)}$) and the corresponding eigenfunctions natural orbitals (geminals), see e.g. [48].

3.2. Hierarchy of density matrices

The time evolution of density matrices is controlled by the von-Neumann equation [34]

$$i\hbar\frac{\partial}{\partial t}\hat{\rho} = \left[\hat{H}, \hat{\rho}\right]. \tag{3.11}$$

The N-particle many-body Hamiltonian

$$\hat{H} = \sum_{i=1}^{N} h(z_i) + \frac{1}{2}\sum_{i\neq j=1}^{N} V_{\text{int}}(z_i, z_j), \tag{3.12}$$

consists of a one-body part, $h(z_i) = -\frac{\hbar^2}{2m}\Delta_i + V_{\text{ext}}(z_i)$, containing the kinetic part and the external one-body potential V_{ext}, and the two-body interaction potential V_{int}. To obtain the equations of motion for the p-RDMs we trace out $N-p$ particles and get

$$i\hbar\frac{\partial}{\partial t}D_{1\dots p} = \left[\hat{H}_{1\dots p}, D_{1\dots p}\right] + \text{Tr}_{\text{p+1}}\left(\sum_{i=1}^{p}\left[V_{i,p+1}, D_{1\dots p+1}\right]\right), \tag{3.13}$$

where $\hat{H}_{1\dots p}$ is the p-particle Hamiltonian in analogy to Eq. 3.12, $V_{i,p+1} = V_{\text{int}}(z_i, z_{p+1})$ is the interaction term, and $\text{Tr}_{\text{p+1}}$ denotes the trace over particle $p+1$ [39]. Eq. 3.13 is known as the Bogoliubov-Born-Green-Kirkwood-Yvon (BBGKY)-hierarchy and differs from Eq. 3.11 by the last term that couples the time evolution of the p-RDM with the (p+1)-RDM. Individual equations of this hierarchy are, thus, not closed. Solving the complete BBGKY-hierarchy amounts to solving the full N-particle Schrödiger equation and is numerically impossible for even just a few particles. Hence, in order to solve these equations we need to truncate them at some point.
In the following we truncate the BBGKY-hierarchy at the second level thus fully incorporating two-particle correlations. Note that the 2-RDM is sufficient to calculate

$$\Delta^{i_1 i_2 i_3}_{j_1 j_2 j_3} \approx$$

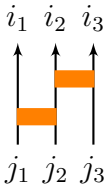

Figure 3.2.: The extension to the Valdemoro approximation found by Yasuda and Nakatsuji [45, 46] approximates Δ_{123} as combination of two separate two-particle interactions. The propagator connecting the two vertices is not the exact single-particle propagator but the so called Hartree-Fock reference [45, 46, 51].

the energy of a given quantum many-body system by [48]

$$E = \left\langle \hat{H} \right\rangle = \frac{1}{2} \int H_2(x_1, x_2) D_{12} \mathrm{d}x_1 \mathrm{d}x_2 = \frac{1}{2} \mathrm{Tr}\left(H_2 D_{12}\right), \tag{3.14}$$

with

$$H_2(x_1, x_2) = \frac{h(x_1) + h(x_2)}{N-1} + V_{\mathrm{int}}(x_1, x_2). \tag{3.15}$$

This fact has triggered a lot of interest for the ground state calculations of molecules in quantum chemistry [40, 48, 49].
Truncating at p=2, the equations of motion for the 2-RDM are

$$i\hbar \frac{\partial}{\partial t} D_{12} = \left[\hat{H}_{12}, D_{12}\right] + \mathrm{Tr}_3\left(\left[V_{1,3} + V_{2,3}, D_{123}\right]\right) = \left[\hat{H}_{12}, D_{12}\right] + C_{12}\left[D_{123}\right], \tag{3.16}$$

where $C_{12}\left[D_{123}\right]$ is the collision operator [23]. To close the equation we approximate the 3-RDM via the 2-RDM and the 1-RDM. One of the approximations we use is the Valdemoro reconstruction [50] given in Eq. 3.9c by setting $\Delta_{123} = 0$, and thereby neglecting three-particle correlations (see below). An extension of the Valdemoro reconstruction was found by Yasuda and Nakatsuji [45, 46] via the inclusion of a diagram to the approximation where one output channel of a two-particle vertex is coupled to the input channel of another two-particle vertex (Fig. 3.2). This is an effective three-particle interaction and an approximation for Δ_{123} given by

$$\Delta^{i_1 i_2 i_3}_{j_1 j_2 j_3} \approx \mathcal{A} \sum_{a,b} \Delta^{i_1 a}_{j_1 j_2} R^b_a \Delta^{i_2 i_3}_{b j_3}, \tag{3.17}$$

where $\mathcal{A}$ denotes the antisymmetrization of this product [51]. The so called Hartree-Fock reference, R^b_a, is a diagonal matrix in the natural orbital basis of D_1. Ordering the natural orbitals according to the weight of the natural occupation numbers $\lambda^{(1)}$ the first N diagonal entries of R^y_x are equal to 1, with N being the number of particles and the other $M - N$ entries are equal to -1, with M being the total number of

spin orbitals. Transforming this matrix back into the basis of the working orbitals $(\phi_1, ..., \phi_M)$ we obtain R^b_a given in Eq. 3.17.
These two reconstructions for D_{123} violate the spin and energy conservation during the propagation as was pointed out by Lackner et al. [23], see App. A. In [23] the contraction consistent (CC) reconstruction has been developed, which includes those parts of the three-particle cumulant that guarantee energy and spin conservation. In the course of this thesis we use the abbreviation **Val** for the Valdemoro reconstruction Eq. 3.9c, **Val+CC** for the contraction consistent Valdemoro reconstruction [23], **NY** for the reconstruction with the approximation for Δ_{123} by Yasuda and Nakatsuji [45, 46], and **NY+CC** for the contraction consistent version of the latter.

3.3. N-representability problem and purification

Despite the considerable level of sophistication, none of the used reconstructions for the 3-RDM ensures that the N-representability of the 2-RDM is preserved during propagation. N-representability describes the fact that the 2-RDM is indeed associated with a many-body wave function of N indistinguishable particles [23, 40, 48]. This problem was first encountered when trial 2-RDMs were used in a variational approach to determine the ground state energy of a many-body system. The obtained energies were below the exact results [49, 52]. One further distinguishes between N-representability and ensemble N-representability where a reduced density-matrix is obtained from a density matrix rather from a pure state. The ensemble N-representability problem was solved for the 1-RDM [48] but for higher order p-RDMs only very recently a constructive method for all conditions was found [53]. However the actual usage of all these conditions is beyond our present numerical implementations [23].

3.3.1. N-representability for D_1 and D_{12}

To review the most important N-representability conditions [23, 40] we use the 2-RDM in second quantization, Eq. 3.8, reproduced here for simplicity

$$D^{i_1 i_2}_{j_1 j_2} = \langle \Psi | \, \hat{a}^\dagger_{i_1} \hat{a}^\dagger_{i_2} \hat{a}_{j_2} \hat{a}_{j_1} \, | \Psi \rangle \, . \tag{3.18}$$

In analogy, the p-hole reduced-density matrix (p-HRDM) is given by

$$Q^{i_1 ... i_p}_{j_1 ... j_p} = \langle \Psi | \, \hat{a}_{j_1} ... \hat{a}_{j_p} \hat{a}^\dagger_{i_p} ... \hat{a}^\dagger_{i_1} \, | \Psi \rangle \, , \tag{3.19}$$

which describes the destruction of holes in the orbitals $\phi_{i_1}, ..., \phi_{i_p}$ (by creating particles) and creation of holes in the orbitals $\phi_{j_1}, ..., \phi_{j_p}$. For the 1-RDM to be ensemble N-representable it is sufficient that Q_1 and D_1 are semidefinite, i.e. that

they have non-negative eigenvalues. It is important to note that both conditions are independent of each other although Q_1 and D_1 are related via the fermionic anti-commutation relation [48]. The N-representability conditions for the 1-RDM amount to the fact that there are neither negative occupation numbers for particles nor for holes.
In a similar way for the 2-RDM, D_{12} and Q_{12} have to be positive semi-definite. However, these conditions are not sufficient and do not guarantee that the 2-RDM is N-representable [40, 53]. In previous applications of the TD-2RDM for molecules in laser fields a restriction to these two N-representability conditions was sufficient to obtain results in very good agreement with exact calculations [23].

3.3.2. Purification

Although the initial 2-RDM is N-representable, $D_{12}(t > 0)$ will, in general, not be N-representable if propagated via Eq. 3.16 with a reconstructed 3-RDM [23]. Over time an error will accumulate. This accumulation of error leads to instabilities in the propagation [23, 24]. To solve this problem, the 2-RDM is modified after each time step to obey certain preselected N-representability conditions. In accordance with literature we call this modification of D_{12} purification [23, 40, 54]. The purification scheme used in [23] applies two N-representability conditions, i.e. that D_{12} and Q_{12} have to be positive-semidefinite. These conditions were sufficient to stabilize the propagation. However, this purification scheme does not preserve the total energy. The purification scheme is based on work by Alcoba [40, 55]. Hence we call this purification scheme **Alcoba purification** in the following.
We develop an alternative purification scheme that only takes into account that D_{12} has to be positive semidefinite and incorporates conservation of energy. Within this purification energy conservation thus comes at the price of the positive-semidefiniteness of the two-hole reduced-density matrix Q_{12}. This means that the probability to find two holes simultaneously can be negative which is not physical. The eigenvalues of D_{12} correspond either to an anti-symmetric spin wave function, i.e. singlet configuration, or to a symmetric spin wave function, i.e. triplet configuration [40]. The total spin is equal to one for the triplet configuration and zero for the singlet configuration. The magnetic spin quantum number of the singlet state is zero while the triplett state has three different configurations, i.e. $(1, 1)$, $(1, 0)$ and $(1, -1)$. The individual spin configurations can be associated with individual blocks of the

2-RDM [40]:

$$\text{Singlet} : S^2 = 0$$

$$\left[D^{0,0}\right]^{i_1 i_2}_{j_1 j_2} = D^{i_1\uparrow i_2\downarrow}_{j_1\uparrow j_2\downarrow} + D^{i_1\uparrow i_2\downarrow}_{j_2\uparrow j_1\downarrow} \qquad S_z = 0 \tag{3.20a}$$

$$\text{Triplet} : S^2 = \frac{3}{4}\hbar^2$$

$$\left[D^{1,1}\right]^{i_1 i_2}_{j_1 j_2} = D^{i_1\uparrow i_2\uparrow}_{j_1\uparrow j_2\uparrow} \qquad S_z = \hbar \tag{3.20b}$$

$$\left[D^{1,0}\right]^{i_1 i_2}_{j_1 j_2} = D^{i_1\uparrow i_2\downarrow}_{j_1\uparrow j_2\downarrow} - D^{i_1\uparrow i_2\downarrow}_{j_2\uparrow j_1\downarrow} \qquad S_z = 0 \tag{3.20c}$$

$$\left[D^{1,-1}\right]^{i_1 i_2}_{j_1 j_2} = D^{i_1\downarrow i_2\downarrow}_{j_1\downarrow j_2\downarrow} \qquad S_z = -\hbar. \tag{3.20d}$$

The indices of the 2-RDMs in Eq. 3.20 are spatial indices. The geminal occupation numbers (eigenvalues) of the triplet configuration, $\lambda^{(2)}_{\text{triplet}}$, are three times degenerate within the full 2-RDM [40]. After each propagation step we decompose the 2-RDM into the singlet and the triplet part and calculate the corresponding geminal occupation numbers $\lambda^{(2)}_{\text{singlet}}$ and $\lambda^{(2)}_{\text{triplet}}$. For the triplet part we set all negative $\lambda^{(2)}_{\text{triplet}}$ to zero and modify the largest triplet geminal occupation number such that the sum of all triplet occupation numbers stays constant for $D^{1,-1}, D^{1,0}$ and $\mathrm{D}^{1,1}$ separately,

$$\sum_k \left[\lambda^{(2)}_{\text{triplet}}\right]_k = \mathrm{Tr}\left(\mathrm{D}^{1,-1}\right) = \mathrm{Tr}\left(\mathrm{D}^{1,0}\right) = \mathrm{Tr}\left(\mathrm{D}^{1,1}\right) = \text{const.} \tag{3.21}$$

For the singlet part we set all negative $\lambda^{(2)}_{\text{singlet}}$ to zero and modify the two largest singlet occupation numbers such that the sum of all $\lambda^{(2)}_{\text{singlet}}$ and the energy is constant

$$\sum_i \left[\lambda^{(2)}_{\text{singlet}}\right]_i = \mathrm{Tr}\left(\mathrm{D}^{0,0}\right) = \text{const.} \tag{3.22}$$

$$\sum_i \left[\lambda^{(2)}_{\text{singlet}}\right]_i \left\langle g_i^{(singlet)} \middle| H \middle| g_i^{(singlet)} \right\rangle + \sum_k \left[\lambda^{(2)}_{\text{triplet}}\right]_k \left\langle g_k^{(triplet)} \middle| H \middle| g_k^{(triplet)} \right\rangle = \text{const.} \tag{3.23}$$

Eq. 3.23 corresponds to the evaluation of the energy functional Eq. 3.14 in spectral representation. $\left|g_i^{(singlet)}\right\rangle$ $\left(\left|g_k^{(triplet)}\right\rangle\right)$ is the the singlet (triplet) geminal corresponding to the singlet (triplet) geminal occupation number $\left[\lambda^{(2)}_{\text{singlet}}\right]_i$ $\left(\left[\lambda^{(2)}_{\text{triplet}}\right]_k\right)$. The conditions given in Eq. 3.22 and Eq. 3.23 result in two linear equations for the two largest singlet geminal occupation numbers $\lambda^{(2)}_{\text{singlet}}$ which can be solved exactly. If the solution results in negative geminal occupation numbers $\lambda^{(2)}_{\text{singlet}}$ we neglect the energy conservation, Eq. 3.23, and just enforce that the trace of the singlet

part is constant, Eq. 3.22. This is done because we perform the purification in order to obtain a 2-RDM where all geminal occupation numbers are greater zero $\lambda^{(2)} > 0$. We then use the new geminal occupation numbers $\tilde{\lambda}^{(2)}_{\text{singlet}}$ and $\tilde{\lambda}^{(2)}_{\text{triplet}}$, and the corresponding geminals to reconstruct D_{12},

$$D_{12} = \sum_i \left[\tilde{\lambda}^{(2)}_{\text{singlet}}\right]_i \left|g_i^{(singlet)}\right\rangle \left\langle g_i^{(singlet)}\right| + \sum_k \left[\tilde{\lambda}^{(2)}_{\text{triplet}}\right]_k \left|g_k^{(triplet)}\right\rangle \left\langle g_k^{(triplet)}\right| . \tag{3.24}$$

Note that the geminals are not changed during the purification step.
The energy mismatch created by setting several geminal occupation numbers to zero is fully compensated in the singlet configuration since the energy contribution of the singlet geminals is much larger than the energy contribution of the triplet geminals. Hence the energy mismatch can be compensated with smaller changes in the singlet geminal occupation numbers than in the triplet geminal occupation numbers. We call this energy conserving purification scheme **EC purification** in the following.
For the previous discussion we assumed an even particle number. For odd particle numbers the above described purification schemes have to be modified.

3.4. Correlation measures

We use different measures for correlations based on properties of reduced-density matrices and cumulants. We define the magnitude of the p-particle cumulant given in Eq. 3.9a - 3.9d as

$$|\Delta_{1\ldots p}|^2 = \mathrm{Tr}_{1\ldots \mathrm{p}}\left(\Delta^2_{1\ldots p}\right) = \sum_{i_1,\ldots,i_p;j_1,\ldots,j_p} \left(\Delta^{i_1\ldots i_p}_{j_1\ldots j_p}\right)^2 . \tag{3.25}$$

Note that this measure is basis independent. For a Slater determinant all cumulants except for Δ_1 are strictly zero and therefore all density matrices can be obtained by the anti-symmetrized product of the 1-RDM, Eq. 3.9a - 3.9d, [43]. We choose the absolute magnitude of the p-particle cumulant as the measure for p-particle correlations.
Although cumulants are a very good tool to pin down correlations of arbitrary order within a many-body theory, they are not easily accessible in experiments. Such a measure would be of great interest to understand correlations in experiments.

One proposed option is to measure correlations via the von Neumann entropy [21, 56, 57] based on the natural occupation numbers $\lambda^{(1)}$ of the 1-RDM, and on the geminal occupation numbers $\lambda^{(2)}$ of the 2-RDM

$$S_1 = -\mathrm{Tr}\left(\mathrm{D}_1 \ln(\mathrm{D}_1)\right) \tag{3.26a}$$

$$S_2 = -\mathrm{Tr}\left(\mathrm{D}_{12} \ln(\mathrm{D}_{12})\right) . \tag{3.26b}$$

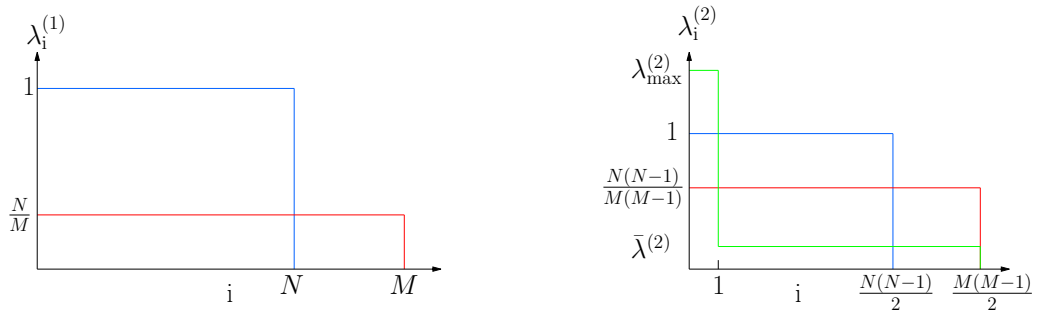

Figure 3.3.: Eigenvalue spectrum for a Hartree-Fock state (blue), and the maximally correlated state (red) for the 1-RDM (a) and the 2-RDM (b). The green curve in (b) corresponds to a state where one geminal is occupied with $\lambda_{\max}^{(2)}$ and the remaining geminals are equally occupied with $\bar{\lambda}^{(2)}$. Such a state is characterized by long-range order [59]. N is the number of particles, M the number of orbitals, and $\lambda_i^{(1)}$ $\left(\lambda_i^{(2)}\right)$ is the i^{th} eigenvalue of the 1-RDM (2-RDM).

To evaluate the expressions in Eq. 3.26 we need the eigenvalues of D_1, the natural occupation numbers $\lambda^{(1)}$, and D_{12}, the geminal occupation numbers $\lambda^{(2)}$. We call the entropies defined in Eq. 3.26 natural entropies in the following. To calculate $\lambda^{(1)}$ and $\lambda^{(2)}$, knowledge of the full 1-RDM and 2-RDM is necessary which is not easily realized in experiments. Hence, we use two similar correlation measures that are accessible in the experiment, e.g. via fluorescence measurements [58], the density entropy for the 1-RDM

$$S_1^{(\rho)} = -\sum_{i_1} D_{i_1}^{i_1} \ln\left(D_{i_1}^{i_1}\right) \tag{3.27a}$$

and the density entropy for the 2-RDM

$$S_2^{(\rho)} = -\sum_{i_1,i_2} D_{i_1 i_2}^{i_1 i_2} \ln\left(D_{i_1 i_2}^{i_1 i_2}\right), \tag{3.27b}$$

where the diagonal elements of $D_{i_1}^{i_1}$ correspond to the mean occupation number of the orbital ϕ_i and the diagonal elements $D_{i_1 i_2}^{i_1 i_2}$ corresponds to the mean occupation number of the orbital pair (ϕ_i, ϕ_j). Expanding $D_{i_1}^{i_1}$ $(D_{i_1 i_2}^{i_1 i_2})$ in a spin-orbital basis, Eq. 3.7, one obtains the spin dependent density (pair-density). The density entropies given in Eq. 3.27a, ?? are not basis independent. Hence, their usage is only useful if there exists a preferred basis. For the Hubbard model this is the basis of the on site orbitals.

To calculate the entropies we normalize the p-RDMs to $\binom{N}{p}$, i.e. different to Eq. 3.5. Doing so the 1-RDM of a single determinant Hartree-Fock state for N particles in M orbitals has N eigenvalues $\lambda^{(1)}$ with $\lambda^{(1)} = 1$ and all remaining being zero. In this normalization the natural entropy of the 1-RDM takes on its minimal value for Hartree-Fock states, i.e.

$$S_1^{\min} = 0. \tag{3.28}$$

Note the difference to entropy measures similar to Eq. 3.26a and Eq. 3.26b where density matrices normalized to one are used to measure entangled states [57, 60]. In this case Hartree-Fock states which are maximally entangled give a maximal value for the von Neumann entropy.
The natural entropy of the 1-RDM is maximal if all natural orbitals M are occupied with the same probability $\lambda_i^{(1)} = \frac{N}{M}$ is given by

$$S_1^{\max} = N \ln\left(\frac{M}{N}\right), \tag{3.29}$$

see Fig. 3.3a.
The 2-RDM of a single determinant Hartree-Fock state has $\frac{N(N-1)}{2}$ non-vanishing eigenvalues $\lambda_i^{(2)}$ with value $\lambda_i^{(2)} = 1$. Thus the minimal natural entropy for the 2-RDM is

$$S_2^{\min} = 0. \tag{3.30}$$

The natural entropy for the 2-RDM is maximal if $\frac{M(M-1)}{2}$ eigenvalues are equally occupied $\lambda^{(2)} = \frac{N(N-1)}{M(M-1)}$. All other geminals are unoccupied due to the anti-symmetry of the 2-RDM, see Fig. 3.3b. Hence the natural entropy of such a 2-RDM is given by

$$S_2^{\max} = \frac{N(N-1)}{2} \ln\left(\frac{N(N-1)}{M(M-1)}\right). \tag{3.31}$$

Note that the minimal and maximal values for $S_1^{(\rho)}$ $\left(S_2^{(\rho)}\right)$ are the same as for S_1 (S_2). The geminal occupation numbers $\lambda^{(2)}$ are, however, not bounded by one. The maximal geminal occupation number is

$$\lambda_{\max}^{(2)} = \frac{N(M-N+2)}{2M}, \tag{3.32}$$

for D_{12} being normalized to $\binom{N}{2}$ [59]. Note that $\lambda_{\max}^{(2)} > 1$ if $M > N$. This implies that the sum in Eq. 3.26b can contain negative terms. The natural entropy S_2 of such a state where one $\lambda^{(2)} > 1$ is smaller than $S_2^{\max}$. This high geminal occupation number is a sign of the condensation of pairs of fermions into the same state [59]. As we will show later, such a state is more correlated than a state where all geminals are equally occupied taking the absolute magnitude of the two-particle cumulant as the measure of two-particle correlations. This is not correctly reproduced by

the entropy. Calculating the natural entropy S_2 for a state where one geminal is occupied with $\lambda^{(2)}_{\text{max}}$ and the remaining geminal occupation numbers are all equal $\bar{\lambda}^{(2)} = \frac{N(MN-2M+N+2)}{M(M^2-M-2)}$, see Fig. 3.3b, we obtain

$$S_2^* = -\lambda^{(2)}_{\text{max}} \ln\left(\lambda^{(2)}_{\text{max}}\right) + \left(\frac{N(N-1)}{2} - \lambda^{(2)}_{\text{max}}\right) \bar{\lambda}^{(2)} \ln\left(\bar{\lambda}^{(2)}\right). \tag{3.33}$$

Since $S_2^* < S_2^{\text{min}}$ but the state described by the former entropy is more correlated than the latter state one has to be careful in using entropy measures to measure correlations using the absolute magnitude of the two-particle cumulant as measure. The state described by S_2^* is called antisymmetric geminal product (AGP) state in literature [61]. The defining property of such a state is that one geminal is occupied by the maximally allowed number of particles, see Eq. 3.32, and all other geminals are evenly occupied, see Fig. 3.3b. An AGP state has built in correlations of infinite range for a homogeneous system in the off-diagonal terms of the 2-RDM [59, 61], i.e. $D^{ii}_{jj} \neq 0$ for $|i-j| \to \infty$. For such a state the natural occupation numbers of the 1-RDM $\lambda^{(1)}_i$ are all equal [61]. Hence, the 1-RDM is diagonal and S_1 is maximal (Eq. 3.29). We will show that in the 1D Hubbard model such states are realized. We will compare the correlation measures based on entropies to the absolute magnitude of the cumulants and test whether the entropy measures can be used as measure for correlations.

4. Time-dependent two-particle reduced density matrix method for the Hubbard model

In this chapter we derive the equations of motion for the 2-RDM for the Hubbard model. In [23] the equations of motion for the 2-RDM where derived for molecules in laser fields. Therein, the orbitals which serve as a basis for the 2-RDM are time-dependent, see Eq. 3.7. For the Hubbard model we chose the orbitals to be time-independent, because the basis set is finite and complete. This simplifies the equations of motion considerably.

4.1. Equations of motion of the 2-RDM

For the Hubbard model the basis in which D_{12} is expanded, see Eq. 3.7, corresponds to static on-site orbitals, i.e. the Wannier functions calculated in the previous chapter. To derive the equations of motion for the Hubbard model we use Eq. 3.16 in orbital representation. Inserting the one-particle $h_{i_1}^{j_1}$ and two-particle elements $V_{i_1 i_2}^{j_1 j_2}$ of the Hamiltonian in the spin-orbital basis

$$h_{j_1}^{i_1} = \langle \phi_{i_1} | h_1 | \phi_{j_1} \rangle \tag{4.1}$$

$$V_{j_1 j_2}^{i_1 i_2} = \langle \phi_{i_1} \phi_{i_2} | V_{12} | \phi_{j_1} \phi_{j_2} \rangle , \tag{4.2}$$

we obtain [23]

$$i\hbar \partial_t D_{j_1 j_2}^{i_1 i_2} = \sum_{k_1 k_2} \left(H_{j_1 j_2}^{k_1 k_2} D_{k_1 k_2}^{i_1 i_2} - D_{j_1 j_2}^{k_1 k_2} H_{k_1 k_2}^{i_1 i_2} \right) + C_{j_1 j_2}^{i_1 i_2}, \tag{4.3}$$

with

$$H_{j_1 j_2}^{i_1 i_2} = h_{j_1}^{i_1} \delta_{j_2}^{i_2} + \delta_{j_1}^{i_1} h_{j_2}^{i_2} + V_{j_1 j_2}^{i_1 i_2} \tag{4.4}$$

$$C_{j_1 j_2}^{i_1 i_2} = I_{j_1 j_2}^{i_1 i_2} + I_{j_2 j_1}^{i_2 i_1} - \left(I_{i_1 i_2}^{j_1 j_2} + I_{i_2 i_1}^{j_2 j_1} \right)^* , \tag{4.5}$$

and

$$I_{j_1 j_2}^{i_1 i_2} = \sum_{k_1, k_2, k_3} V_{j_1 k_1}^{k_2 k_3} D_{k_2 j_2 k_3}^{i_1 i_2 k_1}. \tag{4.6}$$

Using the Hubbard Hamiltonian, Eq. 2.19, we obtain the equations of motion for the Hubbard model with

$$h_{j_1}^{i_1} = -J\left(\delta_{j_1}^{i_1-1} + \delta_{j_1}^{i_1+1}\right) \tag{4.7}$$

and

$$V_{j_1 j_2}^{i_1 i_2} = U\delta_{j_1}^{i_1}\delta_{i_2}^{j_2}\delta_{i_2}^{i_1}. \tag{4.8}$$

Eq. 4.6 then simplifies to

$$I_{j_1 j_2}^{i_1 i_2} = UD_{j_1 j_2 j_1}^{i_1 i_2 j_1} = UD_{j_1 j_1 j_2}^{i_1 j_1 i_2}. \tag{4.9}$$

This implies that we do not need the complete 3-RDM within the Hubbard model but just a rather small fraction of it.
Compared to previous applications of the TD-2RDM [23] the numerical effort is reduced because the evaluation of the collision operator is less expensive. Further, numerical costs are reduced since there is no need to propagate the orbitals.

4.2. Spin symmetry of D_{12}

The 2-RDM can be decomposed into spin blocks out of which those elements are non-zero which have the same total spin in the lower and upper indices [40],

$$D_{t_1 t_2}^{v_1 v_2} = \begin{pmatrix} D_{j_1\uparrow\, j_2\uparrow}^{i_1\uparrow\, i_2\uparrow} & D_{j_1\uparrow\, j_2\downarrow}^{i_1\uparrow\, i_2\uparrow} & D_{j_1\downarrow\, j_2\uparrow}^{i_1\uparrow\, i_2\uparrow} & D_{j_1\downarrow\, j_2\downarrow}^{i_1\uparrow\, i_2\uparrow} \\ D_{j_1\uparrow\, j_2\uparrow}^{i_1\uparrow\, i_2\downarrow} & D_{j_1\uparrow\, j_2\downarrow}^{i_1\uparrow\, i_2\downarrow} & D_{j_1\downarrow\, j_2\uparrow}^{i_1\uparrow\, i_2\downarrow} & D_{j_1\downarrow\, j_2\downarrow}^{i_1\uparrow\, i_2\downarrow} \\ D_{j_1\uparrow\, j_2\uparrow}^{i_1\downarrow\, i_2\uparrow} & D_{j_1\uparrow\, j_2\downarrow}^{i_1\downarrow\, i_2\uparrow} & D_{j_1\downarrow\, j_2\uparrow}^{i_1\downarrow\, i_2\uparrow} & D_{j_1\downarrow\, j_2\downarrow}^{i_1\downarrow\, i_2\uparrow} \\ D_{j_1\uparrow\, j_2\uparrow}^{i_1\downarrow\, i_2\downarrow} & D_{j_1\uparrow\, j_2\downarrow}^{i_1\downarrow\, i_2\downarrow} & D_{j_1\downarrow\, j_2\uparrow}^{i_1\downarrow\, i_2\downarrow} & D_{j_1\downarrow\, j_2\downarrow}^{i_1\downarrow\, i_2\downarrow} \end{pmatrix} = \begin{pmatrix} D_{j_1\uparrow\, j_2\uparrow}^{i_1\uparrow\, i_2\uparrow} & 0 & 0 & 0 \\ 0 & D_{j_1\uparrow\, j_2\downarrow}^{i_1\uparrow\, i_2\downarrow} & D_{j_1\downarrow\, j_2\uparrow}^{i_1\uparrow\, i_2\downarrow} & 0 \\ 0 & D_{j_1\uparrow\, j_2\downarrow}^{i_1\downarrow\, i_2\uparrow} & D_{j_1\downarrow\, j_2\uparrow}^{i_1\downarrow\, i_2\uparrow} & 0 \\ 0 & 0 & 0 & D_{j_1\downarrow\, j_2\downarrow}^{i_1\downarrow\, i_2\downarrow} \end{pmatrix}, \tag{4.10}$$

where $t, v \,\epsilon\, \{1...M\}$ represent the spin orbitals, $i, j \,\epsilon\, \left\{1...\frac{M}{2}\right\}$ represent the spatial orbitals, and $\{\uparrow, \downarrow\}$ symbolize the spin part. Treating a closed shell system, the total spin is zero and the system is invariant under spin flips [23], e.g.

$$D_{j_1\uparrow j_2\downarrow}^{i_1\uparrow i_2\downarrow} = D_{j_1\downarrow j_2\uparrow}^{i_1\downarrow i_2\uparrow}. \tag{4.11}$$

Using further the anti-symmetry of D_{12}, e.g.

$$D_{j_1\uparrow j_2\downarrow}^{i_1\uparrow i_2\downarrow} = -D_{j_1\uparrow j_2\downarrow}^{i_2\downarrow i_1\uparrow}, \tag{4.12}$$

the full 2-RDM can be constructed from the two independent spin-blocks [23, 40]

$$D_{j_1\uparrow j_2\uparrow}^{i_1\uparrow i_2\uparrow} = D_{j_1\downarrow j_2\downarrow}^{i_1\downarrow i_2\downarrow} \qquad \text{and} \qquad D_{j_1\uparrow j_2\downarrow}^{i_1\uparrow i_2\downarrow} = D_{j_1\downarrow j_2\uparrow}^{i_1\downarrow i_2\uparrow} = -D_{j_1\downarrow j_2\uparrow}^{i_2\uparrow i_1\downarrow} = -D_{j_2\uparrow j_1\downarrow}^{i_1\downarrow i_2\uparrow}. \tag{4.13}$$

For a closed shell system where S_z and S^2 are conserved the two spin blocks can be related to another via [23]

$$D^{i_1\uparrow i_2\uparrow}_{j_1\uparrow j_2\uparrow} = D^{i_1\uparrow i_2\downarrow}_{j_1\uparrow j_2\downarrow} - D^{i_1\uparrow i_2\downarrow}_{j_2\uparrow j_1\downarrow}. \tag{4.14}$$

The Hubbard Hamiltonian 2.19 depends on the spin but every single term of the Hamiltonian conserves the spin and does not induce spin-flips such that it commutes with S_z and S^2. One can, therefore, restrict oneself to the equations of motion of $D^{i_1\uparrow i_2\downarrow}_{j_1\uparrow j_2\downarrow}$ [23]

$$\begin{aligned} i\hbar\partial_t D^{i_1\uparrow i_2\downarrow}_{j_1\uparrow j_2\downarrow} &= \sum_{k_1,k_2} \left(H^{k_1 k_2}_{j_1 j_2} D^{i_1\uparrow i_2\downarrow}_{k_1\uparrow k_2\downarrow} - D^{k_1\uparrow k_2\downarrow}_{j_1\uparrow j_2\downarrow} H^{i_1 i_2}_{k_1 k_2} \right) \\ &+ U \left[D^{i_2\uparrow j_1\uparrow i_1\downarrow}_{j_2\uparrow j_1\uparrow j_1\downarrow} + D^{i_1\uparrow j_2\uparrow i_2\downarrow}_{j_1\uparrow j_2\uparrow j_2\downarrow} - \left(D^{j_2\uparrow i_1\uparrow j_1\downarrow}_{i_2\uparrow i_1\uparrow i_1\downarrow} + D^{j_1\uparrow i_2\uparrow j_2\downarrow}_{i_1\uparrow i_2\uparrow i_2\downarrow} \right)^* \right], \end{aligned} \tag{4.15}$$

which substantially enhances the numerical efficiency of the method.

5. Correlations in eigenstates of the Hubbard model

We apply measures for correlations introduced in Sec. 3.4 to eigenstates of the Hubbard model. For the graphical representation of the 1-RDM, $D_1(x_1; x_2)$, the pair-density, $D_{12}(x_1, x_2; x_1, x_2)$, and the diagonal of the two-particle cumulant, $\Delta_{12}(x_1, x_2; x_1, x_2)$, we use the Wannier functions calculated in Sec. 2.3 as basis functions.
Unless stated otherwise, we use the six site Hubbard model at half-filling with different interaction strengths U, for a sketch see Fig. 5.1. All results in this chapter with the exception of Sec. 5.5 are obtained via exact diagonalization, see App. B.

5.1. Energy spectrum of the six-site Hubbard model

Before we consider the influence of correlations on different eigenstates we investigate the energy spectrum of the Hubbard model at half-filling for different interaction strengths. We observe that for $U = 0.1\ J$ the spectrum consists of many small nearly degenerate plateaus while for $U = 1\ J$ the spectrum follows a nearly continuous line, see Fig. 5.2a. The overall shape is very similar for $U = 0.1\ J$ and $U = 1\ J$. For intermediate interaction strengths we observe the emergence of gaps in the energy spectrum and quasi-continuous parts in between, see Fig. 5.2b. The

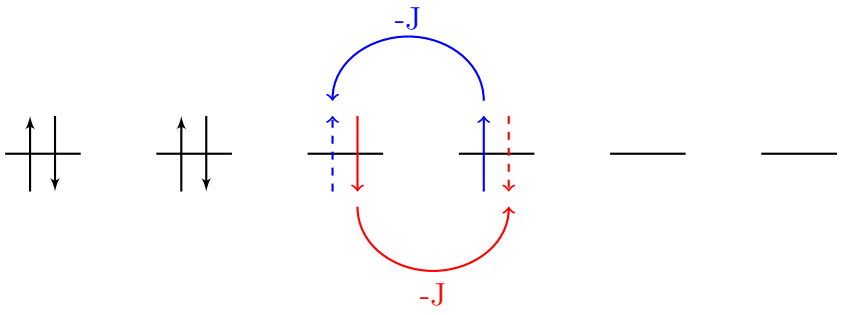

Figure 5.1.: Sketch of a six-site Hubbard model at half-filling with hopping amplitude J. The particles interact only if they occupy the same site with the interaction strength U.

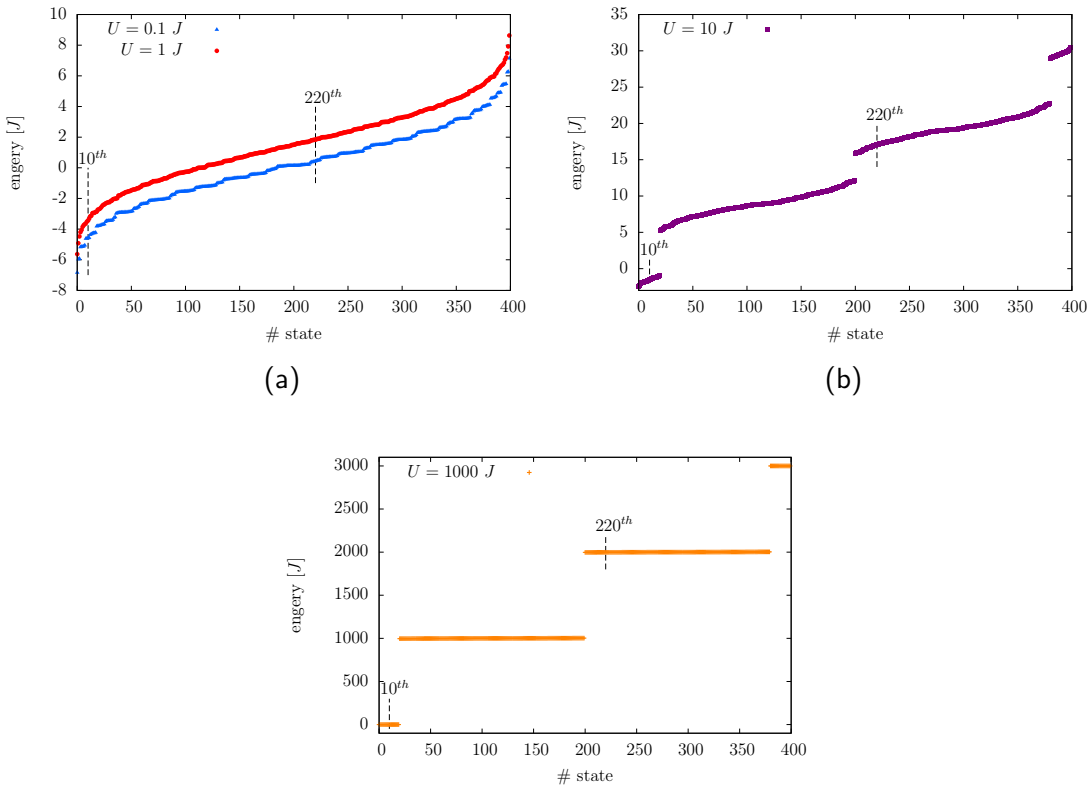

Figure 5.2.: Energy spectrum of a six-site Hubbard model at half-filling for (a) weak, (b) intermediate and (c) strong interactions obtained via exact diagonalization. The dashed lines indicate states further investigated in the following sections.

shape of the quasi continuous spectra between two gaps resembles the shape of the complete spectrum for weak interactions. For strongly interacting systems we observe $N/2+1$ equally spaced plateaus with gaps separating them, see Fig. 5.2c. The gaps are proportional to the interaction strength U and the energies on the plateaus are nearly degenerate. The shape and the height of the gaps can be explained with the number of doubly occupied sites. On the lowest plateau no site is doubly occupied and so the interaction energy is close to zero. On the second plateau one site is doubly occupied and has the interaction energy U. The third plateau has two doubly occupied sites and an interaction energy of 2 U and so on until $N/2$ of the sites are doubly occupied. The energy difference between the ground state and the maximally excited state increases linearly with U for strong interactions.
The Hubbard model is a finite model and thus has a finite basis set. Hence, the number of eigenstates is limited to the linear dimension of the Hamiltonian. For half-hilling the linear dimension is $\binom{N}{N/2}^2$. This yields a maximum of 400 eigenstates for the six-site Hubbard model at half-filling.
While the ground state $|\Psi_0\rangle$ is always a singlet state, i.e. $S_z|\Psi_0\rangle = 0$ and $S^2|\Psi_0\rangle = 0$, this is not true in general for excited states $|\Psi_i\rangle$. At half-filling, $S_z|\Psi_i\rangle = 0$ for all excited states but the possible eigenvalues of S^2 are $0, 2, ..., \frac{N}{2}\left(\frac{N}{2}-1\right)$. Since we only treat singlet states within the TD-2RDM method we focus in the remaining chapters on singlet states and all results shown are for singlet states.

5.2. Two-particle correlations in eigenstates of the Hubbard model

For a non-interacting system, $U = 0$, the N-body wave function factorizes completely and all cumulants vanish [42]. For non-vanishing U, the two-particle cumulant Δ_{12} plays a significant role. With increasing U double occupation of sites becomes increasingly energetically unfavorable. For the ground state double occupation of sites is thus increasingly suppressed, see the pair-density $D_{12}(x_1, x_2; x_1, x_2)$ in Fig. 5.3b, e, h. The structure of the pair-density can be traced back to a non-vanishing two-particle cumulant $\Delta_{12}(x_1, x_2; x_1, x_2)$ along the diagonal, see Fig. 5.3c, f, i. Already for the weakly interacting system, $U = 1\ J$, $\Delta_{12}(x_1, x_2; x_1, x_2)$ shows a complex structure enhancing the pair-density $D_{12}(x_1, x_2; x_1, x_2)$ on nearest neighboring sites while strongly surpressing the double occupation of sites. This effect was also observed in experiments [10]. For weakly correlated systems the 1-RDM $D_1(x_1; x_2)$ shows that the particles are delocalized on the whole lattice, see Fig. 5.3a. For the strongly correlated system the 1-RDM is strictly diagonal which means that the natural orbitals are the Wannier-orbitals occupied by exactly one particle, see Fig. 5.3g. It is striking to see that the 1-RDM predicts a mean occupation of one

particle per site independent of U. Although $D_1(x_1; x_2)$, $D_{12}(x_1, x_2; x_1, x_2)$, and Δ_{12} strongly vary with U, the density $D_1(x; x)$ is identical up to numerical precision for all U, see Fig. 5.4.

To study the influence of correlations on excited states we use a strongly interacting system with $U = 1000\ J$ where we expect the system to be highly correlated. We investigate three different states, the 10^{th} excited state which is in the same energy plateau as the ground state, the 220^{th} exited state located in the third plateau, and the maximally excited state. The 1-RDM, $D_1(x_1; x_2)$, for weakly and highly excited states does not show observable deviations from the ground state 1-RDM, compare Fig. 5.5a, c with Fig. 5.3g. Only for medium excited states it is more strongly smeared out which indicates that the natural occupation numbers $\lambda^{(1)}$ deviate from one, see Fig. 5.5b. This means that for weakly and highly excited states the particles are very localized and the natural orbitals correspond to the Wannier orbitals. For medium excitations the particles are partially delocalized. Comparing the pair-density $D_{12}(x_1, x_2; x_1, x_2)$ for the ground state, see Fig. 5.3h, and for excited states, see Fig. 5.6, we observe that the difference in $D_{12}(x_1, x_2; x_1, x_2)$ is small for weak excitations. For medium and very high excitations the structure of $D_{12}(x_1, x_2; x_1, x_2)$ changes since doubly occupied lattice sites start to appear which are not observed in the ground state due to the high energy associated with double occupation. The diagonal of the two-particle cumulant, $\Delta_{12}(x_1, x_2; x_1, x_2)$, for weakly excites states looks very similar to the ground state $\Delta_{12}(x_1, x_2; x_1, x_2)$, compare Fig. 5.7a and Fig. 5.3i. For higher excited states the structure of $\Delta_{12}(x_1, x_2; x_1, x_2)$ is different and $\Delta_{12}(x_1, x_2; x_1, x_2)$ can be positive and negative, see Fig. 5.7b, c. Especially for the maximally excited state $\Delta_{12}(x_1, x_2; x_1, x_2)$ enhances $D_{12}(x_1, x_2; x_1, x_2)$ on the diagonal and lowers it on the secondary diagonals, see Fig. 5.7c . Interestingly, we observe only very small deviations, i.e. of of the order 10^{-9}, in the density, $D_1(x; x)$, (not shown) for all excited states. The Hubbard model is thus a striking example where the density alone is practically insensitive to different interaction strengths U and excitation energies.

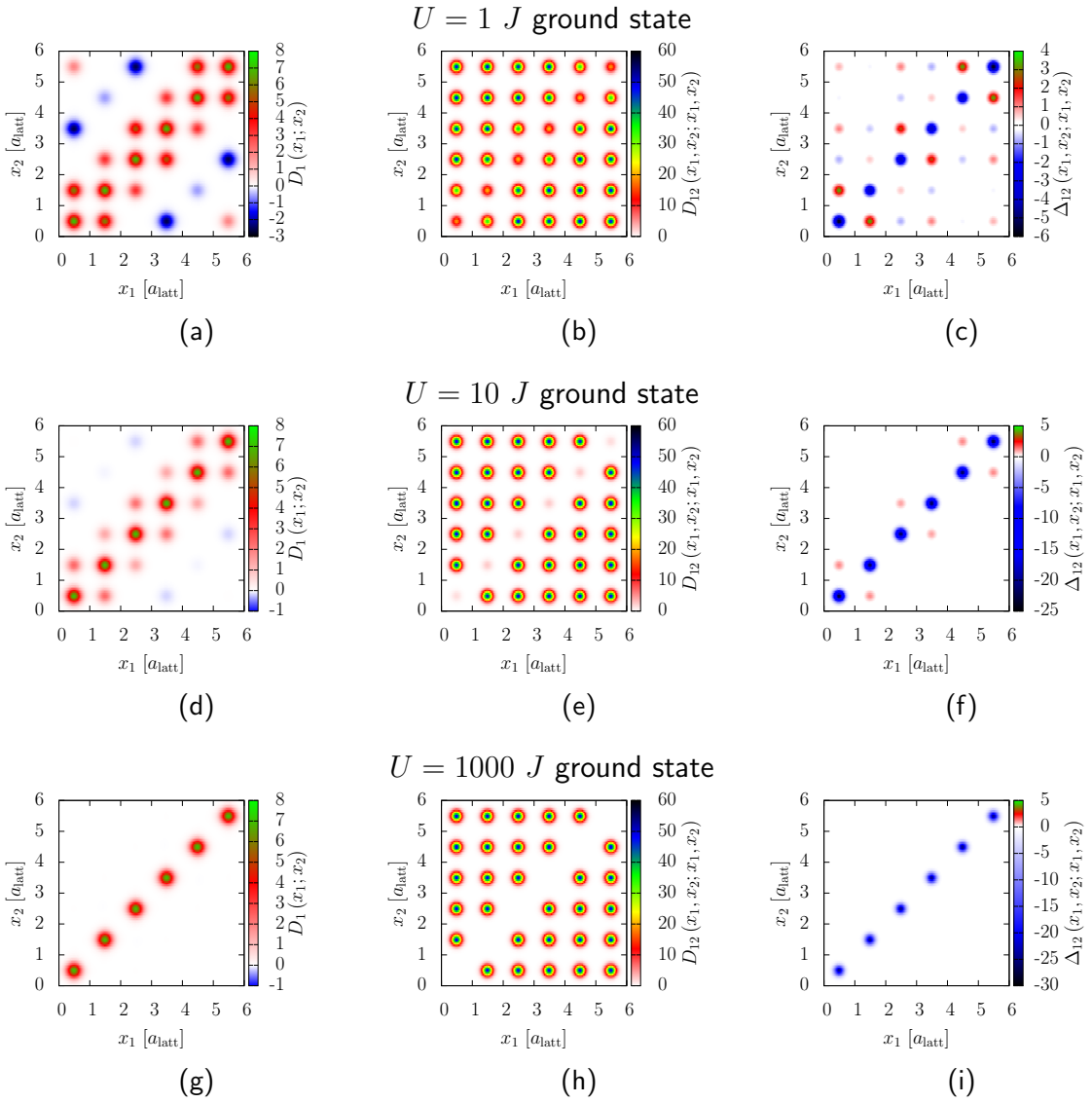

Figure 5.3.: Six-site Hubbard model at half-filling: 1-RDM $D_1(x_1;x_2)$, pair-density $D_{12}(x_1,x_2;x_1,x_2)$, and the diagonal of $\Delta_{12}(x_1,x_2;x_1,x_2)$ for the ground state with $U = 1\ J$ (a)-(c), $U = 10\ J$ (d)-(f) and $U = 1000\ J$ (g)-(i).

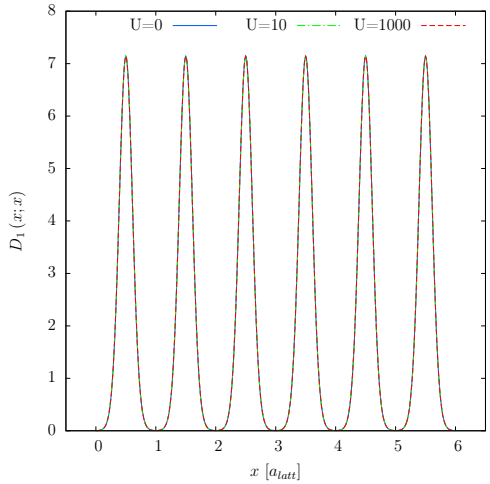

Figure 5.4.: Six-site Hubbard model at half-filling: The ground state density, $D_1(x;x)$, calculated for different interaction strengths U shows no difference up to numerical precision.

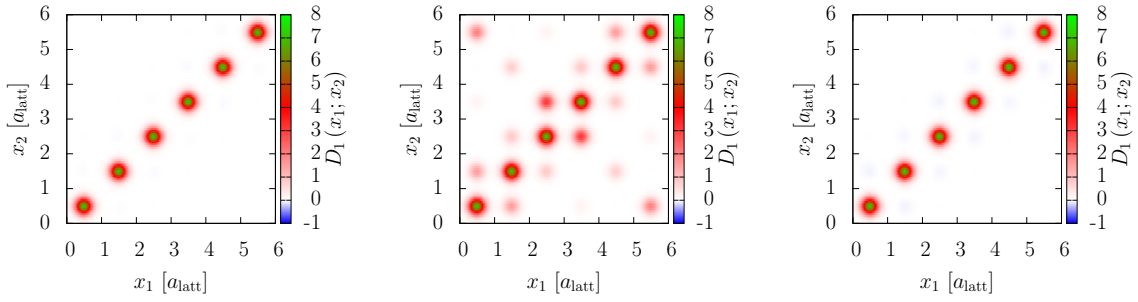

(a) (b) (c)

Figure 5.5.: Six-site Hubbard model at half-filling: 1-RDM, $D_1(x_1;x_2)$, obtained for $U = 1000\ J$ for the 10^{th} (a), the 220^{th} (b), and the highest eigenstate (c). In total there are 400 eigenstates in for the six-site Hubbard model at half-filling.

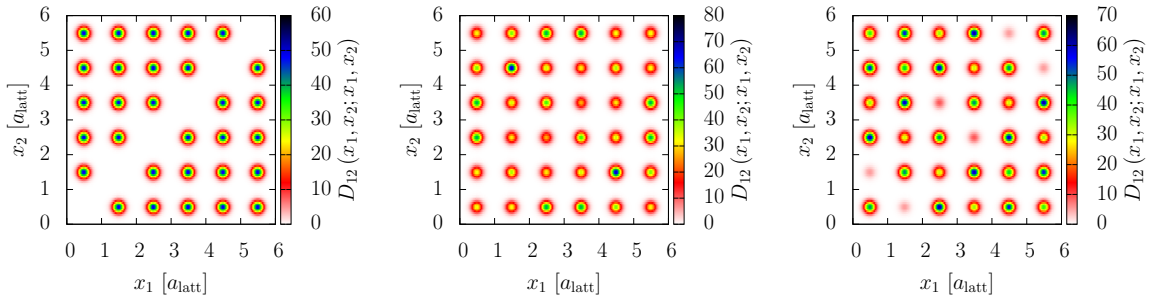

(a) (b) (c)

Figure 5.6.: Six-site Hubbard model at half-filling: Pair-density, $D_{12}(x_1,x_2;x_1,x_2)$, obtained for $U = 1000\ J$ for the 10^{th} (a), the 220^{th} (b), and the highest excited state (c).

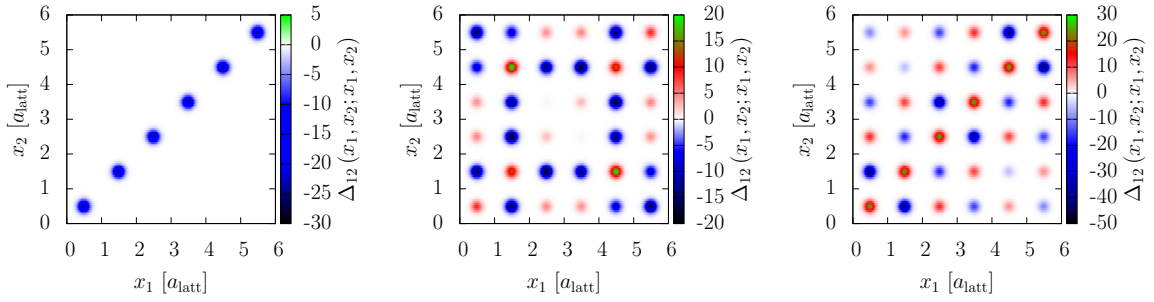

(a) (b) (c)

Figure 5.7.: Six-site Hubbard model at half-filling: The diagonal of $\Delta_{12}(x_1,x_2;x_1,x_2)$ calculated for $U = 1000\ J$ for the 10^{th} (a), the 220^{th} (b), and the highest excited state (c).

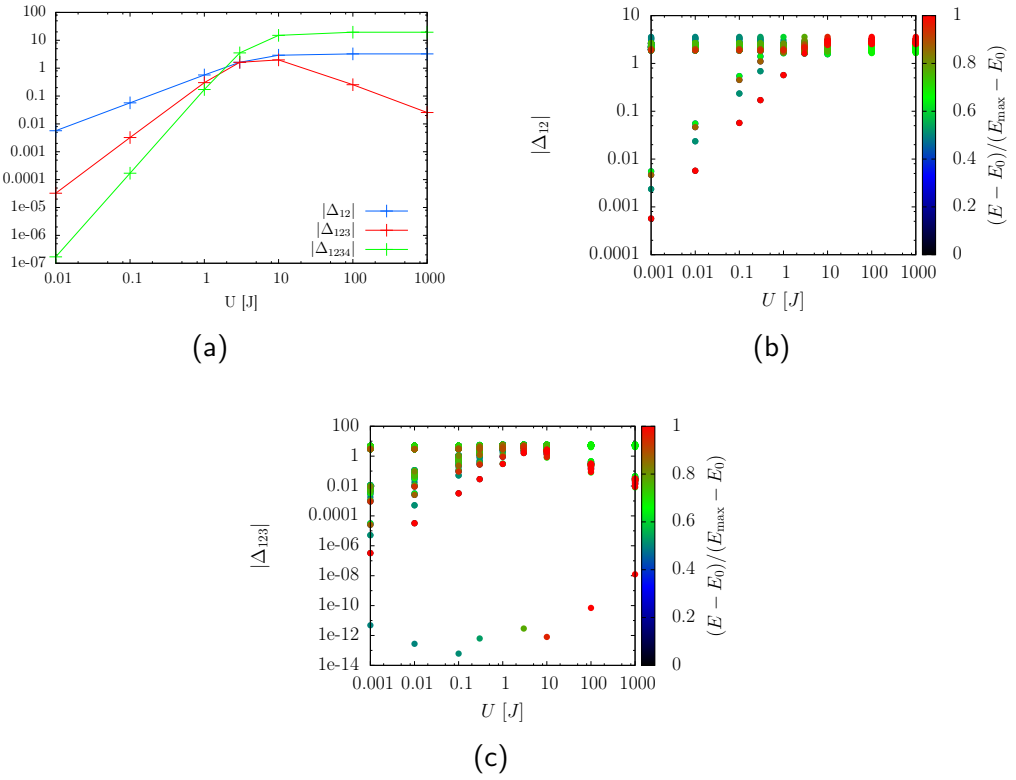

Figure 5.8.: Six-site Hubbard model at half-filling: (a) The magnitude of $\Delta_{1\ldots p}$, Eq. 3.25, as a function of U for the ground state. Magnitude of (b) Δ_{12}, and (c) Δ_{123} for various excited states. The color of the dots in (n) and (c) indicates the excitation energy $E - E_0$ of the state normalized to the maximal excitation energy $E_{\max} - E_0$, where $E_{\max}$ is the energy of the maximally excited state and E_0 is the ground state energy.

5.3. Quantification of correlations for eigenstates

To quantify correlations we calculate the two-particle Δ_{12}, three-particle Δ_{123}, and four-particle cumulant Δ_{1234} for the ground state and several excited states and compare the absolute magnitude, Eq. 3.25, with varying U. For the ground state at $U = 0$ all cumulants are exactly zero since the states are Hartree-Fock states. Increasing U, the magnitude of the cumulants increases according to a power law for $U \in [0 : 1]$ with

$$|\Delta_{12}| \propto U, \qquad |\Delta_{123}| \propto U^2, \qquad \text{and} \qquad |\Delta_{1234}| \propto U^3, \tag{5.1}$$

see Fig. 5.8a. This power law scaling in the limit of small interactions can be understood by looking at the graphical interpretation of the cumulants, Fig. 3.1, and

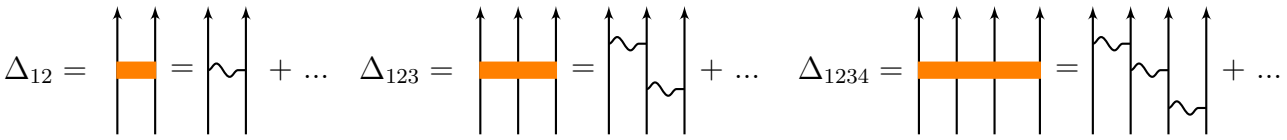

Figure 5.9.: Graphical representation of a perturbative approximation for cumulants. The orange rectangle represents the full vertex and the wiggly line symbolizes a single two-particle interaction with strength U.

remembering that the p-particle interaction vertex contains all possible p-particle interactions. The two particle-cumulant Δ_{12} describes all possible two-particle interactions where in the weak interacting limit the leading order connected diagram contains one interaction. The leading order connected three-particle term for small U is depicted in Fig. 5.9 and scales as U^2. In general, we thus expect a scaling of U^{p-1} for the magnitude of connected p-particle cumulants $|\Delta_{1..p}|$ in the weak interaction limit for the ground state. For stronger interactions we observe that $|\Delta_{12}|$ and $|\Delta_{1234}|$ saturate around $U \approx 10\ J$ while $|\Delta_{123}|$ decreases from there on. This means that for high interaction strengths three-particle correlations become less important than two and four-particle correlations.
In the following, we examine $|\Delta_{12}|$ and $|\Delta_{123}|$ for all singlet excited states and several interaction strengths, see Fig. 5.8b and c. The color of the dots indicates the excitation energy of the corresponding eigenstate $E - E_0$ normalized to the maximal excitation energy $E_{\text{max}} - E_0$, where E_0 is the ground state energy, and E_{max} is the energy of the maximally excited state. We observe that the strength of correlations is similar for a large number of states independent of their energy for large U. We observe that $|\Delta_{12}|$ is large for many excited states already for weak interaction strengths. Among these states we observe that two-particle correlations slightly increase with U. For a few states the dependence of $|\Delta_{12}|$ on U is similar as for the ground state. For high interaction strengths all states show strong two-particle correlations.
$|\Delta_{123}|$ shows a qualitatively similar dependence on U as the ground state for many excited states where we observe an increase for $U < 1\ J$ and a slower decrease for $U > 10\ J$, see Fig. 5.8c. As for $|\Delta_{12}|$ we observe a fraction of eigenstates where $|\Delta_{123}|$ is not strongly dependent on U. Interestingly, we find states that have a vanishing three-particle cumulant. Investigating these states more closely we observe that these states correspond to anti-symmetrized geminal product (AGP) states [61]. Such states are characterized by one geminal being maximally occupied and all others equally occupied as described in Sec. 3.4, see Fig. 5.10a. This means that the natural entropy for the 2-RDM obeys $S_2 = S_2^*$. Further, the 1-RDM becomes diagonal and all natural occupation numbers are equal [61], i.e. for half-filling $\lambda^{(1)} = \frac{1}{2}$. The 1-RDM entropy is thus maximal $S_1 = S_1^{\text{max}}$. These states

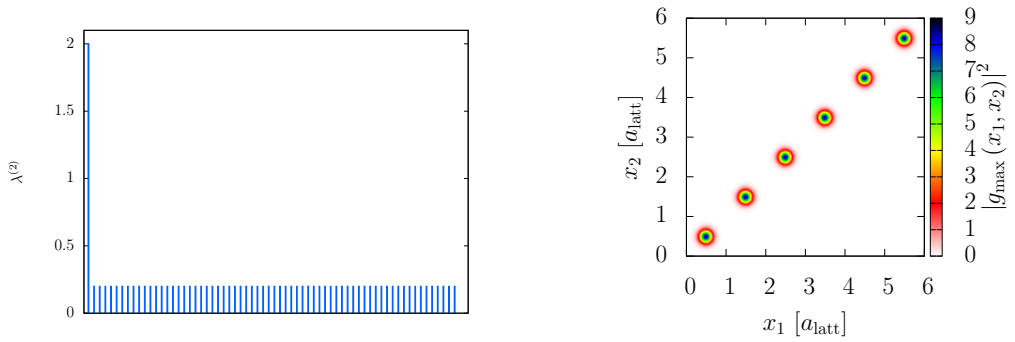

(a) (b)

Figure 5.10.: Six-site Hubbard model at halffilling: (a) Geminal occupation numbers $\lambda^{(2)}$ of the 215^{th} excited state with interaction strength $U = 0.1\ J$. $|\Delta_{123}| = 0$ for this state. (b) Absolute magnitude of the highest occupied geminal $g_{\max}(x_1, x_2)$ shown in (a).

reach maximum values for $|\Delta_{12}|$. We observe, to our knowledge for the first time, that $|\Delta_{123}|$ is vanishing for these states. Other empirical observations are that these states have vanishing kinetic energy and that the maximally occupied geminal $g_{\max}(x_1, x_2)$ is diagonal in x_1 and x_2. As an example the maximally occupied geminal for $U = 0.1\ J$ is depicted in Fig. 5.10b. With knowledge of $g_{\max}$ we can show that an AGP state does, indeed, show off-diagonal long-range order as mentioned in Sec. 3.4 and described in [59, 61]. This off-diagonal long-range order can be seen in the 2-RDM, i.e. in D^{ii}_{jj}. Decomposing the 2-RDM into geminals for an AGP state we get

$$D^{i_1 i_2}_{j_1 j_2} = \lambda_{\max} [g_{\max}]_{j_1 j_2} [g^*_{\max}]^{i_1 i_2} + \bar{D}^{i_1 i_2}_{j_1 j_2}, \tag{5.2}$$

where $\bar{D}^{i_1 i_2}_{j_1 j_2}$ is the part of the 2-RDM formed from all geminals that are equally occupied. Looking at the part of the 2-RDM that is responsible for off-diagonal long-range order, i.e. D^{ii}_{jj}, formed from $g_{\max}$ we find

$$[D_{\max}]^{ii}_{jj} = \lambda_{\max} [g_{\max}]_{jj} [g^*_{\max}]^{ii} = \lambda_{\max} \frac{1}{\sqrt{N}} (-1)^{j+1} \frac{1}{\sqrt{N}} (-1)^{i+1} = \frac{M - N + 2}{2M} (-1)^{i+j}. \tag{5.3}$$

This non-vanishing contribution for all values of i and j stems from the diagonal and up to a sign constant structure of $g_{\max}$.

It is instructive to investigate the spatial distribution of correlations. We define a two-particle correlation function

$$C_{\mathrm{particle}}(r) = \sum_i \frac{\Delta^{i\ i+r}_{i\ i+r}}{n}, \tag{5.4}$$

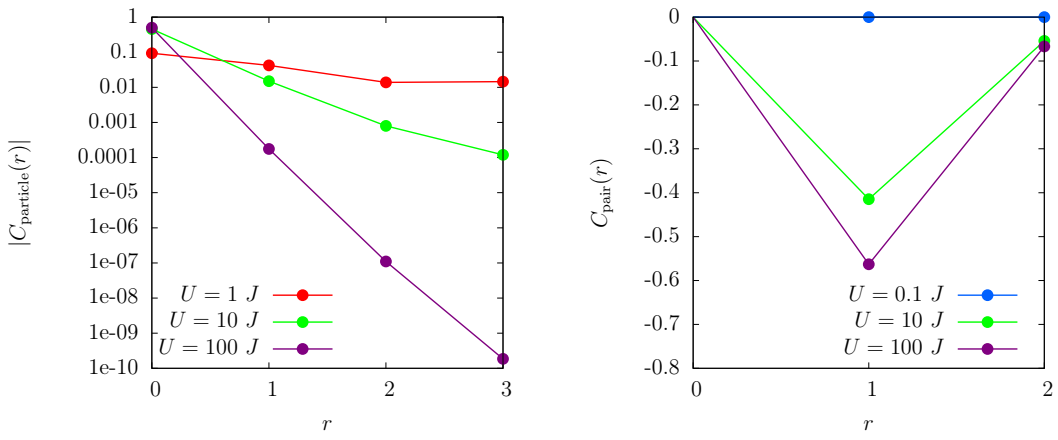

Figure 5.11.: Six-site Hubbard model at half-filling: (a) Magnitude of the two-particle correlation function $C_{\text{particle}}(r)$, Eq. 5.4, as a function of the particle distance r for the ground state of a six-site Hubbard model for different interaction strengths. (b) Pair-pair correlation function $C_{\text{pair}}(r)$, Eq. 5.5, as function of the particle distance r for the ground state for different interaction strengths.

where i is a spatial index, r is the distance between two sites, and n is the number of terms contributing to the sum, e.g. for a six-site Hubbard model $n = 6$ for $r = 0$, $n = 5$ for $r = 1$, and so on. We choose this normalization due to the small system sizes we investigate and note that this overestimates the impact of boundary terms which is the reason why we only show results for $r < N_{\text{sites}}/2$. The two-particle correlation function $C_{\text{particle}}(r)$ measures the correlations of two particles over distance r. $C_{\text{particle}}(r)$ shows that the largest contribution to two-particle correlations for weakly excited states of strongly interacting systems is on-site correlation, i.e. $C_{\text{particle}}(r)$ is maximal for $r = 0$, see Fig. 5.11a. We observe that for strongly interacting systems C_{particle} decays exponentially for the ground state, see Fig. 5.11a. In Fig. 5.11a we show the absolute magnitude of $C_{\text{particle}}(r)$, because the sign is different for different values of r. We do not observe an exponential decay of $|C_{\text{particle}}|$ for weakly interacting systems. Similar to $C_{\text{particle}}(r)$ we define a pair-pair correlation function

$$C_{\text{pair}}(r) = \sum_i \frac{\Delta_{i\ i\ i+r\ i+r}^{i\ i\ i+r\ i+r}}{n}, \tag{5.5}$$

where i is a spatial index, r is the distance between two sites and n is the number of terms contributing to the sum. $C_{\text{pair}}(r)$ measures the correlation between two doubly occupied sites, so called doublons, with distance r. $C_{\text{pair}}(r)$ is zero for $r = 0$

because it is impossible to doubly occupy the same site twice, see Fig. 5.11b. Interestingly, we see strong correlations for strongly interacting systems for neighboring sites which shows that the two doubly occupied sites are correlated although they interaction is only local on site [62]. $C_{\text{pair}}(r)$ increases rapidly with interaction strength for $r = 1$. For weak interactions we do not observe such correlations. The negative sign stems from the suppression of doubly occupied sites for large U, see Fig. 5.3f.
We compare the correlation measures based on entropies, see Sec. 3.4, with the two-particle correlation strength defined as $|\Delta_{12}|$ to test whether they show the same results and can thus be used as correlation measures in experiments. The 1-RDM natural entropy S_1, see Eq. 3.26a, shows a large increase up to $U = 10\ J$ for many excited states, see Fig. 5.12a. A small fraction of states reaches the maximal entropy for six sites

$$S_1^{\max} = 3 \ln (2) \,, \tag{5.6}$$

for high interaction strengths, see Eq. 3.29. This means that all natural orbitals are occupied uniformly. Investigating the natural entropy for the 2-RDM, S_2, we observe a broad spectrum of possible values for S_2 for $U \leq 1\ J$, see Fig. 5.12b. For higher interaction strengths the spectrum becomes narrower. This means that for low interaction strengths we can find states that are close to Hartree-Fock states while for larger interaction strengths the geminal occupation numbers $\lambda_2^{(2)}$ are broader distributed. Comparing the energy of the states with the highest S_1 and S_2 we observe that for large U the high energy states reach the maximum value of S_1, but not of S_2 which is given by

$$S_2^{\max} = 15 \ln \left(\frac{22}{5} \right) , \tag{5.7}$$

for the six-site Hubbard model at half-filling, see Eq. 3.31. Comparing S_1 and S_2 with $|\Delta_{12}|$ we observe that both entropy measures show qualitatively a similar behavior as $|\Delta_{12}|$, see Fig. 5.8b and Fig. 5.12a, b. Hence, we expect the natural entropies S_1 and S_2 to provide a qualitative measure of the two-particle correlation strength $|\Delta_{12}|$.
Concluding this section, we investigate the frequently measured [10, 30] doublon fraction

$$D = \frac{\langle \hat{n}_{i\uparrow} \hat{n}_{i\downarrow} \rangle}{\langle \hat{n}_{i\uparrow} \rangle \cdot \langle \hat{n}_{i\downarrow} \rangle} , \tag{5.8}$$

which counts the fraction of doubly occupied lattice sites. $\hat{n}_{i\uparrow}$ ($\hat{n}_{i\downarrow}$) is the occupation number operator on site i of spin $\uparrow$ ($\downarrow$). $< \cdots >$ denotes the sum over all sites i. We compare its behavior with $|\Delta_{12}|$. In the literature D is used as indicator for transport coefficients since it becomes zero for a chain of localized atoms [10, 56].

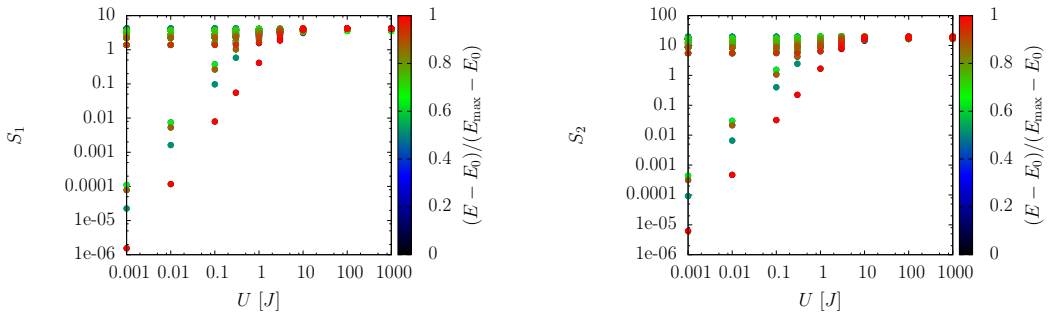

(a) (b)

Figure 5.12.: Six-site Hubbard model at half-filling: Natural entropy for (a) the 1 -RDM S_1, Eq. 3.26a, and (b) the 2-RDM S_2, Eq. 3.26b, for the ground state. The color of the dots in (c) indicates the excitation energy $E - E_0$ of the state normalized to the maximal excitation energy $E_{\max} - E_0$, where $E_{\max}$ is the energy of the maximally excited state and E_0 is the ground state energy.

D is closely related to D_1 and Δ_{12} via

$$D = \frac{\langle \hat{n}_{i\uparrow} \hat{n}_{i\downarrow} \rangle}{\langle \hat{n}_{i\uparrow} \rangle \cdot \langle \hat{n}_{i\downarrow} \rangle} = \frac{\mathrm{Tr}\left(D_{1\uparrow} \cdot D_{1\downarrow}\right) + \mathrm{Tr}\left(\Delta_{1\uparrow 2\downarrow}\right)}{\left(\mathrm{Tr}\left(D_{1\uparrow}\right)\right)^2}. \tag{5.9}$$

For the six-site Hubbard model at half-filling we observe that for low energy states the doublon fraction goes to zero for $U \to \infty$, see Fig. 5.13. While for weak interactions the doublon fraction D varies over a large interval for large U D takes on discrete values. The reason is the plateau structure of the energy spectrum for large U, see Fig. 5.2c . D is zero for the low energy states, $\frac{1}{N}$ for the states on the next energy plateau, and so on. In theoretical calculations it was shown that the continuous Hubbard model in one dimension has a Mott transition for $U = 0$ and is thus an insulator for all $U > 0$ [63]. Nevertheless, we observe a a significant and abrupt change in the properties of the system in the range between $U = 3\ J$ and $U = 10\ J$ especially for the ground state where the two-particle and four-particle cumulants saturate and the 1-RDM becomes diagonal, see Fig. 5.8a and Fig. 5.3a, d, g. This Mott-transition like feature might be traced back to the finite size of the system.

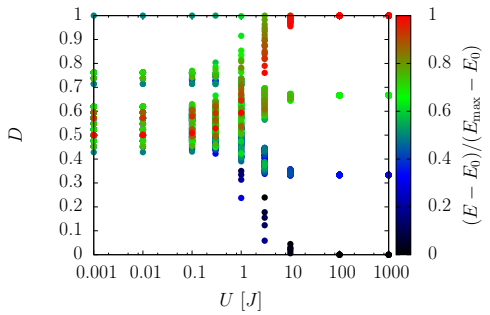

Figure 5.13.: Six-site Hubbard model at half-filling: Doublon fraction D, Eq. 5.8, for the ground state and different excited states. The color of the dots indicates the excitation energy $E - E_0$ of the state normalized to the maximal excitation energy $E_{\max} - E_0$, where $E_{\max}$ is the energy of the maximally excited state and E_0 is the ground state energy.

5.4. Quality of the 3-RDM reconstruction

In this section we quantify the accuracy of the 3-RDM reconstructions described in Sec. 3.2. We focus on the $(\uparrow,\uparrow,\downarrow)$-block of the 3-RDM because we only need this block in the propagation, see Eq. 4.15. We calculate the difference between the $(\uparrow,\uparrow,\downarrow)$-block of the exact and the reconstructed 3-RDM

$$\begin{aligned}\epsilon^2_{D_{\uparrow\uparrow\downarrow}} &= \mathrm{Tr}\left\{\left([D_{123}]_{\uparrow\uparrow\downarrow} - [D^{rec}_{123}]_{\uparrow\uparrow\downarrow}\right)^2\right\} \\ &= \sum_{i_1,i_2,i_3,k_1,k_2,k_3} \left\{\left(D^{i_1\uparrow i_2\uparrow i_3\uparrow}_{k_1\uparrow k_2\uparrow k_3\downarrow} - [D^{rec}]^{i_1\uparrow i_2\uparrow i_3\uparrow}_{k_1\uparrow k_2\uparrow k_3\downarrow}\right)\left(D^{k_1\uparrow k_2\uparrow k_3\uparrow}_{i_1\uparrow i_2\uparrow i_3\downarrow} - [D^{rec}]^{k_1\uparrow k_2\uparrow k_3\uparrow}_{i_1\uparrow i_2\uparrow i_3\downarrow}\right)\right\}.\end{aligned} \tag{5.10}$$

Due to the on-site interaction only a fraction of elements of the 3-RDM enters the collision operator in Eq. 4.5. The magnitude of the $(\uparrow,\downarrow)$-block of the collision operator is

$$|C_{\uparrow\downarrow}|^2 = \sum_{j_1 j_2 i_1 i_2} \left|C^{i_1\uparrow i_2\downarrow}_{j_1\uparrow j_2\downarrow}\right|^2, \tag{5.11}$$

and the error in the collision operator is

$$\begin{aligned}\epsilon^2_{C_{\uparrow\downarrow}} &= \mathrm{Tr}\left\{\left([C]_{\uparrow\downarrow} - [C^{rec}]_{\uparrow\downarrow}\right)^2\right\} \\ &= \sum_{i_1,i_2,k_1,k_2} \left\{\left(C^{i_1\uparrow i_2\uparrow}_{k_1\uparrow k_2\downarrow} - [C^{rec}]^{i_1\uparrow i_2\uparrow}_{k_1\uparrow k_2\downarrow}\right)\cdot\left(C^{k_1\uparrow k_2\uparrow}_{i_1\uparrow i_2\downarrow} - [C^{rec}]^{k_1\uparrow k_2\uparrow}_{i_1\uparrow i_2\downarrow}\right)\right\}.\end{aligned} \tag{5.12}$$

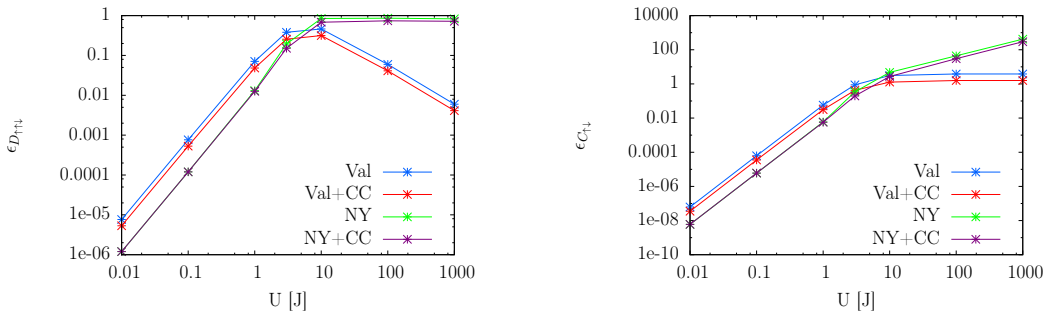

Figure 5.14.: Six-site Hubbard model at half-filling: Error in the reconstruction of (a) the $(\uparrow,\uparrow,\downarrow)$-block of the 3-RDM $\epsilon_{D_{\uparrow\uparrow\downarrow}}$, Eq. 5.10, and (b) the $(\uparrow,\downarrow)$-block of the collision operator $\epsilon_{C_{\uparrow\downarrow}}$, Eq. 5.12, for different reconstructions for the ground state.

Comparing the Valdemoro and the NY reconstruction of the 3-RDM for the ground state of the six-site Hubbard model at half-filling we see that for low interaction strengths the NY approximation gives more accurate results. We expect the reason for this to be that one term of the three-particle cumulant Δ_{123} is included in the reconstruction, see Fig. 5.14a and Fig. 3.2 for the the NY approximation of $\epsilon_{C_{\uparrow\downarrow}}$. However, for stronger interactions strengths the NY reconstruction overestimates the impact of this collision process and leads to a saturation of $\epsilon_{D_{\uparrow\uparrow\downarrow}}$. The contraction consistent correction of the reconstructions consistently reduces the error in both cases. The error in the collision operator $\epsilon_{C_{\uparrow\downarrow}}$ for the Valdemoro reconstruction saturates for strong interactions, see Eq. 4.5. The error of the 3-RDM $\epsilon_{D_{\uparrow\uparrow\downarrow}}$ scales as $1/U$ in the relevant region, see Fig. 5.14a and Fig. 5.14b. For the NY reconstruction $\epsilon_{C_{\uparrow\downarrow}}$ grows with U because $\epsilon_{D_{\uparrow\uparrow\downarrow}}$ saturates.
The behavior of $\epsilon_{C_{\uparrow\downarrow}}$ and $\epsilon_{D_{\uparrow\uparrow\downarrow}}$ observed for the ground state is found for a small fraction of excited states while most states show a considerable error in the 3-RDM already for weak interactions, see Fig. 5.15a, b, c and d. Note that we do not show the results for the states with vanishing Δ_{123} in Fig. 5.15c - f to make comparison between the two reconstructions easier. Comparing the contraction consistent NY reconstruction with the contraction consistent Valdemoro reconstruction we observe that both yield similar results for $U < 10\ J$ while the later is more accurate for $U > 10\ J$, see Fig. 5.15a and Fig. 5.15b. For the contraction consistent Valdemoro reconstruction $\epsilon_{D_{\uparrow\uparrow\downarrow}}$ decreases for most of the excited states with increasing U while the contraction consistent NY reconstruction yields a constantly large $\epsilon_{D_{\uparrow\uparrow\downarrow}}$ for all excited states. The contraction consistent Valdemoro approximation gives exact results for AGP states since $\Delta_{123} = 0$.
$\epsilon_{C_{\uparrow\downarrow}}$ scales linearly with U, see Eq. 4.5. This means that $\epsilon_{C_{\uparrow\downarrow}}$ is suppressed for small interactions, i.e. $U < 1\ J$, but enhanced for stronger interactions, see Fig. 5.15c

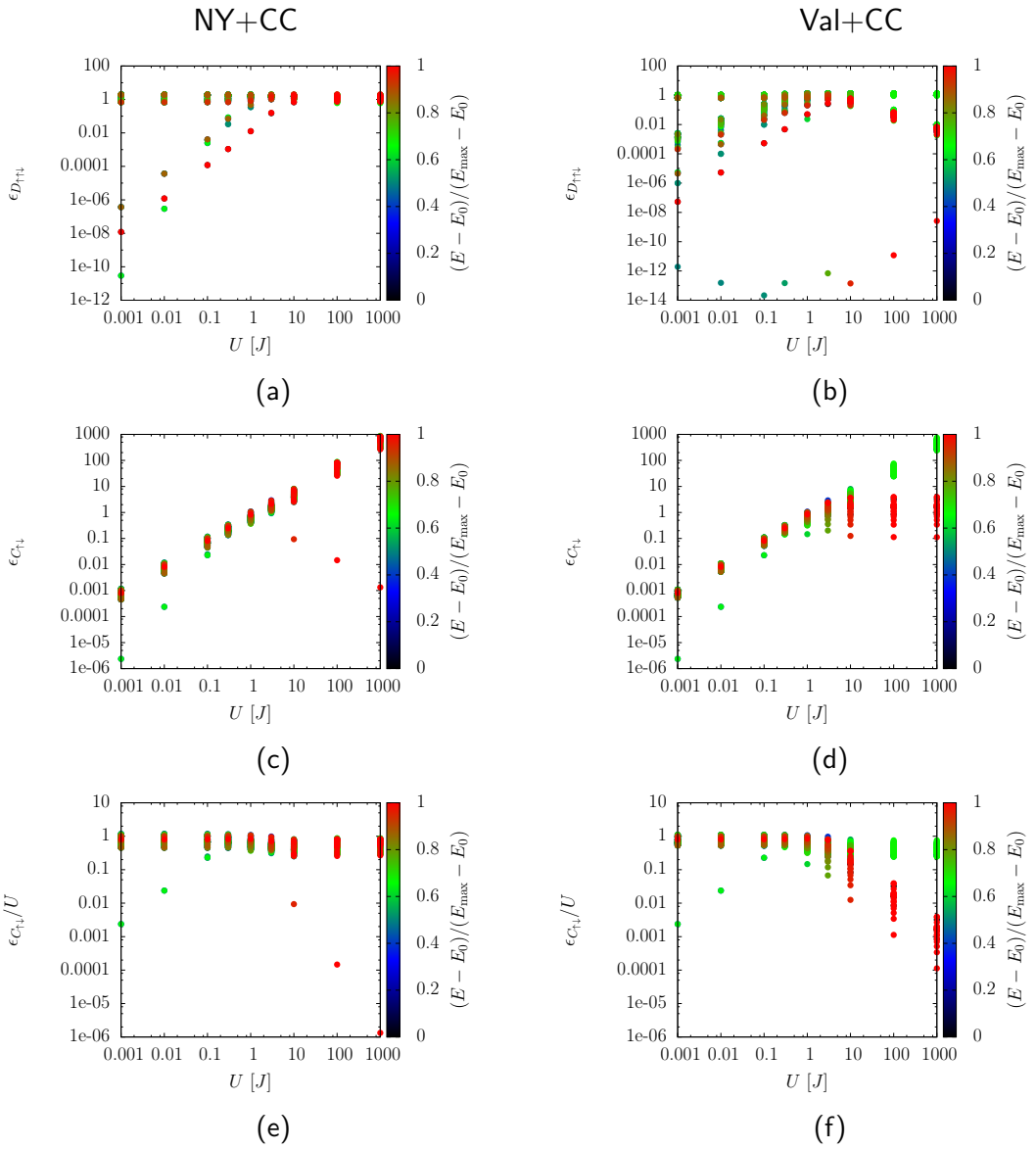

Figure 5.15.: Six-site Hubbard model at half-filling: Error in the reconstruction of the $(\uparrow,\uparrow,\downarrow)$-block of the 3-RDM $\epsilon_{D_{\uparrow\uparrow\downarrow}}$, Eq. 5.10, using (a) the contraction consistent NY, and (b) the contraction consistent Valdemoro reconstruction for the ground state and several excited states. Error in the $(\uparrow,\downarrow)$-block of the collision operator $\epsilon_{C_{\uparrow\downarrow}}$, Eq. 5.12, using (c) the contraction consistent NY, and (d) the contraction consistent Valdemoro reconstruction for the ground state and several excited states. $\epsilon_{C_{\uparrow\downarrow}}/U$, Eq. 5.12, using (e) the contraction consistent NY, and (f) the contraction consistent Valdemoro reconstruction for the ground state and several excited states. The color of the dots in (c) indicates the excitation energy $E-E_0$ of the state normalized to the maximal excitation energy $E_{\max}-E_0$, where $E_{\max}$ is the energy of the maximally excited state and E_0 is the ground state energy.

and Fig. 5.15d. For $U \leq 1\ J$ the contraction consistent NY reconstruction is more accurate but for $U > 1\ J$ almost all states show a large $\epsilon_{C_{\uparrow\downarrow}}$. In this regime $\epsilon_{C_{\uparrow\downarrow}}$ saturates for a large fraction of excited states using the contraction consistent Valdemoro approximation. Dividing $\epsilon_{C_{\uparrow\downarrow}}$ with U we obtain the magnitude of the part of the three-particle cumulant Δ_{123} entering the equations of motion, see Eq. 4.5. We observe that $\frac{\epsilon_{C_{\uparrow\downarrow}}}{U}$ shows a similar behavior as $\epsilon_{D_{\uparrow\uparrow\downarrow}}$ for large interaction strengths, see Fig. 5.15a, b and Fig. 5.15e, f. For small interaction strengths $\frac{\epsilon_{C_{\uparrow\downarrow}}}{U}$ we do not observe a strong dependence on U but a constantly large value for both reconstructions.
Concluding, we see that the contraction consistent NY reconstruction provides good results for weakly interacting systems. Thus, we expect the TD-2RDM method to work well within this limit.

5.5. Excitation spectra

The excitation spectrum of the Hubbard model can be determined within the TD-2RDM method using linear response theory [3]. We start with the ground state obtained via exact diagonalization and apply in analogy with [26] a weak external potential to the first lattice site for short time. The Hubbard Hamiltonian is in this case given by

$$H_{\text{Hub}} = -J \sum_{\substack{\langle i,j \rangle \\ \sigma\epsilon(\downarrow,\uparrow)}} \hat{a}^\dagger_{i,\sigma}\hat{a}_{j,\sigma} + U \sum_i \hat{n}_{i,\uparrow}\hat{n}_{i,\downarrow} + f_0\delta(t)\left(\hat{n}_{1,\uparrow} + \hat{n}_{1,\downarrow}\right), \tag{5.13}$$

where f_0 is the strength of the external potential, and $\hat{n}_{1,\uparrow}$ ($\hat{n}_{1,\downarrow}$) is the occupation number operator on site one for spin $\uparrow$ ($\downarrow$). This δ-kick in principle excites all possible transitions. In practice, the available energy is limited by the time step of the propagation Δt. The kick leads to density fluctuations of the whole system which can be used to determine the energy spectrum via linear response theory [3]. We use the ground state of an eight-site Hubbard model at half-filling with $U = 0.1\ J$, $f_0 = 0.01\ J$, a time step of $\Delta t = 0.02\ J^{-1}$ and a maximum propagation time of $T = 1000\ J^{-1}$. The 2-RDM is propagated without purification using the contraction consistent NY reconstruction. The obtained density fluctuations on site one

$$n_1(t) = \langle\Psi(t)|\,\hat{n}_{1,\uparrow} + \hat{n}_{1,\downarrow}\,|\Psi(t)\rangle = \langle\Psi(t)|\,\hat{n}_1\,|\Psi(t)\rangle\,, \tag{5.14}$$

are in excellent agreement with the exact calculation, see Fig. 5.16a. The absolute magnitude of the Fourier transform of the density-fluctuation $|\mathcal{F}\left[n_1(t)\right]|^2$ is peaked at the excitation energies of the system [3, 26]. Since the density fluctuations can be reproduced very well within the TD-2RDM method the excitation spectrum can be reproduced almost perfectly, see Fig. 5.16b. Comparing the obtained excitation

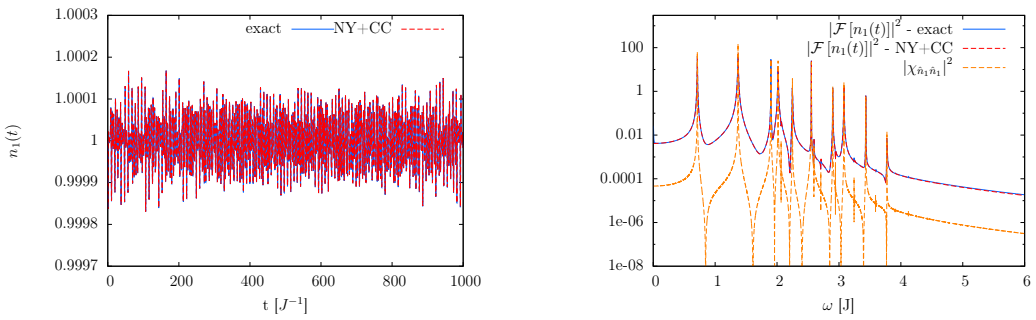

(a) (b)

Figure 5.16.: Eight-site Hubbard model at half-filling with interaction strength $U = 0.1\ J$: (a) Density fluctuations on the first site $n_1(t)$ after a quasi-δ-kick of the ground state with strength $f_0 = 0.01\ J$ calculated within the TD-2RDM method using the contraction consistent NY reconstruction and compared to the exact calculation. (b) Excitation spectrum obtained from the exact calculation (blue), compared to the result obtained within the TD-2RDM method using the contraction consistent NY reconstruction (red dashed), and the Lehmann representation (orange dashed) of linear response theory, Eq. 5.15. The time step Δt was $0.02\ J^{-1}$.

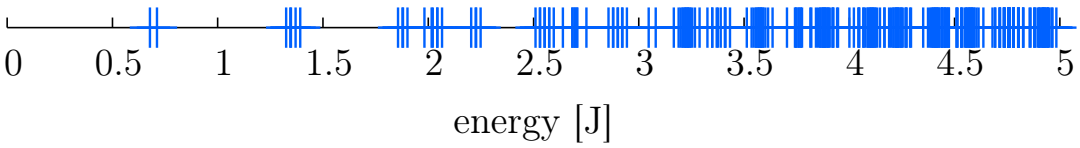

(a)

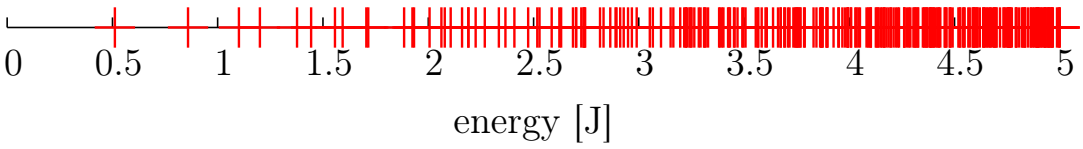

(b)

Figure 5.17.: The exact low-energy excitation spectrum of the eight-site Hubbard model at half-filling for (a) $U = 0.1\ J$ and (b) $U = 1\ J$.

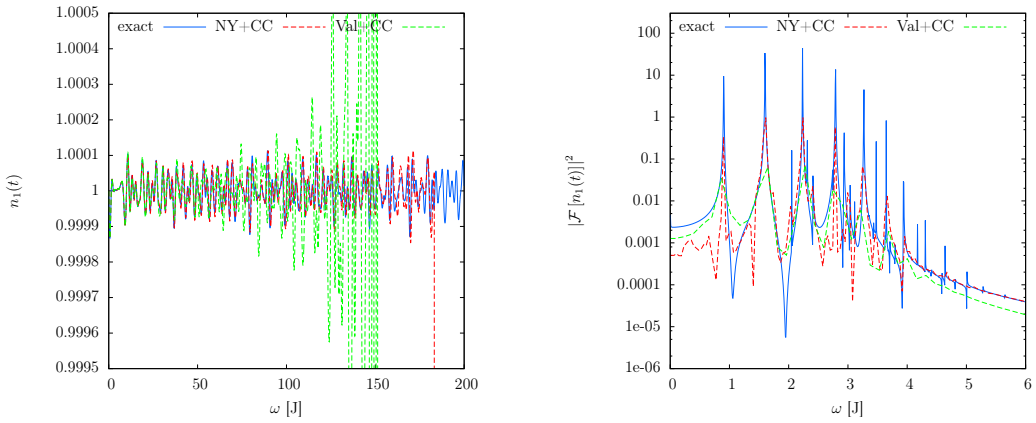

(a) (b)

Figure 5.18.: Eight-site Hubbard model at half-filling with interaction strength $U = 1\ J$: (a) Density fluctuations on the first site $n_1(t)$ of the ground state after a quasi δ-kick with strength $f_0 = 0.01\ J$ calculated within the TD-2RDM method compared to the exact calculation. (b) Energy spectrum obtained from the TD-2RDM method compared to the exact calculation.The time step Δt was $0.02\ J^{-1}$.

spectrum with the exact spectrum we observe that only low lying excitations can be resolved, see Fig. 5.17a. This is because the difference between two neighboring excitation energies is often too small. We compare the excitation spectrum with a linear response curve calculated using the density-density response function $\chi_{\hat{n}_1\hat{n}_1}$ obtained from Lehmann representation [3]

$$\chi_{\hat{n}_1\hat{n}_1}(\omega) = \lim_{\eta\to 0^+} \sum_{n=1}^{\infty} \left\{ \frac{\langle\Psi_0|\,\hat{n}_1\,|\Psi_n\rangle\,\langle\Psi_n|\,\hat{n}_1\,|\Psi_0\rangle}{\omega - \Omega_n + i\eta} - \frac{\langle\Psi_0|\,\hat{n}_1\,|\Psi_n\rangle\,\langle\Psi_n|\,\hat{n}_1\,|\Psi_0\rangle}{\omega + \Omega_n + i\eta} \right\}, \tag{5.15}$$

where $|\Psi_0\rangle$ is the initial wave function and $|\Psi_n\rangle$ are the eigenfunctions with the corresponding eigenenergies Ω_n of the underlying Hamiltonian. The eigenfunctions $|\Psi_0\rangle$ and eigenenergies Ω_n are obtained via exact diagonalization. The curve shows good agreement apart from the peak shape which is strongly dependent on the smearing parameter η needed to evaluate Eq. 5.15.

Performing the same analysis with the same parameters for the higher interaction strength $U = 1\ J$ we observe that the TD-2RDM method shows some deviations from the exact calculation and shows instabilities for $t > 120\ J^{-1}$ for the contraction consistent Valdemoro reconstruction and for $t > 180\ J^{-1}$ for the contraction consistent NY reconstruction, see Fig. 5.18a. This limits the accessible energy resolution which is given by $\Delta\omega = \frac{2\pi}{T}$. With this resolution we can only resolve the

main peaks for both reconstructions. The contraction consistent NY reconstruction grasps the first few energy peaks correctly, while the contraction consistent Valdemoro reconstruction shows a very blurred picture, compare Fig. 5.18b and Fig.5.17b. Concluding we showed that we can reproduce the low frequency energy spectrum of a weakly interacting systems with the TD-2RDM method with higher accuracy than previous results [26].

6. Build-up of correlations in non-equilibrium states

Previously, time-dependent density matrix methods and related Green's function based methods [24–26] have been applied to highly excited but initially uncorrelated states of the Hubbard model at half-filling to benchmark the methods. These states are interesting per se because one can study the build-up of correlations as a function of time. Moreover, such states can be studied experimentally by a quench in interactions and in the optical lattice. We investigate the dynamics of highly excited but initially uncorrelated states within the exact numerical solution. The results presented here are for the six-site Hubbard model at half-filling unless explicitly stated. We use the initial condition that all particles are confined to the left half of the Hubbard chain.

6.1. Density fluctuations

The initial condition of half of the sites being doubly occupied is far from equilibrium and leads to strong density fluctuations on all sites, see Fig. 6.1a for site one. On a qualitative level we observe for weakly interacting systems that the occupation number on site one $n_1(t)$ strongly fluctuates while for strong interactions the initial configuration is almost frozen and $n_1(t)$ varies very slowly. The long stability for strongly interacting systems can be explained by writing the time-depedent wave function in terms of the eigenfunctions $|\phi_i\rangle$ and use the known time evolution

$$|\Psi(t)\rangle = \sum_i \alpha_i e^{-\frac{i}{\hbar}\omega_i t} |\phi_i\rangle \,, \tag{6.1}$$

where the energy ω_i corresponds to $|\phi_i\rangle$ and α_i are the expansion coefficients. The time dependence of the occupation number on site i using Eq. 6.1 is given by

$$n_i(t) = \langle\Psi(t)| \hat{n}_i |\Psi(t)\rangle = \sum_{k,l} \alpha_k \alpha_l^* e^{-\frac{i}{\hbar}(\omega_k - \omega_l)} \langle\phi_l| \hat{n}_i |\phi_k\rangle \,. \tag{6.2}$$

For strong interactions the relative phase difference $(\omega_k - \omega_l)/\hbar$ acquired for two different eigenfunctions, i.e. off-diagonal matrix elements, is either close to zero or very large, i.e. integer multiples of U, see Fig. 5.2c. This leads to slow density fluctuations. Weakly interacting systems have a quasi-continuous energy spectrum, see

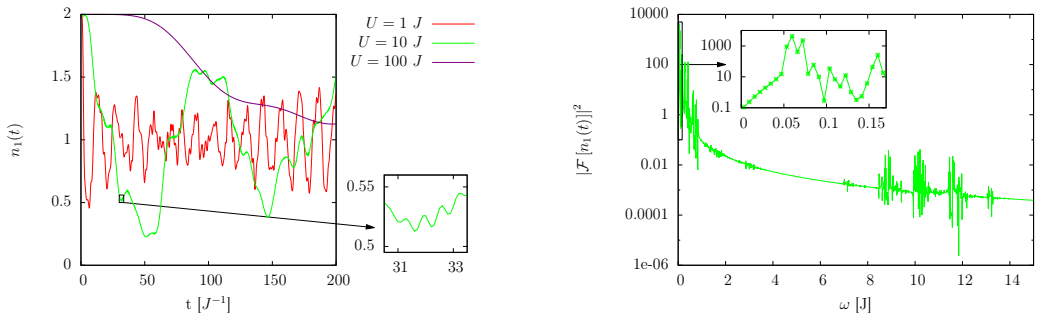

(a) (b)

Figure 6.1.: Six-site Hubbard model at half-filling: (a) Occupation number of the first site $n_1(t)$ for different interaction strengths U with the initial condition that the three leftmost sites are doubly occupied. (b) Absolute magnitude of the Fourier-transformed of the occupation number on the first site $|\mathcal{F}[n_1(t)]|^2$ for $U = 10\ J$.

Fig. 5.2a, leading to a broad interval of relative phases which explains the strong density fluctuations.
The absolute magnitude of the Fourier transform of $n_1(t)$, $|\mathcal{F}[n_1(t)]|^2$, allows to disentangle which eigenstates contribute, see Eq. 6.2. In Fig. 6.1b we see for $U = 10\ J$ two main frequency intervals with large contributions around $\omega \approx 10\ J$ and around $\omega \approx 0.06\ J$, respectively. They are related to the periodicities of the fluctuation of $n_1(t)$, i.e. $T_{\text{periodic}} = \frac{2\pi}{\omega} \approx 0.6\ J^{-1}$ and $T_{\text{periodic}} \approx 100\ J^{-1}$, respectively. The larger period is clearly visible in Fig. 6.1a for $U = 10\ J$ and the large frequency modulations can be seen as small wiggles on top of $n_1(t)$, see inset of Fig. 6.1a. The very low energy peaks, see inset of Fig 6.1b, originate from states with small energy differences, i.e. they are in same plateau of the energy spectrum. The other frequency components correspond to energy differences between states from different plateaus, see Fig 6.1b. The gap in in the excitation spectrum is clearly visible by the absence of frequency components within $\omega\ \epsilon\ [3.5 : 7]\ J$. The physical background of the small density fluctuations for large interactions is the fact that we treat a discrete model in the single-band approximation and within this model a particle can only gain the kinetic energy J by moving from one site to the other while it would loose the much larger interaction energy U. This energy mismatch is responsible for the fact that the particles can effectively only hop in pairs and form so called doublons [11, 64–66]. This fact is clearly visible when comparing $n_1(t)$, Eq. 5.14, with the two-particle occupation number on site one

$$n_1^{(double-occ.)}(t) = \langle\Psi(t)|\,\hat{n}_1\hat{n}_1\,|\Psi(t)\rangle = \langle\Psi(t)|\,\hat{n}_{1\uparrow}\hat{n}_{1\downarrow} + \hat{n}_{1\downarrow}\hat{n}_{1\uparrow}\,|\Psi(t)\rangle\,, \tag{6.3}$$

see Fig. 6.2a. Considerable deviations between the two observables can be seen for weakly interacting systems but they coincide for strong interactions. Comparing

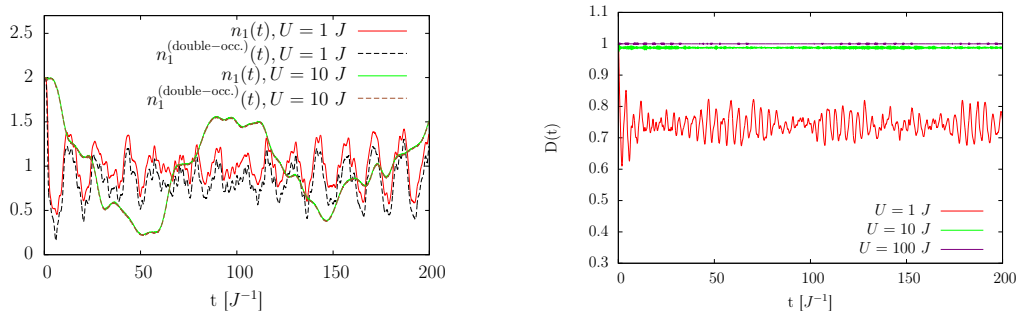

(a) (b)

Figure 6.2.: Six-site Hubbard model at half-filling: (a) One-particle (solid) n_1 and two-particle (dashed) occupation number $n_1^{(double-occ.)}$ of the first site. For $U = 10\ J$ and the lines lie on top of each other. (b) Doublon fraction, Eq. 5.8, over time for different interaction strengths. The inital condition was that the three leftmost sites were doubly occupied.

the doublon fraction D, Eq. 5.8, we observe that for low interactions the number of doubly occupied sites strongly fluctuates. For strong interactions D remains practically one, see Fig. 6.2b. We can derive this pair-wise hopping by requiring that

$$n_1(t) = n_1^{(double-occ.)}(t). \tag{6.4}$$

We expand $|\Psi(t)\rangle$ in the basis of the spin-dependent occupation numbers $n_{i\sigma}$

$$|\Psi(t)\rangle = \sum_{\{\vec{n}\}} C_{\vec{n}}(t)\, |n_{1\uparrow}, n_{1\downarrow}, ..., n_{r\uparrow}, n_{r\downarrow}\rangle\,, \tag{6.5}$$

where the sum goes over all possible configurations $\vec{n}$, $C_{\vec{n}}(t)$ is the expansion coefficient of the configuration $\vec{n}$ and r is the number of sites. $n_{i\sigma}$ can only be 0 or 1 since we treat a fermionic system. Evaluating Eq. 5.14 and Eq. 6.3 we obtain

$$n_1(t) = \sum_{\{\vec{n}\}} |C_{\vec{n}}(t)|^2\, (n_{1\uparrow} + n_{1\downarrow}) \tag{6.6}$$

$$n_1^{(double-occ.)}(t) = \sum_{\{\vec{n}\}} |C_{\vec{n}}(t)|^2\, (n_{1\uparrow} n_{1\downarrow} + n_{1\downarrow} n_{1\uparrow})\,. \tag{6.7}$$

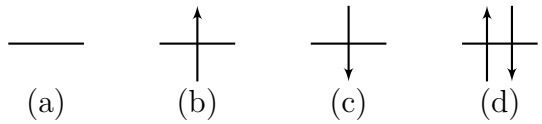

(a) (b) (c) (d)

Figure 6.3.: Graphical representation of the possible occupations of each site in the Hubbard model.

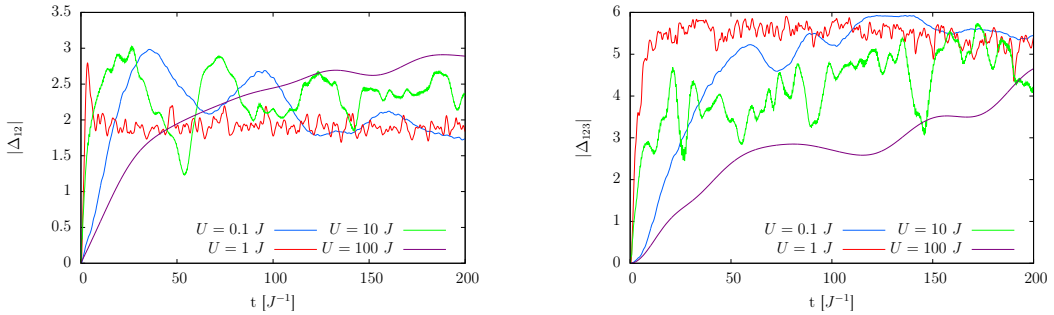

(a) (b)

Figure 6.4.: Six-site Hubbard model at half-filling: Time dependence of the magnitude of (a) the two-particle cumulant $|\Delta_{12}|$ and (b) the three-particle cumulant $|\Delta_{123}|$, Eq. 3.25, for different interaction strengths. The initial configuration was that all particles were on the left half of the Hubbard chain.

Enforcing Eq. 6.4 we obtain

$$n_{1\uparrow} + n_{1\downarrow} = n_{1\uparrow}n_{1\downarrow} + n_{1\downarrow}n_{1\uparrow}. \tag{6.8}$$

Comparing the possible occupations for each site in the Hubbard model we see that Eq. 6.8 only holds if the site is not occupied or doubly occupied, see Fig. 6.3 (a) and (d). Eq. 6.8 is not fulfilled for single occupations, see Fig. 6.3 (b) and (c). In this way the expansion coefficients $C_{\vec{n}}(t)$ for configurations with single occupied sites, Eq. 6.5, are zero for all times. That means that if Eq. 6.4 holds for all times we can describe the system purely by the hopping of pairs (doublons). Doublons have already been observed in experiment [11, 64] as well as their interaction dependent lifetime [65, 66].

6.2. Time-dependence of the correlation strength

To quantify correlations we show the absolute magnitude of Δ_{12} and Δ_{123} which show a steep increase at the beginning for weak interactions and fluctuations around an approximately constant mean afterwards, see Fig. 6.4a and Fig. 6.4b. For strong interactions the rise is rather slow due to the slow variation in the density matrices. The time at which the maximum value of $|\Delta_{12}|$ and $|\Delta_{123}|$ is reached decreases in the interval $U\ \epsilon\ [0:1\ J]$ and increases for $U > 1\ J$. This means that for weakly interacting systems correlations build up faster with increasing the interaction strength. For strongly interacting systems correlations build up slower because the system is much more rigid. We observe that three-particle correlations reach their maximum value for later times as two-particle correlations. We empirically observe saturation of $|\Delta_{123}|_{\max} \approx 6$ and saturation of $|\Delta_{12}|_{\max} \approx 3$. The saturation of $|\Delta_{123}|$

and $|\Delta_{12}|$ is also observed for the four-site and the eight-site Hubbard model at half-filling. However the values of $|\Delta_{123}|_{\max}$ and $|\Delta_{12}|_{\max}$ depend on the particle and site number. So far the explicit values for of $|\Delta_{12}|_{\max}$ and $|\Delta_{123}|_{\max}$ remain an open question.
In the TD-2RDM method we use the approximation $\Delta_{123} \approx 0$ which is not fulfilled for the investigated system, see Fig. 6.4b. We thus expect the TD-2RDM method to work best for weak interactions and short times since there three-particle correlations are weak, see Fig. 6.4b. For strong interactions three-particle correlations are weak as well for short times but since in the collision operator Δ_{123} is multiplied with the interaction strength U, see Eq. 4.5, we do not expect the TD-2RDM method to give accurate results for this regime.
To investigate whether the density entropies $S_1^{(\rho)}$ and $S_2^{(\rho)}$, Eq. 3.27b and Eq. 3.27b, provides a good measure for two-particle correlations we first compare them to the natural entropies S_1 and S_2, Eq. 3.26a and Eq. 3.26b, and then relate their time dependence to the time dependence of $|\Delta_{12}|$. $S_1^{(\rho)}$ and $S_2^{(\rho)}$ show a very similar behavior as S_1 and S_2 for $U \geq 1\ J$ see Fig. 6.5a, c and Fig. 6.5b, d. For $U \geq 1\ J$ the density entropy $S_1^{(\rho)}$ and the natural entropy S_1 are practically identical, see Fig. 6.5e. This is because the occupation numbers $n_i(t)$ are very close to the natural occupation numbers $\lambda^{(1)}$ of the 1-RDM which means that the 1-RDM is almost diagonal in the site basis. S_2 and $S_2^{(\rho)}$ show the same qualitative time dependence but are different in absolute magnitude. The reason for this is the following. The geminal occupation numbers $\lambda^{(2)}$ are not bounded between zero and one as the spin-dependent two-particle occupation numbers

$$n_{i\sigma,j\sigma'}^{(double-occ.)}(t) = \langle \Psi(t) | \, \hat{n}_{i\sigma} \hat{n}_{j\sigma'} \, | \Psi(t) \rangle \, , \tag{6.9}$$

of the sites i and j with spin σ and σ' are [59]. For the six-site Hubbard model the maximum value for $\lambda^{(2)}$ is

$$\lambda^{(2)}_{\max} = 2, \tag{6.10}$$

if the 2-RDM is normalized to $\binom{N}{2}$ [59], see Sec. 3.4. Investigating the geminal occupation numbers of the singlet part $\lambda^{(2)}_{\text{singlet}}$ of the 2-RDM, see Fig. 6.6a, b, c, we, indeed, see such highly occupied geminals. We observe that there is maximally one geminal occupation number of the singlet part $\lambda^{(2)}_{\text{singlet}} > 1$ while all others are strictly smaller than one. The geminal occupation numbers of the triplet part $\lambda^{(2)}_{\text{triplet}}$ are always smaller than one in the investigated time span (not shown). If one $\lambda^{(2)}$ is greater than one this is a sign of pairing between two particles [59]. Such a state is strongly correlated as revealed by $|\Delta_{12}|$, Fig. 6.4a. The entropy S_2, however, gives a small value for a state where one geminal occupation number reaches $\lambda^{(2)}_{\max}$ and all others are weakly occupied compared to a state where all geminal occupation numbers have the same weight, see Sec. 3.4. For a specific example, compare $\lambda^{(2)}_{\text{singlet}}$ for $t = 106\ J^{-1}$ for $U = 10\ J$ and $U = 100\ J$ in Fig. 6.6b. Both have almost the

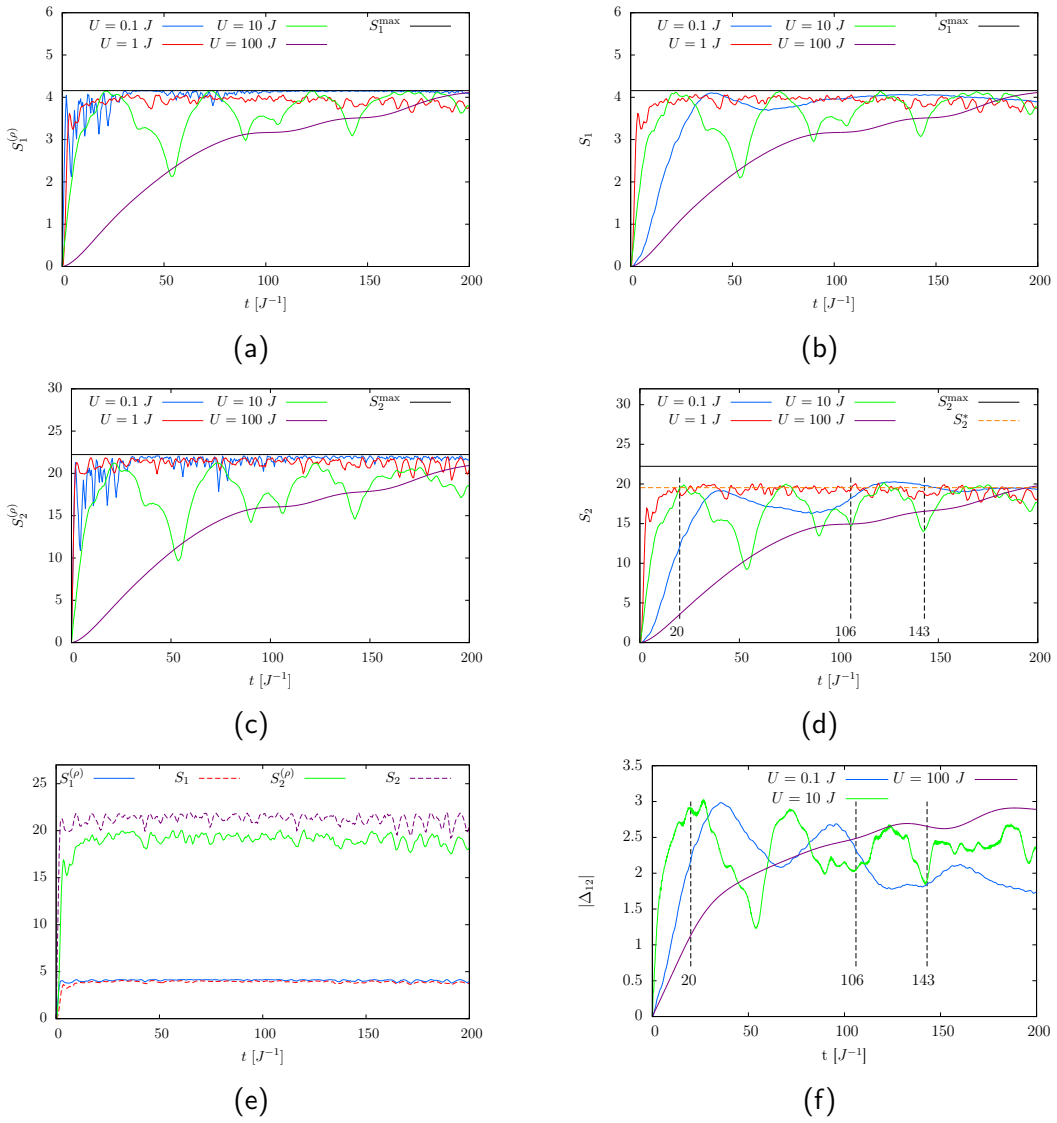

Figure 6.5.: Six-site Hubbard model at half-filling with different interaction strengths U: (a), (c) Density entropies $S_1^{(\rho)}$, $S_2^{(\rho)}$, Eq. 3.27, and (b), (d) natural entropies S_1, S_2, Eq. 3.26. (e) Comparison of the density $S_1^{(\rho)}$, $S_2^{(\rho)}$ and natural entropies S_1, S_2 for $U = 1\ J$. (f) Time dependence of the magnitude of the two-particle cumulant $|\Delta_{12}|$ for $U = 10\ J$ and $U = 100\ J$. Initially the three leftmost sites were doubly occupied for all (a)-(f).

same value of S_2 for $t = 106\ J^{-1}$, see Fig. 6.5d, but the distribution of the $\lambda^{(2)}_{\text{singlet}}$ is considerably different. This state is more correlated than a state with a broad distribution of geminal occupation numbers $\lambda^{(2)}$ that are smaller than one, see also Sec. 3.4.
From this it follows that if one geminal occupation number $\lambda^{(2)}$ is greater than one, S_2 and $S_2^{(\rho)}$ predict a too small correlation. As an example, compare S_2 for $U = 0.1\ J$ and $U = 100\ J$ for $t = 143\ J^{-1}$ where the weakly interacting systems appears to be stronger correlated, see Fig. 6.5d. $|\Delta_{12}|$ reveals that for this time the strongly interacting system is actually much more correlated than the weakly interacting system, see Fig. 6.4a.

In summary, the experimentally easily accessible measures $S_2^{(\rho)}$ and especially $S_1^{(\rho)}$ are capable to reveal the basic time-dependence of two-particle correlations, compare Fig. 6.5a, c with Fig. 6.5f. Their values on an absolute scale, however, have to be taken with caution.

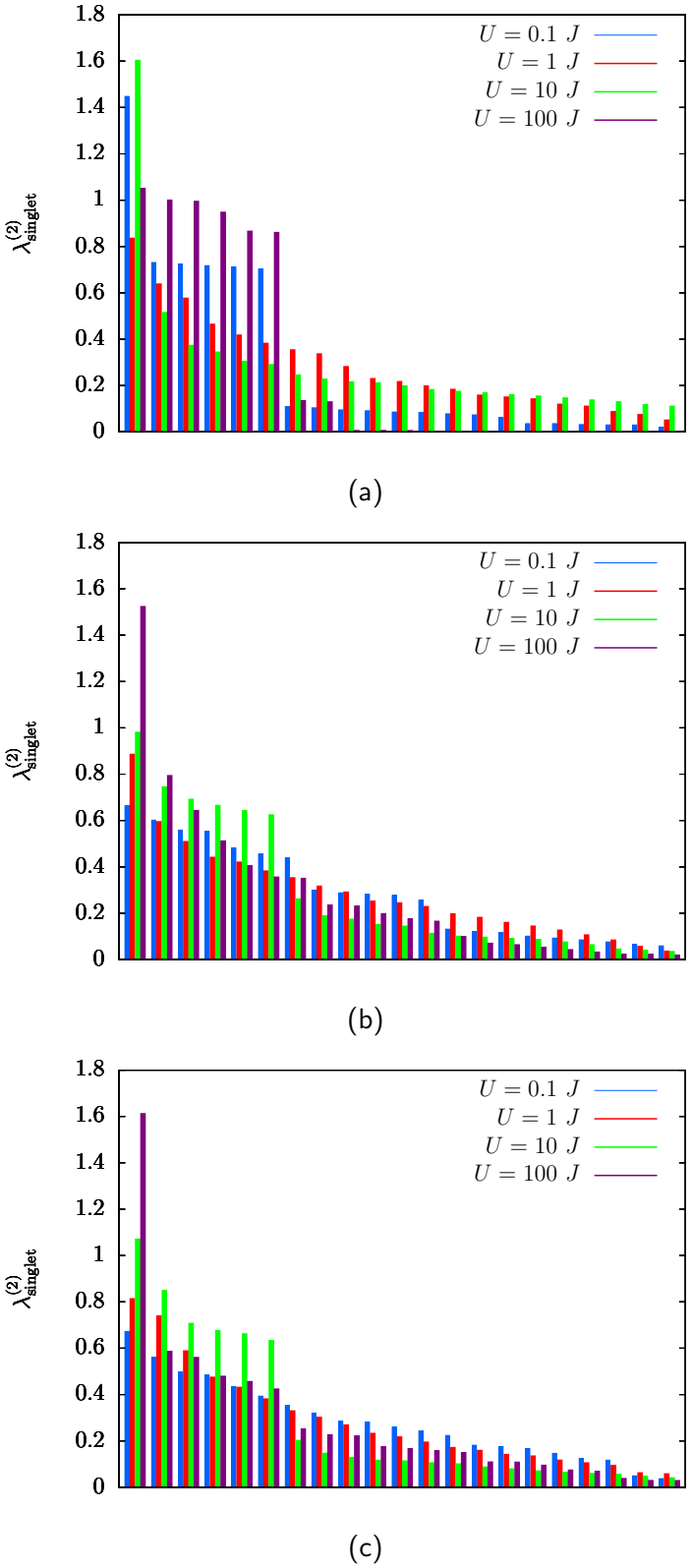

Figure 6.6.: Histogram of the geminal occupation numbers of the singlet part $\lambda^{(2)}_{\text{singlet}}$ of the 2-RDM for different interaction strengths U at different times t of a six-site Hubbard chain at half-filling. (a) $t = 20\ J^{-1}$, (b) $t = 106\ J^{-1}$ and (c) $t = 143 J^{-1}$. Initially all particles where on the left half of the Hubbard chain. For this calculation the 2-RDM was normalized to $\binom{N}{2}$, contrary to Eq. 3.5.

7. TD-2RDM method applied to the Hubbard model at half-filling

Comparing the TD-2RDM method to previous results in literature obtained with similar methods [24–26] we apply it to highly excited states. We expect the applicability for the TD-2RDM method to be limited to this regime based on the results in the previous section since three-particle correlations can not be neglected.

7.1. Convergence

Before we show our results we study the convergence of the TD-2RDM method with and without purification. As an example we use the six-site Hubbard model with $U = 0.1\ J$ and the initial condition that the three left most sites are doubly occupied. Without purification the results are converged already for $\Delta t = 0.1\ J^{-1}$, see Fig. 7.1a. This is true using the contraction consistent Valdemoro reconstruction as well as the contraction consistent NY reconstruction. The EC purification, however, does not converge with decreasing time step, see Fig. 7.1b. This is because of the strong manipulation of the geminal occupation numbers $\lambda^{(2)}$ involved with the EC purification. Furthermore for some Δt unphysical jumps and kinks appear in the results, e.g. for $t \approx 45\ J^{-1}$ with $\Delta t = 0.001\ J^{-1}$. These jumps are due to the simple purification scheme which can lead to large discontinuous adjustments of the geminal occupation numbers $\lambda^{(2)}$. We conclude that we avoid purification whenever possible since the EC purification does not converge and can lead to an unphysical behavior of the observables. We note that if we do use the EC purification we have to decrease the time step considerably in order to obtain at least partially converged results. For the Alcoba purification we observe convergence for the same Δt as for the propagation without purification (not shown).

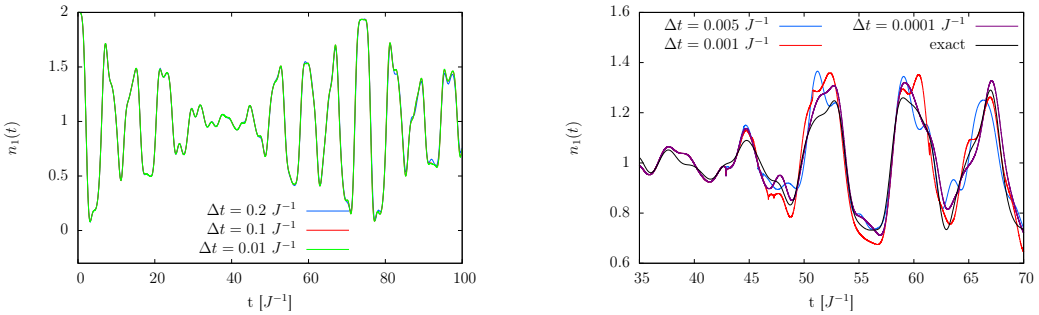

(a) (b)

Figure 7.1.: Six-site Hubbard model at half-filling with $U = 0.1\ J$: (a) Occupation number on site one $n_1(t)$ obtained within the TD-2RDM method without purification using the contraction consistent NY-reconstruction for different time steps Δt. (b) Occupation number on site one $n_1(t)$ obtained within the TD-2RDM method with the EC purification using the contraction consistent NY-reconstruction for different time steps Δt. The initial state corresponds to the leftmost sites being doubly occupied.

7.2. Comparison of purifications

We test several purification schemes for a six-site Hubbard model at half-filling with $U = 0.1\ J$ for the initial condition that the three leftmost sites are doubly occupied. Applying the Alcoba purification used in [23] and comparing it to the results obtained using the EC purification we observe that the Alcoba purification does not conserve energy for both reconstructions, see Fig. 7.2a. The EC purification does conserve the energy to high accuracy for the contraction consistent NY reconstruction and to higher accuracy than the Alcoba purification for the contraction consistent Valdemoro reconstruction. To quantify the accuracy of the different reconstructions and purifications we compare the occupation number on site one $n_1(t)$, see Fig. 7.2b. We observe that both purifications give similar results for the Valdemoro reconstruction. For the NY reconstruction with the Alcoba purification we obtain similar results. The results obtained using the EC purification with the NY reconstruction reproduce the exact results very accurately up to $t = 80\ J^{-1}$. We see that both purifications stabilize the propagation for all reconstructions, see Fig. 7.2c. Without purification both reconstructions lead to a break-down of the TD-2RDM method. Energy conservation is, thus, essential for the systems investigated. We, therefore, use the EC purification when necessary despite the error associated with it due to the insufficient convergence with Δt.

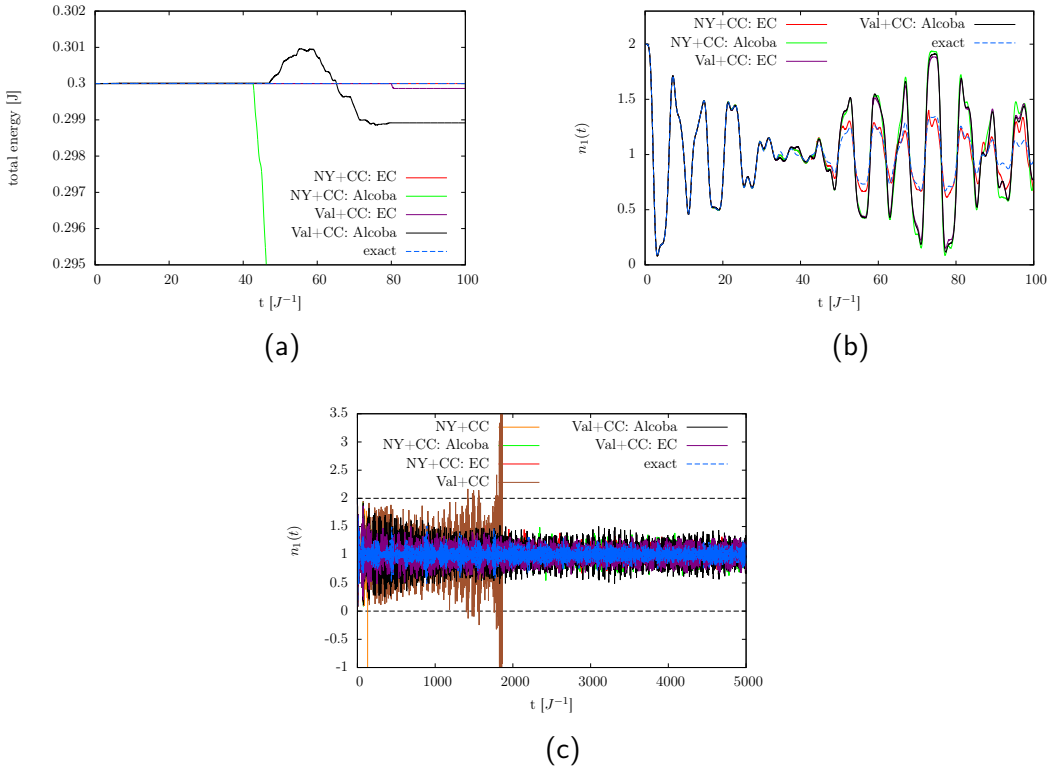

Figure 7.2.: Six-site Hubbard model at half-filling with $U = 0.1\ J$: (a) Total energy and (b) occupation number on site one $n_1(t)$ obtained within the TD-2RDM method with different purifications and different reconstructions for the 3-RDM. The time step Δt was $0.01\ J^{-1}$. (c) The same as (b) but for a longer propagation time and a different time step $\Delta t = 0.1\ J^{-1}$. The initial state corresponds to the leftmost sites being doubly occupied. The dashed lines show the allowed minimum and maximum value of $n_1(t)$.

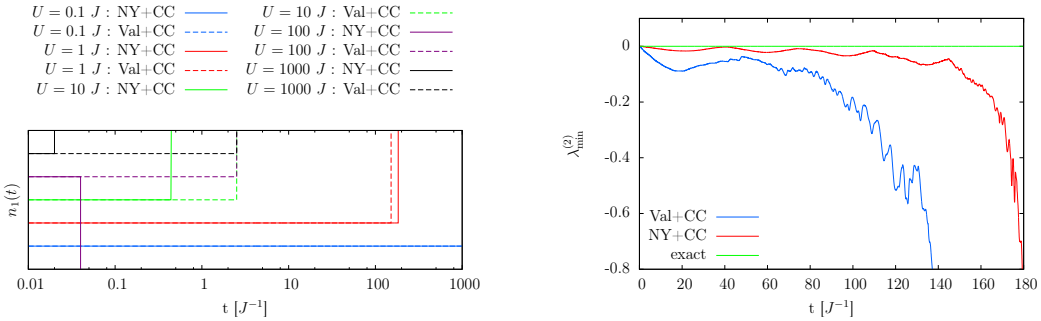

(a) (b)

Figure 7.3.: Eight-site Hubbard model at half-filling using different methods and interaction strengths U: (a) Occupation number of the first lattice site $n_1(t)$ for the ground state propagated within the TD-2RDM method. For clarity the curves are shifted horizontally and all have an initial value of one. (b) Minimal geminal occupation number $\lambda^{(2)}_{\text{min}}$ of the 2-RDM in comparison with the exact calculation for $U = 1\ J$. The time step Δt was $0.02\ J^{-1}$.

7.3. Instabilities

To test the time scales over which the TD-2RDM method remains stable we propagate the ground state (obtained via exact diagonalization) of the eight-site Hubbard model at half-filling. In this case, all properties of the system should stay constant over time. However, due to the N-representability problem we expect, in accordance with literature [23, 24], to find instabilities in the propagation. In Fig. 7.3a we see that for weak interactions, $U = 0.1\ J$, the propagation of the ground state is stable over the complete investigated time interval. Increasing the interaction strength leads to instabilities emerging earlier in the propagation such that already for $U = 10\ J$ the propagation is only stable up to $t \approx 3\ J^{-1}$. Comparing different reconstructions for the 3-RDM we see that for $U < 10\ J$ the contraction consistent NY reconstruction yields better results but for larger interaction strengths the propagation is very unstable. For the contraction consistent Valdemoro reconstruction the propagation always breaks down around the same time for the largest U investigated, see Fig. 7.3a. Although in Fig. 7.3a the instabilities appear to develop instantaneously at some time, D_{12} acquires only a small error at each propagation step which accumulates over time leading to an eventual break down of the TD-2RDM method. This can be observed in the geminal occupation numbers $\lambda^{(2)}$ of D_{12} where we see that the smallest geminal occupation number $\lambda^{(2)}_{\text{min}}$ is smaller than zero almost immediately after the start of the propagation. This error adds up continuously until the propagation breaks down, see Fig. 7.3b. This is a manifestation of the violation of N-representability since D_{12} has to be positive semidefinite, see Sec. 3.3.1. We observe that for $U = 1\ J$, $\lambda^{(2)}_{\text{min}}$ is less negative within the

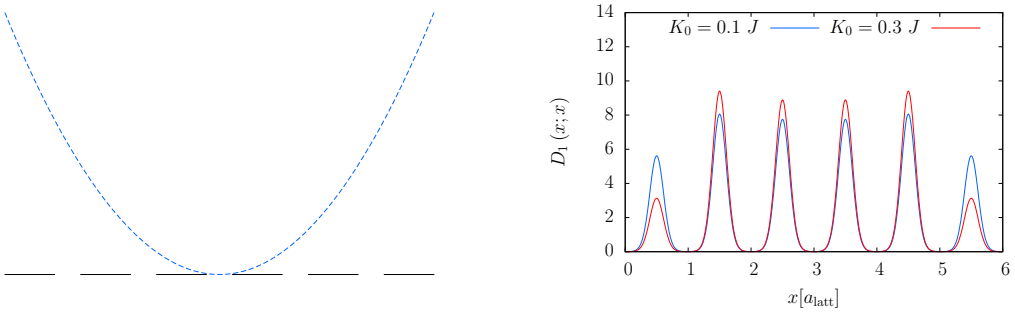

(a) (b)

Figure 7.4.: (a) Sketch of the harmonic potential (blue dashed line) superimposed onto the Hubbard model. (b) Ground state density for a six-site Hubbard model at half-filling for different strengths of the harmonic potential V_0, Eq. 7.1, with $U = 0.1\ J$.

contraction consistent NY reconstruction than within the contraction consistent Valdemoro reconstruction at each instant of time. This is a direct indication for the NY approximation being more accurate at this interaction strength.

7.4. Propagating from weakly correlated states using potential quenches

In Sec. 5.3 and Sec. 5.4 we predicted that the TD-2RDM method should be applicable for weakly interacting and weakly correlated systems. To delimit the applicability of the TD-2RDM method we investigate a weakly correlated state where we expect the TD-2RDM method to give good results. To do so we superimpose a harmonic potential to the Hubbard model. The Hamiltonian is then given by

$$H_{\mathrm{HC}} = -J \sum_{\substack{\langle i,j\rangle \\ \sigma\epsilon(\downarrow,\uparrow)}} \hat{a}^{\dagger}_{i,\sigma}\hat{a}_{j,\sigma} + U\sum_{i}\hat{n}_{i,\uparrow}\hat{n}_{i,\downarrow} + K_0\sum_{i}\left(i - \frac{N+1}{2}\right)^2 \hat{n}_i, \tag{7.1}$$

where K_0 is the amplitude of the harmonic potential, see Fig. 7.4a for a sketch. We calculate the ground state of this system for different potential amplitudes K_0, see Fig.7.4b, and monitor the time evolution after switching off the harmonic potential. Such potential quenches can also be applied in experiments, e.g. [67]. This potential quench leads to density fluctuations. We use the TD-2RDM method with the contraction consistent NY reconstruction and an interaction strength of $U = 0.1\ J$. The density fluctuations on site one $n_1(t)$ can be reproduced very well for weak interaction quenches, i.e. $K_0 = 0.1\ J$, see Fig. 7.5a. Investigating

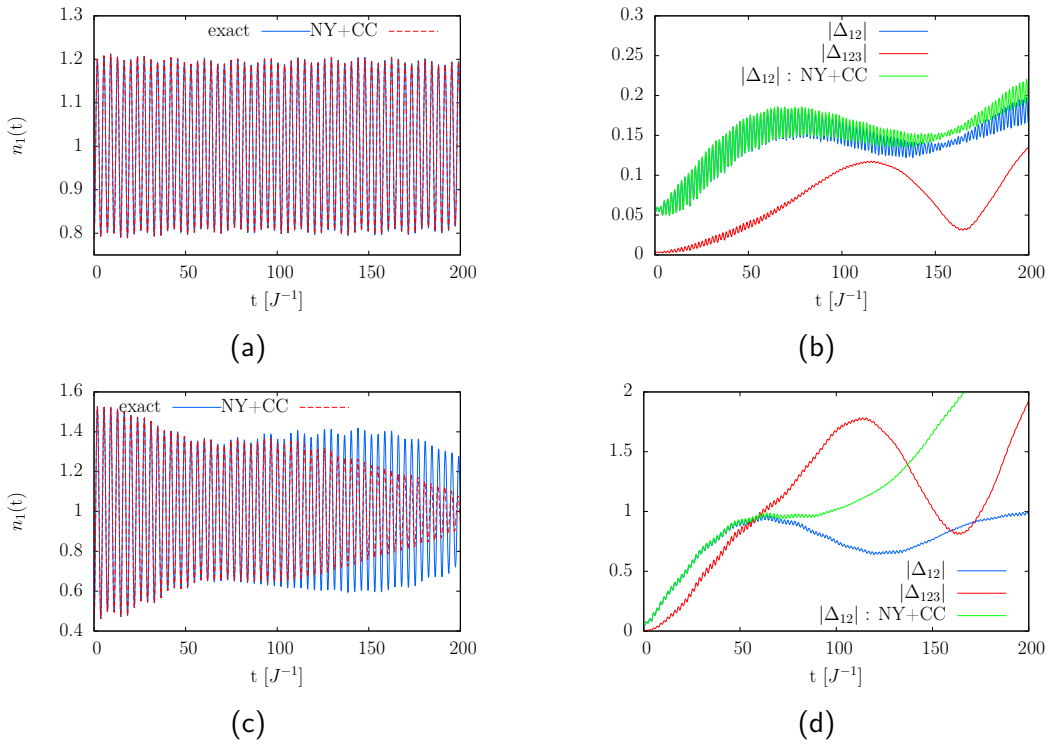

Figure 7.5.: Six-site Hubbard model at half-filling with $U = 0.1\ J$: (a), (c) Occupation number on site one $n_1(t)$ within the TD-2RDM method using the contraction consistent NY reconstruction compared to the exact calculation. For (a) $K_0 = 0.1\ J$ and (c) $K_0 = 0.3\ J$. (b), (d) Magnitude of the two-particle and three-particle cumulant, Eq. 3.25, obtained in the exact calculation compared to the magnitude of the two-particle cumulant calculated within the TD-2RDM method. The initial state of (a) and (b) is the ground state of Eq. 7.1 with $K_0 = 0.1\ J$. The initial state of (c) and (d) is the ground state of Eq. 7.1 with $K_0 = 0.3\ J$. The time step Δt was $0.1\ J^{-1}$.

the magnitude of the two-particle and three-particle cumulant we observe that we, indeed, produced a weakly correlated state as desired, see Fig. 7.5b. For a stronger potential quench, i.e. $K_0 = 0.3$, we observe that the TD-2RDM can only reproduce the exact fluctuations up to $t < 80\ J^{-1}$. This coincides with a significant rise of the three-particle cumulant which is not taken account by in the reconstruction, see Fig. 7.5d. Nevertheless, initially the state is only weakly correlated as for weak interaction quenches, see Fig. 7.5d. Comparing the magnitude of the two-particle cumulant $|\Delta_{12}|$ obtained within the exact calculation and within the TD-2RDM method we observe that the two-particle correlation is represented very well for weak quenches, see Fig. 7.5b. For stronger quenches, $|\Delta_{12}|$ calculated within the TD-2RDM method shows considerable deviations from the exact calculations for $t > 50\ J^{-1}$.

7.5. Propagation of highly excited but initially uncorrelated states

The success of the TD-2RDM method relies strongly on the assumption that $\Delta_{123} \approx 0$. As shown in Sec. 5.4 this assumption only holds for weakly interacting systems and low excited states. The systems studied in literature [24–26] are weakly interacting but highly excited. In this chapter we compare the performance of the TD-2RDM method with results from [24–26].

Four-site Hubbard model

We start with the four-site Hubbard model at half-filling, see [24]. We employ the EC purification scheme which only considers the semi-definiteness of the 2-RDM. We observe that the NY reconstruction reproduces the exact calculation better than the Valdemoro reconstruction for $t > 20\ J^{-1}$. However for $t > 80\ J^{-1}$ both reconstructions show large deviations, see Fig. 7.6a. We do not use the contraction consistent extension here because this is not possible for four particles on four sites [23]. In contrast to [24] we observe no instabilities during the long time propagation and also the geminal occupation numbers $\lambda^{(2)}$ stay within reasonable bounds, see Fig. 7.6b. The stability is achieved through purification after each time step. If we do not purify we observe the same instabilities as found in [24]. Since we do not use the contraction consistent extension the reconstructed 3-RDM does not contract correctly onto the 2-RDM and energy conservation is not fulfilled [23], see Fig. 7.7a. Hence we observe fluctuations in the total energy for both reconstructions. These energy fluctuations were also observed in [24]. To get a closer insight into the dynamics of the system we decompose the total energy E_{tot}

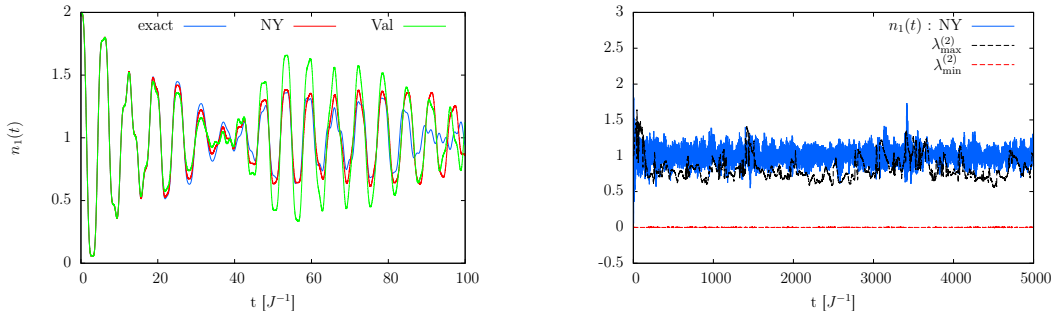

(a) (b)

Figure 7.6.: Four-site Hubbard model at half-filling with $U = 0.1\ J$: (a) The occupation number of the first site $n_1(t)$ obtained via the TD-2RDM method for the Valdemoro and the NY reconstruction compared to the exact result. The time step Δt is $0.001\ J^{-1}$. (b) The occupation number of the first site $n_1(t)$ obtained via the TD-2RDM method with the NY reconstruction and the minimal and maximal geminal occupation number obtained via the exact calculation, $\lambda^{(2)}_{\min}$ and $\lambda^{(2)}_{\max}$. The time step Δt is $0.05\ J^{-1}$. Initially all particles were on the two leftmost sites.

into its different components, namely the interaction energy

$$E_{\text{int}} = \frac{1}{2}\text{Tr}\left(\text{V}_{1,2}\ \text{D}_{12}\right), \tag{7.2}$$

where $V_{1,2}$ is the interaction part of the full two-particle Hamiltonian H_{12}, see Eq. 4.8, the interaction part of the Hartree-Fock energy E_{HF} given by

$$E_{\text{HF}} = \frac{1}{2}\text{Tr}\left(\text{V}_{1,2}\ 2\ \text{D}_1 \wedge \text{D}_2\right) = \text{U}\sum_{\text{i}} \text{n}_{\text{i}\uparrow}\text{n}_{\text{i}\downarrow}, \tag{7.3}$$

the correlation energy

$$E_{\text{corr}} = E_{\text{int}} - E_{\text{HF}} = \frac{1}{2}\text{Tr}\left(\text{V}_{1,2}\ \Delta_{12}\right), \tag{7.4}$$

and the kinetic energy

$$E_{\text{kin}} = E_{\text{tot}} - E_{\text{int}}. \tag{7.5}$$

We note that E_{HF} does not contain an exchange contribution for the Hubbard model, and that E_{corr} is defined in accordance with many-body quantum theories beyond Hartree-Fock. For the investigated system we observe that E_{HF} is converted rapidly into kinetic energy E_{kin} and that the correlation energy E_{corr} is a large contribution for $t > 20\ J$. This means that the system is strongly correlated for $t > 20\ J$. E_{HF} amounts to approximately half of the total energy where

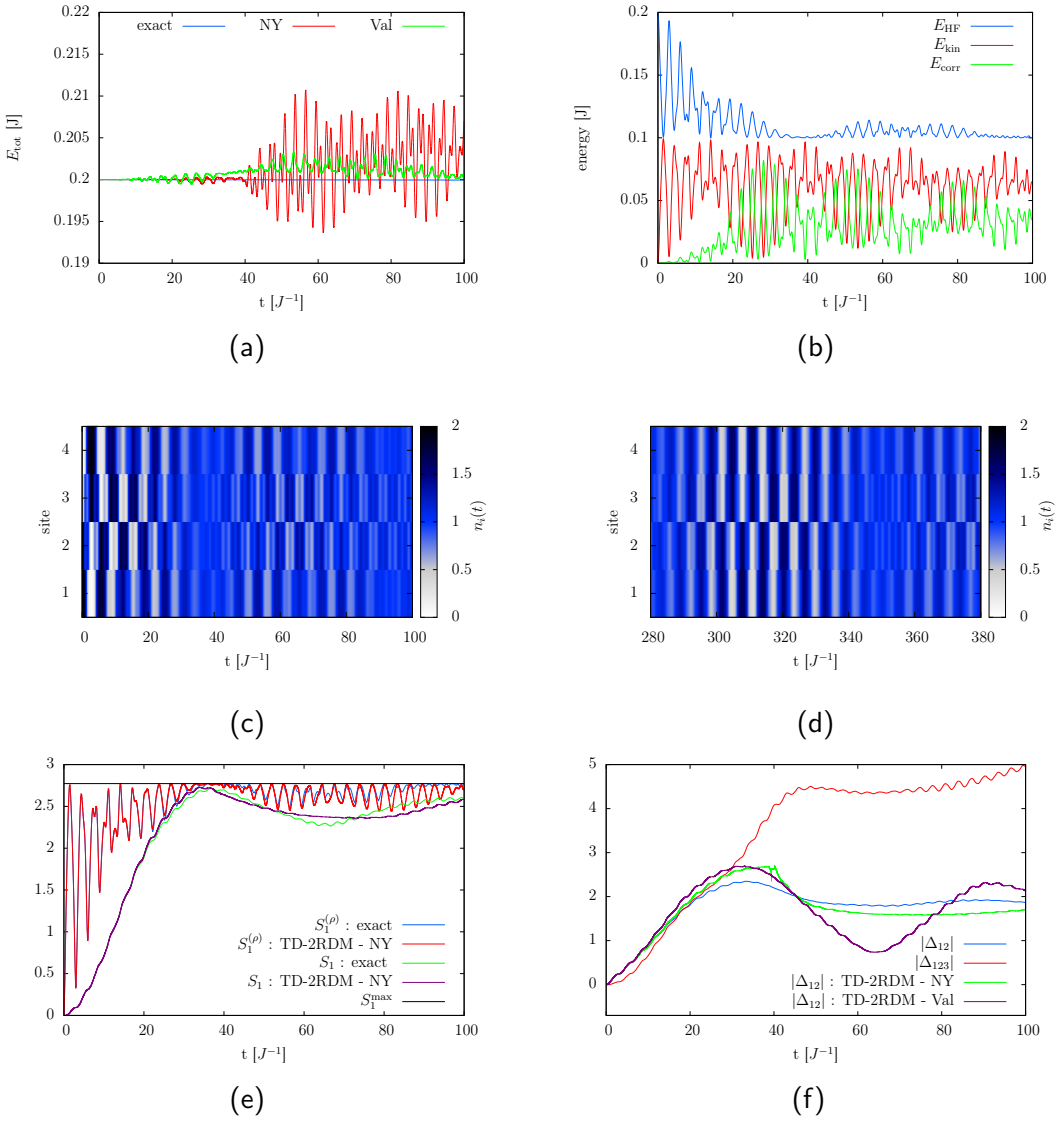

Figure 7.7.: Four-site Hubbard model at half-filling with $U = 0.1\ J$: (a) Total energy E_{tot} during the propagation within the TD-2RDM compared to the exact calculation. (b) Individual energy contributions within the exact calculation, where E_{HF} is the Hartree-Fock energy, E_{kin} is the kinetic energy, and E_{corr} is the correlation energy. (c), (d) Occupation numbers $n_i(t)$ over time and for all lattice sites. (e) S_1, Eq. 3.26, and $S_1^{(\rho)}$, Eq. 3.27, within the exact calculation compared to the results for $S_1^{(\rho)}$ within TD-2RDM method. (f) Magnitude of the two-particle $|\Delta_{12}|$ and three-particle cumulant $|\Delta_{123}|$ obtained within in the exact calculation compared to $|\Delta_{12}|$ calculated within in the TD-2RDM method with the NY and the Valdemoro reconstruction. The initial state corresponds to the two leftmost sites being occupied by two particles, respectively.

the remaining energy is distributed to kinetic and correlation energy. The particle density fluctuates over the lattice sites and shows sequences of homogeneous distribution and subsequent revivals close to the initial state, see Fig. 7.7c and Fig. 7.7d. Observing the correlation measures used in the previous sections we see that the natural entropy S_1, Eq. 3.26, and the density entropy for the 1-RDM $S_1^{(\rho)}$, Eq. 3.27, both have maxima at $t \approx 35\ J^{-1}$, see Fig. 7.7e. Already for $t \approx 30\ J^{-1}$ we see deviations between the occupation of site one $n_1(t)$ for the exact calculation and the TD-2RDM method which is due to the strong three-particle correlation at this time, see Fig. 7.7f. After this correlation peak the system gets less correlated such that the TD-2RDM gives results of comparable quality, i.e. the phase of $n_1(t)$ is tracked correctly but the amplitude is too large. For $t > 75J^{-1}$ correlations increase again, see Fig. 7.7f, and the TD-2RDM method does not reproduce the exact calculation anymore, see Fig. 7.6a. Comparing $|\Delta_{12}|$ obtained within the TD-2RDM method with the exact calculation we see that the NY reconstruction reproduces the magnitude of the two-particle correlation quite well while the Valdemoro approximation shows a qualitatively different behavior. Investigating the time evolution of $|\Delta_{123}|$ we see that the TD-2RDM method performs surprisingly well, since three-particle correlations are very large over the complete investigated time interval. Comparing the density fluctuations with $|\Delta_{12}|$ we observe that a smeared density corresponds to strong three-particle correlations, see Fig. 7.7c and Fig. 7.7f.

Eight-site Hubbard model

We now compare our results with the results of Hermanns et al. [26] for the eight-site Hubbard model at half-filling. In [26] a Green's function method is used which is similar to the TD-2RDM method. The assumption is that $\Delta_{123} = 0$ but also Δ_{12} is used only in an approximate form [25, 26]. When comparing to our equations of motion for D_{12}, Eq. 3.16, inserting the expansion $D_{12} = 2D_1 \wedge D_1 + \Delta_{12}$, Eq. 3.9b, an equation of motion for Δ_{12} follows. The second-order Born approximation on the level of the equation of motion of Δ_{12} neglects the term $[V_{12}, \Delta_{12}]$ and terms of the form $\mathrm{Tr}_3\,[\mathrm{V}_{13}, \mathrm{D}_1\Delta_{23}]$. The equations of motion for Δ_{12} contains a source term of the form $(1 - D_1 - D_2)\, V_{12} D_1 D_2 - D_1 D_2 V_{12} \left(1 - D_1^\dagger - D_2^\dagger\right)$. For details see [39] chapter 3 and chapter 6.

Since Δ_{12} is vanishing for the present initial condition we expect the results of the Green's function method to become worse with increasing time. We use the EC purification which only considers the semi-definiteness of D_{12}. Initially, all particles are confined to the four leftmost sites of the Hubbard chain.

The occupation number on the first site $n_1(t)$ obtained within the contraction consistent NY reconstruction shows good agreement with the exact result and shows improvement compared to the results of [26], compare Fig. 7.8a and the HF-GKBA

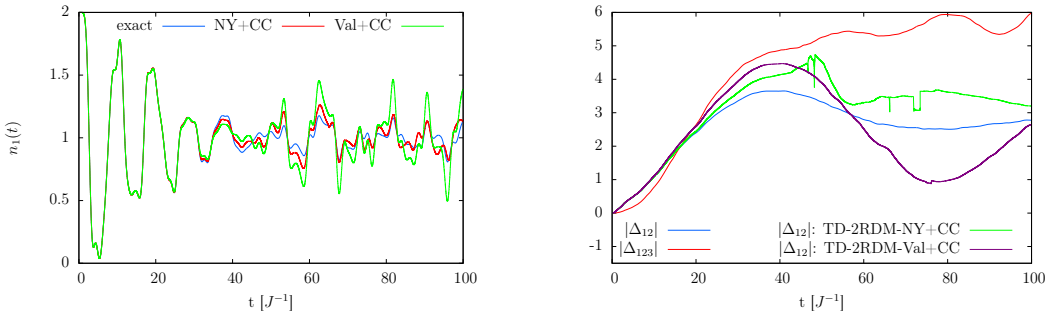

(a) (b)

Figure 7.8.: Eight-site Hubbard model at half-filling with $U = 0.1\ J$: (a) Occupation number of the first site $n_1(t)$ obtained within the TD-2RDM method for the contraction consistent Valdemoro and the contraction consistent NY reconstruction compared to the exact result. The time step Δt was $0.001\ J^{-1}$. (b) Magnitude of the two-particle $|\Delta_{12}|$ and three-particle cumulant $|\Delta_{123}|$, Eq. 3.25 obtained within in the exact calculation.

curve in Fig. (4) of [26]. The results obtained within the contraction consistent Valdemoro reconstruction show improvements relative to the results obtained in [26], e.g. $n_1(t = 96) \approx 0.25$ in [26], $n_1(t = 96) \approx 0.5$ obtained within the TD-2RDM method, and $n_1(t = 96) \approx 1.0$ obtained within the exact calculation. We observe that $n_1(t)$ obtained within the TD-2RDM method shows deviations from the exact result for $t > 35\ J^{-1}$. At this time $|\Delta_{123}|$ is already very large and three-particle correlations can thus not be neglected, see Fig. 7.8b. For $t > 35\ J^{-1}$ the contraction consistent NY reconstruction reproduces the exact calculation very accurately, while the contraction consistent Valdemoro approximation strongly overestimates the amplitudes of the density oscillations, see Fig. 7.8a. Comparing the values of $|\Delta_{12}|$ for the different reconstructions we see that the exact calculation is not reproduced well for $t > 30\ J^{-1}$, see Fig. 7.8b.

For the individual energy contributions we observe that the general dynamics for the four and eight-sites systems is very similar except for the fact that the energy contributions of the eight-site Hubbard chain show smaller fluctuations and the contribution of E_{corr} is less important, compare Fig. 7.7b and Fig. 7.9a. This observation was also discussed in [26] and used to extend the method to larger Hubbard chains since agreement is expected to be better in this case. Looking at the energy contributions obtained within the TD-2RDM method we see that especially the contraction consistent NY reconstruction shows very good agreement up to $t \approx 60\ J^{-1}$ and E_{HF} is very well reproduced even for later times, compare Fig. 7.9a and Fig. 7.9b. E_{kin} shows deviations and is in general overestimated leading to negative correlation energies for small time intervals which we do not observe in the exact calculation. The general structure, however, is resolved quite

well and is more accurate than in [26] as expected due to the equations of motions, e.g. the results in [26] do not reproduce the two dips in the kinetic energy around $t = 40\ J^{-1}$ which are very well reproduced for both reconstructions. For $t < 50\ J^{-1}$ the contraction consistent Valdemoro reconstruction shows the same results as the contraction consistent NY reconstruction, see Fig. 7.9c. For $t > 50\ J^{-1}$ the contraction consistent NY reconstruction yields more accurate results. We checked that the TD-2RDM method is of similar quality also for $U = 0.25\ J$ as in [26]. For stronger interactions however the EC purification fails and the propagation is unstable.

In density-functional theory [2] and time-dependent density functional theory [3] one often used measure for correlations is the correlation energy E_{corr}. For the Hubbard model E_{corr}, Eq. 7.4, can be written down explicitly

$$E_{\text{corr}}(\Delta_{12}) = \text{Tr}\left(\text{V}_{1,2}\Delta_{12}\right) = \text{U}\sum_{\text{i}_1}\Delta^{\text{i}_1\text{i}_1}_{\text{i}_1\text{i}_1}, \tag{7.6}$$

where we have inserted Eq. 4.8 to arrive at the last equality. Comparing the maximum of E_{corr} for different numbers of particles we observe that E_{corr} gives a larger contribution to the total energy for the smaller system, compare Fig. 7.7a and Fig. 7.9a. To understand the influence of the interaction strength on E_{corr} we investigate E_{corr} normalized to the total energy E_{tot} for a six-site Hubbard model at half-filling with the same initial condition as above. The total energy is given by $E_{\text{tot}} = 3\ U$. We observe that the normalized correlation energy rises very quickly with U such that already for $U = 10\ J$ approximately 50% of the total energy are made up by correlations, see Fig. 7.9d. These results were obtained from the exact calculation.

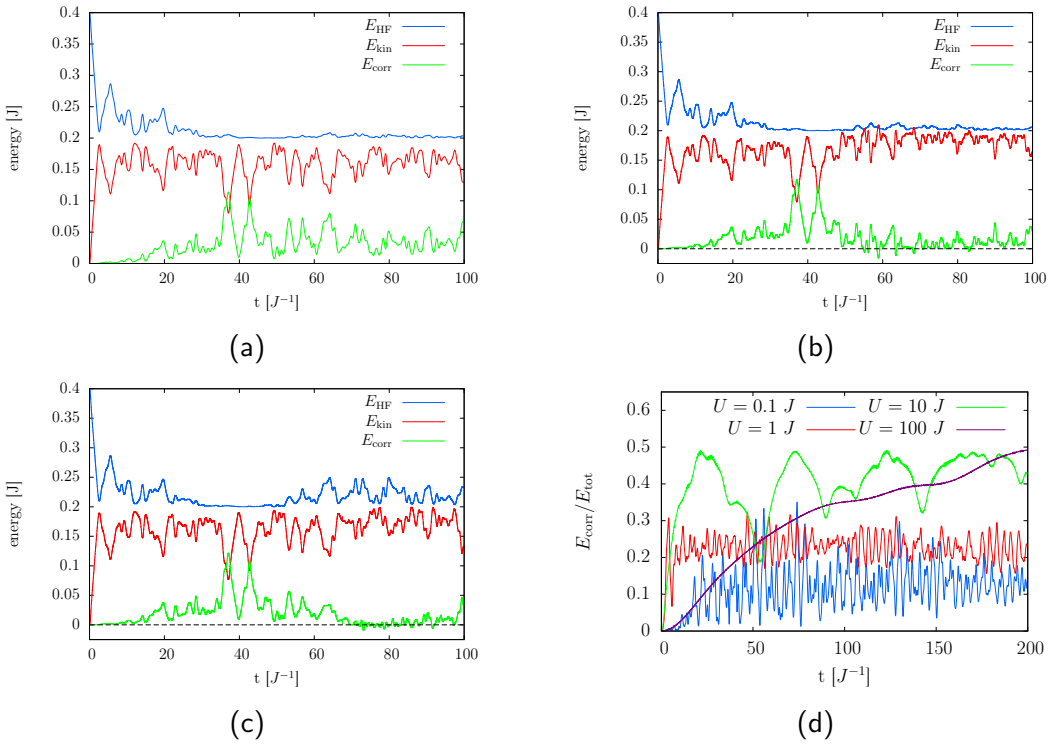

Figure 7.9.: Eight-site Hubbard model at half-filling with $U = 0.1\ J$: Individual energy contributions obtained within (a) the exact calculation, (b) the TD-2RDM method using the contraction consistent NY reconstruction, and (c) the TD-2RDM method using the contraction consistent Valdemoro reconstruction. The dashed line is a guide for the eye marking zero.
Six-site Hubbard model at half-filling for different U: (d) E_{corr}, see Eq. 7.6, normalized to the total energy E_{tot} over time obtained via the exact calculation. The total energy is given by $E_{\mathrm{tot}} = 3\ U$.
The initial configuration corresponds to all particles being on the left half of the Hubbard chain.

8. Conclusion & Outlook

Summarizing our results we have shown that correlations in quantum many-body states can be measured using cumulants. We haven seen that an accurate measure for p-particle correlations are the absolute magnitudes of the p-particle cumulants $|\Delta_{1\ldots p}|$. Entropy measures defined in analogy to the von Neumann entropy for reduced-density matrices capture the main features for time-dependent systems. On a quantitative level one important effect cannot by resolved by entropy measures, namely the condensation of particles. Considering two-particle correlations, the geminal occupation numbers of the two-particle reduced density matrix (2-RDM) can be larger than one. In this case the natural entropy for the 2-RDM S_2, Eq. 3.26b, predicts a too low level for two-particle correlations. The physics behind such highly occupied geminals is the condensation of pairs of fermions to bosonic particles which is a highly correlated state [59].
Investigating the ground state properties of the few-site Hubbard-model we have observed a maximum of three-particle correlations and a saturation of two and four-particle correlations between $U = 3\ J$ and $U = 10\ J$. In this region the one-particle reduced density matrix (1-RDM) and the 2-RDM become almost diagonal in the site-basis. This cross over resembles the Mott metal-insulator transition observed in the three-dimensional Hubbard model [56]. Quantifying the spatial distribution of correlations for weakly excited states of strongly interacting systems we have observed that the particle-particle correlation C_{particle}, Eq. 5.4, is strongest for particles occupying the same site and decays exponentially with the distance of the particles. This is an effect of the purely local interaction of the Hubbard model. However the investigated system sizes were too small to quantify this result more accurately and extract coefficients for the ground and excited states. The pair-pair correlation function $C_{\text{pair}-\text{pair}}$, Eq. 5.5, shows a maximum for nearest-neighbor sites and increases in magnitude with the interaction strength U. This can be related to the fact that the strongly interacting Hubbard model can be mapped onto a hard-core boson model with nearest-neighbor interaction [5, 62].
Examining the excited states of the Hubbard model we have found good agreement between the two-particle correlation strength $|\Delta_{12}|$ and the natural entropies for the 1-RDM and the 2-RDM, S_1 and S_2, on a qualitative level. Interestingly we have found excited states with vanishing three-particle cumulants. We have shown that these states are antisymmetrized geminal product (AGP) states [61] which are characterized by one geminal being maximally occupied and all other geminals being equally occupied.

Applying the time-dependent two-particle density matrix (TD-2RDM) method [23] we have derived the equations of motion for 2-RDM for the one-dimensional Hubbard model. We have used two different reconstructions of the three-particle reduced density matrix (3-RDM) and compared them with each other. The contraction-consistent Valdemoro reconstruction [50] makes the assumption that the three-particle cumulant $\Delta_{123} \approx 0$, while the contraction-consistent Nakatsuji-Yasuda (NY) reconstruction [45, 46] approximates the three-particle cumulant as two subsequent two-particle interactions. For both reconstructions we have used the contraction-consistency conditions [23] which improved the results. We have observed that already for weakly interacting systems a large fraction of excited states are strongly correlated. This limits the application of the TD-2RDM method. Nevertheless, the method gives good results for weakly excited states of weakly interacting systems. In this regime the contraction-consistent NY reconstruction is more accurate than the contraction-consistent Valdemoro reconstruction. In the weakly interacting regime the TD-2RDM method is capable of reproducing the low-energy excitation spectrum via linear response to high accuracy. Using the TD-2RDM method to describe potential quenches [67] we have reproduced the results for weak quenches with very high accuracy. Applying the TD-2RDM method to highly-excited initially uncorrelated states as done in literature [24–26] we have observed that the 2-RDM has to be purified because of stability problems encountered otherwise. Consistently, we have observed a significant rise of two and three-particle correlations. The Alcoba purification used for molecules in [23] does not grasp the dynamics of the system properly because it does not conserve the energy during the purification step. To overcome this we have proposed a very simple energy conserving (EC) purification that conserves the energy during the purification for weak interactions. Applying it to the Hubbard model we have observed that the TD-2RDM method yields good results that are comparable to the exact calculation and more accurate than previous results [24–26].

With the EC purification we observed to absence of instabilities for the TD-2RDM method for weak interactions which was the main problem in [24]. Yet for strong interactions the multiplication of the interaction strength U with a large error in the 3-RDM leads to numerical instabilities which we were not able to avoid.

As observed in [26] we have seen that the correlation strength of the system decreases if the number of sites, i.e. the number of particles, is increased for constant interaction strength. Hence, we expect the TD-2RDM method to be more accurate for larger particle numbers.

In contrast to methods currently used for the one-dimensional Hubbard model, like the time-dependent density matrix renormalization group method [15], the TD-2RDM method can be extended to higher dimensions. In future, we will extend the method to the two-dimensional Hubbard model and calculate the low energy excitation spectrum for small square Hubbard nano-cluster as done for the one-dimensional case. The numerical effort scales with r^5 where r is the number sites.

We asses that with the present implementation and usage of parallel computing 10×10 clusters can be investigated.
To improve the reconstruction of the 3-RDM we will use a ladder approximation in the spirit of the NY reconstruction to approximate the three-particle cumulant. Herein, we plan to include further topologically distinguishable interaction diagrams and also sophisticated approximations for the propagator connecting the two-particle cumulants. Further, we plan to develop a more sophisticated purification scheme which incorporates the semi-definiteness of the 2-RDM, the semi-definiteness of the two-hole reduced density matrix, and energy conservation. To do so, we work on a purification scheme which modifies the collision operator at each time-step such that the 2-RDM fulfills the before mention conditions instead of purifying the 2-RDM.

Acknowledgements

I would like to thank my advisor Iva Březinová for helping me through all troubles of this thesis and for countless discussions about things related to my thesis, about physics in general as well as the "real" world outside the physics bubble. I thank my advisor Joachim Burgdörfer for his constant interest in my work and for helping me to focus on the physics of all problems, rather than on math. I am very grateful to Fabian Lackner, who introduced me to the MCTDHF code of Takeshi Sato, to the physical and computational aspects of the TD-2RDM method, and that he gave me a first version of the Hubbard code. His constant interest in new results and discussions with him considerably improved this work. I thank all colleagues in the group of Theoretical Quantum Dynamics at the Institute of Theoretical Physics for scientific discussions and distraction during lunch and coffee breaks. I am grateful to my mother for supporting me throughout my studies, both mentally and financially. I thank my father that he has always been curious about what I was working on and that he has encouraged me to be interested into science.

Cuiusvis hominis est errare, nullius nisi insipientis in errore perseverare.
Cicero, Orationes Philippicae (Die Philippischen Reden) XII, II, 5

A. Norm and energy conservation for the TD-2RDM method

We review the conditions that have to be fulfilled for the equations of motion for the 2-RDM to conserve norm and energy following [23]. In order for the particle number to be conserved

$$\frac{\partial}{\partial t}\mathrm{Tr}_{12}\left(D_{12}\right)=0 \tag{A.1}$$

has to hold. Inserting Eq. 3.16 into Eq. A.1 we obtain

$$i\hbar\frac{\partial}{\partial t}\mathrm{Tr}_{12}\left(D_{12}\right)=\mathrm{Tr}_{12}\left(\left[\hat{H}_{12},D_{12}\right]\right)+\mathrm{Tr}_{123}\left(\left[V_{1,3}+V_{2,3},D^{R}_{123}\right]\right)=0, \tag{A.2}$$

where we have used the antisymmetry of the commutator and the linearity and invariance of the cyclic permutations. Thus, the equations of motion are norm conserving. Conservation of energy can be shown by taking the first derivate of Eq. 3.14 with respect to t

$$\begin{aligned}\frac{\partial}{\partial t}E\left(t\right)=&\frac{1}{2}\mathrm{Tr}_{12}\left[\left(\partial_t H_{12}\right)D_{12}+H_{12}\left(\partial_t D_{12}\right)\right]\\ =&\frac{1}{2i\hbar}\mathrm{Tr}_{12}\left(H_{12}\cdot\left(\left[H_{12},D_{12}\right]+\mathrm{Tr}_3\left[V_{1,3}+V_{2,3},D_{123}\right]\right)\right)\\ =&\frac{N-2}{2i\hbar\left(N-1\right)}\mathrm{Tr}_{12}\left(\left[V_{1,2},h_1+h_2\right]\left(D_{12}-\frac{1}{N-2}\mathrm{Tr}_3 D^{R}_{123}\right)\right),\end{aligned} \tag{A.3}$$

where we have used that the Hamiltonian H_{12} is time independent ($\partial_t H_{12}=0$). Eq. A.3 shows that the reconstructed 3-RDM has to contract correctly to the 2-RDM

$$D_{12}=\frac{1}{N-2}\mathrm{Tr}_3\left(D^{R}_{123}\right), \tag{A.4}$$

in order for the energy to be a conserved quantity. This provides a condition on the reconstruction of the 3-RDM. The Valdemoro and the NY reconstruction do not fulfill Eq. A.4 and are not energy conserving. However, the contraction consistent extension introduced in [23] fulfills this condition. Hence the contraction consistent Valdemoro and the contraction consistent NY reconstruction are energy conserving.

B. Exact diagonalization of the one-dimensional Hubbard model

To use exact diagonalization we choose the sites of the Hubbard model as basis. We treat the spin up and the spin down configuration separately. We illustrate the basis for a two-site Hubbard model:

$$\begin{pmatrix}1\\0\\0\\0\end{pmatrix} \hat{=} |1,0\rangle \otimes |1,0\rangle \tag{B.1}$$

$$\begin{pmatrix}0\\1\\0\\0\end{pmatrix} \hat{=} |1,0\rangle \otimes |0,1\rangle \tag{B.2}$$

$$\begin{pmatrix}0\\0\\1\\0\end{pmatrix} \hat{=} |0,1\rangle \otimes |1,0\rangle \tag{B.3}$$

$$\begin{pmatrix}0\\0\\0\\1\end{pmatrix} \hat{=} |0,1\rangle \otimes |0,1\rangle\,. \tag{B.4}$$

$|1,0\rangle \otimes |0,1\rangle$ denotes the state where one spin $\uparrow$ particle is located on the first site and one spin $\downarrow$ particle is located on the second site. In this basis the Hamiltonian is given by

$$H = \begin{pmatrix} U & -J & -J & 0 \\ -J & 0 & 0 & -J \\ -J & 0 & 0 & -J \\ 0 & -J & -J & U \end{pmatrix}. \tag{B.5}$$

For larger systems the calculation is not as straightforward. In general the linear dimension of the one-dimensional Hubbard Hamiltonian at half-filling is

$$\binom{N}{N/2}^2. \tag{B.6}$$

We write each configuration as

$$|\alpha_1, ..., \alpha_i, ..., \alpha_r\rangle \otimes |\beta_1, ..., \beta_i, ..., \beta_r\rangle \,, \tag{B.7}$$

where α_i (β_i) is the occupation number of the i^{th} site for spin $\uparrow$ ($\downarrow$). r is the number of sites. Treating a fermionic system α_i (β_i) can only be 0 or 1. The configuration of each basis vector is stored in a separate function where the occupation of each site i is stored separately for spin $\uparrow$ and $\downarrow$ To obtain the i^{th} line of H we calculate the action of H onto the i^{th} eigenvector

$$H \begin{pmatrix} 0 \\ . \\ . \\ . \\ 1_i \\ . \\ . \\ . \\ 0 \end{pmatrix} = h_i. \tag{B.8}$$

The interaction term can be implemented easily by setting all matrix elements to U where the site is doubly occupied.
The kinetic operator $\hat{T}$ is not as easily implemented because it is not diagonal and makes out of a given configuration two new different configurations, e.g.

$$\hat{T}\,|0, 0, 1, 0, 0\rangle = -J\,|0, 1, 0, 0, 0\rangle - J\,|0, 0, 0, 1, 0\rangle \,. \tag{B.9}$$

To know the elements that are related to each other we define a a unique reference number for the spin $\uparrow$ part, $r_\uparrow$, of each configuration and one for the spin $\downarrow$ part, $r_\downarrow$. We therefore convert the binary number given by the configuration, Eq. B.7, into a decimal number for spin $\uparrow$ and $\downarrow$ separately, e.g.

$$|0, 1, 0, 1, 0, 1\rangle \otimes |1, 1, 1, 0, 0, 0\rangle \tag{B.10}$$

$$\rightarrow r_\uparrow = 0 \cdot 2^5 + 1 \cdot 2^4 + 0 \cdot 2^3 + 1 \cdot 2^2 + 0 \cdot 2^1 + 1 \cdot 2^0 = 21, \tag{B.11}$$

$$\rightarrow r_\downarrow = 1 \cdot 2^5 + 1 \cdot 2^4 + 1 \cdot 2^3 + 0 \cdot 2^2 + 0 \cdot 2^1 + 0 \cdot 2^0 = 56. \tag{B.12}$$

We thus have a direct mapping between the index of the configuration i and $r_\uparrow$, $r_\downarrow$. Having the new configuration we can directly calculate the new $r_\uparrow$, $r_\downarrow$ and relate it to the corresponding configuration index k. Now the k^{th} element of h_i is set to $-J$. Since the kinetic operator separates in spin $\uparrow$ and $\downarrow$ we perform this for both spins independently.
Having obtained the complete Hamiltonian we can directly calculate the eigenenergies and eigenstates using the LAPACK routine *zheev* which uses the Pal-Walker-Kahan variant of the QL or QR algorithm.

Bibliography

[1] J. Quintanilla and C. Hooley. *The strong-correlations puzzle.* Physics World p. 32 (2009).

[2] R. G. Parr and W. Yang. *Density-Functional Theory of Atoms and Molecules.* Number 16 in International series of monographs on chemistry. Oxford University Press (1989).

[3] C. A. Ullrich. *Time-Dependent Density-Functional Theory.* Oxford Gratuate Texts. Oxford University Press (2012).

[4] J. Hubbard. *Electron Correlations in Narrow Energy Bands.* Proceedings of the Royal Society of London. Series A **276**, 238 (1963).

[5] F. H. Essler, H. Frahm, F. Göhmann, A. Klüper, and V. E. Korepin. *The One-Dimensional Hubbard Model.* Cambridge University Press (2005).

[6] Editorial. *The Hubbard model at half a century.* Nature Physics **9**, 523 (2013).

[7] I. Bloch, J. Dalibard, and W. Zwerger. *Many-body physics with ultracold gases.* Reviews of Modern Physics **80**, 885 (2008).

[8] K.-H. Bennemann and J. B. Ketterson (eds.). *Novel Superfluids Volume 2*, chapter Optical Lattice Emulators: Bose and Fermi Hubbard Models. Number 157 in International Series of Monographs in Physics. Oxford University Press (2014).

[9] M. Greiner, O. Mandel, T. Esslinger, T. W. Hänsch, and I. Bloch. *Quantum phase transition from a superfluid to a Mott insulator in a gas of ultracold atoms.* Nature **415**, 39 (2002).

[10] R. Jördens, N. Strohmaier, K. Günter, H. Moritz, and T. Esslinger. *A Mott insulator of fermionic atoms in an optical lattice.* Nature **455**, 204 (2008).

[11] S. Fölling, S. Trotzky, P. Cheinet, M. Feld, R. Saers, A. Widera, T. Müller, and I. Bloch. *Direct observation of second-order atom tunneling.* Nature **448**, 1029 (2007).

[12] T. Esslinger. *Fermi-Hubbard Physics with Atoms in an Optical Lattice.* Annual Review of Condensed Matter Physics **1**, 129 (2012).

[13] K. Levin, A. L. Fetter, and D. M. Stamper-Kurn (eds.). *Ultracold Bosonic and Fermionic Gases*, volume 5 of *Contemporary Concepts of Condensed Matter Physics*, chapter Ultracold Atoms and Molecules in Optical Lattices. Elsevier (2012).

[14] A. Georges, G. Kotliar, W. Krauth, and M. J. Rozenberg. *Dynamical mean-field theory of strongly correlated fermion systems and the limit of infinite dimensions.* Reviews of Modern Physics **68**, 6861 (1996).

[15] U. Schollwöck. *The density-matrix renormalization group.* Reviews of Modern Physics **77**, 259 (2005).

[16] M. Lewenstein, A. Sanpera, V. Ahufinger, B. Damski, A. Sen, and U. Sen. *Ultracold atomix gases in optical lattices: mimicking condensed matter physics and beyond.* Advances in Physics pp. 243 – 379 (2007).

[17] P.-O. Löwdin. *Quantum Theory of Many-Particle Systems. I. Physical Interpretationsby Means of Density Matrices, Natural Spin-Orbitals, and Convergence Problems in the Method of Configurational Interaction.* Physical Review **97**, 1474 (1955).

[18] P.-O. Löwdin. *Quantum Theory of Many-Particle Systems. II. Study of the Ordinary Hartree-Fock Approximation.* Physical Review **97**, 1490 (1955).

[19] P.-O. Löwdin. *Quantum Theory of Many-Particle Systems. III. Extension of the Hartree-Fock Scheme to Include Degenerate Systems and Correlation Effects.* Physical Review **97**, 1509 (1955).

[20] W. Kutzelnigg, G. Del Re, and G. Berthier. *Correlation Coefficients for Electron Wave Functions.* Physical Review **172**, 49 (1968).

[21] Z. Huang and S. Kais. *Entanglement as measure of electron-electron correlation in quantum chemistry calculations.* Chemical Physics Letters **413**, 1 (2005).

[22] K. Held and N. Mauser. *Physics behind the minimum of relative entropy measures for correlations.* The European Physical Journal B **86** (2013).

[23] F. Lackner, I. Brezinova, T. Sato, K. L. Ishikawa, and J. Burgdörfer. *Propagating two-particle reduced density matrices without wavefunctions.* Physical Review A **91**, 023412 (2015).

[24] A. Akbari, M. Hashemi, A. Rubio, R. Nieminen, and R. van Leeuwen. *Challenges in truncating the hierarchy of time-dependent reduced density matrix equations.* Physical Review B **85**, 235121 (2012).

[25] S. Hermanns, K. Balzer, and M. Bonitz. *Few-particle quantum dynamics-comparing nonequilibrium Green functions with the generalized Kadanoff-Baym ansatz to density operator theory.* Journal of Physics: Conference Series **427**, 012008 (2013).

[26] S. Hermanns, N. Schlünzen, and M. Bonitz. *Hubbard nanoclusters far from equilibrium.* Physical Review B **90**, 125111 (2014).

[27] C. Pethick and H. Smith. *Bose-Einstein Condensation in Dilute Gases.* Cambridge University Press, 2 edition (2008).

[28] R. Grimm, M. Weidemüller, and Y. B. Ovchinnikov. *Optical Dipole Traps for Neutral Atoms.* Advances in Atomic, Molecular & Optical Physics **42**, 95 (2000).

[29] S. Peil, J. V. Porto, B. L. Tolra, J. M. Obrecht, B. E. King, M. Subbotin, S. L. Rolston, and W. D. Phillips. *Patterned loading of a Bose-Einstein condensate into an optical lattice.* Physical Review A **67**, 051603 (2003).

[30] U. Schneider, L. Hackermüller, S. Will, T. Best, I. Bloch, T. A. Costi, R. W. Helmes, D. Rasch, and A. Rosch. *Metallic and Insulating Phases of Repulsively Interacting Fermions in a 3D Optical Lattice.* Science **322**, 1520 (2008).

[31] W. Kohn. *Analytical Properties of Bloch Waves and Wannier Functions.* Physical Review **115**, 809 (1959).

[32] N. W. Ashcroft and N. D. Mermin. *Solid State Physics.* Saunders College Publishing (1976).

[33] E. Reichl. *A modern course in statistical physics.* John Wiley & Sons, Inc., 2 edition (1998).

[34] F. Schwabl. *Quantenmechanik.* Springer (2007).

[35] D. Hochstuhl, C. Hinz, and M. Bonitz. *Time-dependent multiconfigurational methods for the numerical simulation of photoionization processes of many-electron atoms.* The European Physical Journal Special Topics **223**, 177 (2014).

[36] R. J. Glauber. *Photon correlations.* Physical Review Letters **10**, 84 (1963).

[37] U. M. Titulaer and R. J. Glauber. *Correlation Functions for Coherent Fields.* Physical Review **140**, 676 (1965).

[38] P. A. M. Dirac. *Note on Exchange Phenomena in the Thomas Atom.* Proceedings of the Cambridge Philosophical Society **26**, 376 (1930).

[39] M. Bonitz. *Quantum Kinetic Theory*. Teubner-Texte zur Physik (1998).

[40] D. A. Mazziotti (ed.). *Reduced-Density Matrix Mechanics: With applications to many-electron atoms and molecules*, volume 134 of *Advances in Chemical Physics*. John Wiley & Sons, Inc. (2007).

[41] K. Sakmann, A. I. Streltsov, O. E. Alon, and L. S. Cederbaum. *Reduced density matrices and coherence of trapped interacting bosons*. Physical Review A **78**, 023615 (2008).

[42] R. Kubo. *Generalized Cumulant Expansion Method*. Journal of the Physical Society of Japan **17**, 012008 (1962).

[43] W. Kutzelnigg and D. Mukherjee. *Cumulant expansion of the reduced density matrices*. The Journal of Chemical Physics **110**, 2800 (1999).

[44] D. A. Mazziotti. *Complete reconstruction of reduced density matrices*. Chemical Physics Letters **326**, 212 (2000).

[45] K. Yasuda and H. Nakatsuji. *Direct determination of the quantum-mechanical density matrix using the density equation*. Physical Review Letters **76**, 1039 (1996).

[46] H. Nakatsuji and K. Yasuda. *Direct determination of the quantum-mechanical density matrix using the density equation. II*. Physical Review A **56**, 2648 (1997).

[47] L. Kong and E. F. Valeev. *A novel interpretation of reduced density matrix and cumulant for electronic structure theories*. The Journal of Chemical Physics **134**, 214109 (2011).

[48] A. Coleman. *Structure of Fermion Density Matrices*. Reviews of Modern Physics **35**, 668 (1963).

[49] J. Cioslowski (ed.). *Many-Electron Densities and Reduced Density Matrices*. Mathematical and Computational Chemistry. Kluwer Academic/Plenum Publishers (2000).

[50] F. Colmenero, C. Pérez del Valle, and C. Valdemoro. *Approximating q-order reduced density matrices in terms of the lower-order ones. I. General realtions*. Physical Review A **47**, 971 (1993).

[51] C. Valdemoro, L. Tel, and E. Perez-Romero. *Three-Body Correlation Effects in Third-Order Reduced Density Matrices*, volume 1 of *Quantum Systems in Chemistry and Physics*, pp. 3–16. Kluwer Academic Publishers (2000).

[52] R. Tregold. *Density Matrix and the Many-Body Problem.* Physical Review **105**, 1421 (1957).

[53] D. A. Mazziotti. *Structure of Fermionic Density Matrices: Complete N-Representability Conditions.* Physical Review Letters **108**, 263002 (2012).

[54] D. A. Mazziotti. *Purification of correlated reduced density matrices.* Physical Review E **65**, 026704 (2002).

[55] D. Alcoba, F. Casquero, L. Tel, E. Perez-Romero, and C. Valdemoro. *Convergence Enhancement in the Iterative Solution of the Second-Order Contracted Schrödinger Equation.* International Journal of Quantum Chemistry p. 620 (2005).

[56] K. Byczuk, J. Kuneš, W. Hofstetter, and D. Vollhardt. *Quantification of Correlations in Quantum Many-Particle Systems.* Physical Review Letters **108**, 087004 (2012).

[57] R. Horodecki, P. Horodecki, M. Horodecki, and K. Horodecki. *Quantum entanglement.* Rev. Mod. Phys. **81**, 865 (2009).

[58] M. F. Parsons, F. Huber, A. Mazurenko, C. S. Chiu, W. Setiawan, K. Wooley-Brown, S. Blatt, and M. Greiner. *Site-Resolved Imaging of Fermionic* ^{6}Li *in an Optical Lattice.* Phys. Rev. Lett. **114**, 213002 (2015).

[59] C. N. Yang. *Concept of Off-Diagonal Long-Range Order and the Quantum Phases of Liquid He and of Superconductors.* Reviews of Modern Physics **34**, 694 (1962).

[60] V. Vedral, M. B. Plenio, M. A. Rippin, and P. L. Knight. *Quantifying Entanglement.* Physical Review Letters **78**, 2275 (1997).

[61] A. Coleman and V. Yukalov. *Reduced Density Matrices.* Number 72 in Lecture Notes in Chemistry. Springer (2000).

[62] T. Giamarchi. *Quantum Physics in One Dimension.* International Series of Monographs on Physics. Oxford University Press (2003).

[63] E. H. Lieb and F. Y. Wu. *Absence of Mott Transition in an Exact Solution of the Short-Range, One-Band Model in One Dimension.* Physical Review Letters **20**, 1445 (1968).

[64] K. Winkler, G. Thalhammer, F. Lang, R. Grimm, J. Denschlag, A. Daley, A. Kantian, H. Büchler, and P. Zoller. *Repulsively bound atom pairs in an optical lattice.* nature **441**, 853 (2066).

[65] R. Sensarma, D. Pekker, E. Altman, E. Demler, N. Strohmaier, D. Greif, R. Jördens, L. Tarruell, H. Moritz, and T. Esslinger. *Lifetime of double occupancies in the Fermi-Hubbard model*. Physical Review B **82**, 224302 (2010).

[66] N. Strohmaier, D. Greif, R. Jördens, L. Tarruell, H. Moritz, T. Esslinger, R. Sensarma, D. Pekker, E. Altman, and E. Demler. *Observation of Elastic Doublon Decay in the Fermi-Hubbard Model*. Physical Review Letters **104**, 080401 (2010).

[67] U. Schneider, L. Hackermüller, J. Ronzheimer, S. Will, S. Braun, T. Best, I. Bloch, E. Demler, S. Mandt, D. Rasch, and A. Rosch. *Fermionic transport and out-of-equilibrium dynamics in a homogeneous Hubbard model with ultracold atoms*. Nature Physics **8**, 213 (2012).